

# **Exploring nonlinear effects in spin-systems using NMR**

A thesis

submitted in partial fulfilment of the requirements of the degree of

**Doctor of Philosophy**

by

**V R Krithika**

Registration ID-20163496



Department of Physics

**INDIAN INSTITUTE OF SCIENCE EDUCATION AND RESEARCH**

PUNE-411008, India



# Certificate

---

Certified that the work incorporated in the thesis entitled “**Exploring nonlinear effects in spin-systems using NMR**” submitted by **V R Krithika** was carried out by the candidate, under my supervision. The work presented here or any part of it has not been included in any other thesis submitted previously for the award of any degree or diploma from any other university or institution.

Date: May 2, 2023

Prof. T.S. Mahesh  
(Supervisor)

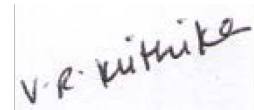


# Declaration

---

I declare that this written submission represents my ideas in my own words and where others ideas have been included, I have adequately cited and referenced the original sources. I also declare that I have adhered to all principles of academic honesty and integrity and have not misrepresented or fabricated or falsified any idea/data/fact/source in my submission. I understand that violation of the above will be cause for disciplinary action by the Institute and can also evoke penal action from the sources which have thus not been properly cited or from whom proper permission has not been taken when needed.

Date: May 2, 2023



V R Krithika  
(20163496)



*To my family*



# Acknowledgments

---

As my PhD draws to its close, I would like to thank many people who have made it possible. I wish to first thank my supervisor, Prof. T. S. Mahesh, for his support and guidance throughout this time. The depth of his understanding of NMR and quantum information processing, and overall passion for science and teaching have been a constant source of inspiration. He is always eager to discuss, learn and incorporate new ideas, and help students out when we are hopelessly stuck in some dead-end. As one of my seniors once remarked, if in five-ten years, we have even half the enthusiasm for science that Prof. Mahesh has, we would count ourselves fortunate.

I would next like to thank my research advisory committee members Prof. M. S. Santhanam and Dr. G. V. Pavan Kumar for their valuable feedback, discussions and guidance through the years. Working with collaborators Prof. M. S. Santhanam, Dr. Rejish Nath, Dr. Sai Vinjanampathy, Dr. Udaysinh Bhosale, Dr. V. S. Anjusha, Dr. Soham Pal, and Parvinder Solanki has been a very enriching experience. Dr. Uday introduced me to the field of quantum chaos and many concepts that fall within its purview, while Dr. Anjusha guided me through my first NMR experiments. Prof. Santhanam has been our go-to source for any queries regarding quantum chaos and quantum nonlinear dynamics. Dr. Rejish Nath's insight into Rydberg atom phenomena and their many applications in other platforms is inspiring. I learnt a great deal from Dr. Soham and his meticulous attention to detail, both in experiments and theory. I would like to thank Parvinder and Dr. Sai Vinjanampathy for building the theoretical formulation of our collaborative work on quantum synchronization, and for introducing me to the basics of open quantum systems. I would also like to thank Prof. Arul Lakshminarayan for his feedback and critical comments on the work pertaining to quantum chaos and dynamical tunneling in this thesis.

When I joined for PhD, I did not have any background in NMR or quantum information processing. I am thankful to my seniors in the lab Dr. V. S. Anjusha, Dr. Sudheer Kumar, Dr. Deepak Khurana and Dr. Soham Pal for helping me get started and always being available for help, be it doing experiments or understanding concepts. Anjusha and Deepak taught me how to handle the NMR spectrometer and guided me through my initial experiments. I would also like to thank my

other group members, former and present, Dr. Rupak Bhattacharya, Dr. Tanmay Chakraborty, Priya, Jiten, Arijit, Conan, Hari, Vishal, Harshanth, Deepesh, Anjali, Janani, Abhinav and Aashay for creating a very lively and intellectually stimulating environment. Evening tea breaks everyday with the group, where we would discuss anything under the sun, and Catan game nights were a lot of fun. I would like to express my sincere gratitude to technical staff Mr. Nitin Dalvi and Dr. Sandeep Mishra for ensuring that the spectrometers were always in their best condition and for help with any technical issues. I would like to thank Mr. Javed and Mr. Brij from Dr. Shabana Khan's lab, and Dr. Minhaj from Prof. Harinath Chakrapani's lab for extensive help with sample preparation and analysis. I would also like to thank department staff Mr. Prabhakar and Mrs. Dhanashree, and office staff Mr. Tushar and Mr. Ranjan Sahu, who many times went out of their way to help us students with administration tasks. I would like to thank Innoplexus Consulting Services Pvt Ltd and Scivic Engineering Pvt Ltd and I-HUB QTF for funding during extension period, and SERB DST for international travel support to attend a conference.

I am very lucky to have had a wonderful group of friends Dibyata, Anjusha, Hridya, Prachi, Ajith, Giri at IISER. From cooking and food sessions, making customized gifts, jamming sessions to quizzing, and 3 am badminton games outside hcross, they made life away from lab really incredible and enjoyable. Ajith with his meticulous attention to detail even in the smallest tasks, Anjusha with her confident and go-getter personality who manages to make time for many things despite being busy, Prachi in her fun loving and at the same time pragmatic approach to life, always reminding us that we should be investing money, Hridya with her quiet demeanour who puts in special efforts to avoid being noticed, and her voracious appetite for pani puri and books, Giri with his cheerful disposition, and finally Dibyata, the most creative and resourceful of the lot, and also the one who had to endure me the most. From making vlogs to skateboarding, her enthusiasm for trying new things is infectious, and even when suffering from some very serious health complications, she has never lost her sense of humour - or her dedication to work. A gifted athlete as well, to this day, she remains the only person to have scored a six in the women's IPL tournament. Be it normal working days or extremely adventurous group trips (which at times had us wondering if we would come back safe), this truly awesome bunch of people have made many good times great and bad times easier.

I would also like to thank my batchmate Bhagya for her delightful company, and whose undaunted

spirit is extraordinary. Thanks also to the Kill Bill cricket team for some very fun times and great memories. My thanks also to the members of Lab 210 at hcross for accommodating me on multiple occasions.

None of this would have been possible without my friends Nandita and Shree, who despite being the farthest away, have always remained the closest. They have been a constant through good times and bad, for a very long time now. Both of them have been, and continue to be an inspiration in so many ways. With the onset of the pandemic, my mental health took a nosedive. Return to any semblance of normalcy has been because of some friends, especially Dibyata, Shree, Nandita and Shyamalee, who have been kind and patient enough not to block my calls even if I was hounding them for the umpteenth time in a day. My thanks also to my senior and friend, Soham, in this regard.

I am forever grateful to my family for their encouragement and support throughout. They have been patiently impatient with every 'it will be over in a few months' I have been promising them over many past months. I am also grateful to my relatives in Pune for always welcoming me with open arms, and for many delicious meals.

Finally, I would like to express my heartfelt gratitude to countless writers, musicians, storytellers, sportspersons, adventurers and artists of the past and present, whose work and lives have provided refuge, encouragement and hope in some of the most trying times. Thank you, truly.



# Abstract

---

Nonlinear dynamics forms the core of classical complex systems. The varied degrees of interactions among multiple parameters characterizing a system give rise to a plethora of phenomena from cosmic dynamics, chemical kinetics, circadian rhythms, atmospheric dynamics to markets and social networks. In the domain of physics, nonlinear dynamics has been exhaustively investigated in classical systems. However, its extension to quantum mechanics is yet to be completely understood. Research into the bridge connecting nonlinear dynamical behaviour in classical and quantum regimes started decades ago, and it continues to remain significant today, especially with the development of quantum technology. Quantum computing and information processing protocols that harness innate quantum properties, such as superpositions and entanglement, have gone beyond theoretical constructs to become experimentally realizable reality that have also demonstrated extremely important and useful applications in security, metrology, communication, etc. Quantum technology currently is still very much in its infancy, and it is hence of timely interest to explore implications of nonlinearity in quantum systems and their possible applications. To this end, in this thesis, we have experimentally studied some facets of nonlinear effects in nuclear spin systems using Nuclear Magnetic Resonance (NMR) architecture. NMR is an extremely versatile test bed with precise control and manipulation of spins, and long coherence times that allows emulation of a wide range of desired Hamiltonians. We simulate dynamics under nonlinear Hamiltonian evolution via interactions between spins to study phenomena such as quantum chaos, quantum dynamical tunneling, interaction-induced Rydberg blockade and freezing, and quantum phase-synchronization. Aside from fundamental interest, these phenomena also have practical applications in quantum technology including but not limited to quantum control, developing efficient quantum computers with multiple interacting qubits, quantum networks, entangled state creation, selective control of qubits in a multi-qubit system, spectroscopy, etc.



# Synopsis

---

In this thesis, we report the study of nonlinear phenomena using nuclear spins in NMR architecture. The thesis is divided into six chapters, each of which are briefly reviewed below.

## **Chapter 1 – Introduction**

In this chapter, we set up the basics of quantum information processing by introducing necessary terms and concepts starting from qubits, quantum gates, density matrices to quantum correlations and measurements. We then give an overview of the NMR experimental test bed and how it can be used for quantum information processing tasks. We conclude this chapter with a discussion on nonlinear phenomena in classical and quantum domains, and some select topics which can be experimentally simulated using NMR spin registers.

## **Chapter 2 – Quantum chaos in a two-qubit kicked top**

Chaos is one of the signatures of classical nonlinear dynamics. However, its extension to the quantum regime still remains poorly understood. Owing to the uncertainty principle and linearity of quantum evolution under the Schrodinger equation, classical definitions of chaos built on sensitivity to initial conditions and exponential separation of trajectories become inoperative in the quantum domain. Quantum chaos has been shown to be characterized by inherent quantum properties such as entanglement and other quantum correlations. In this chapter, we experimentally simulate the kicked top model in a two-qubit NMR spin system to study quantum chaos. We demonstrate correspondences and deviations between the classical phase space and entanglement entropy patterns. Further, we also study Husimi distributions to emphasize the effect of chaos in the deep-quantum regime.

## **Chapter 3 – Quantum chaos in large spin registers**

In this chapter, we extend the study of quantum chaos to large spin registers with star-topology. These systems have been shown to have significant advantages for sensing, creating highly entan-

gled NOON states and for many other applications. Moreover, being much larger spin systems, they are closer to the classical limit. Here, we numerically study the kicked top model with disorder, i.e., the absence of all-to-all couplings, in star-topology systems of varying sizes, and use entanglement entropy to characterize quantum chaos. This study helps us get closer to understanding the bridge between quantum and classical regimes.

#### **Chapter 4 – Dynamical tunneling in nuclear spin systems**

Tunneling through a potential barrier is a quintessential feature of quantum mechanics, which has been widely investigated and applied. A less well-known aspect of quantum tunneling is the coupling between isolated symmetry related regular regions in a mixed phase space. Here, potential barriers are replaced by dynamical barriers, wherein a classical system initialized in one regular region cannot move to a symmetric regular region across the chaotic sea dividing them. A quantum system however can periodically tunnel between the regions. In this chapter, we experimentally study dynamical tunneling in two- and three-qubit spin systems using the kicked top model, using expectation values of angular momentum operators as probes. They show periodic revivals as the system moves from one regular region to another. In addition, we also study the importance of coherences in sustaining tunneling behaviour by introducing dephasing noise in the system.

#### **Chapter 5 – Quantum phase-synchronization in a nuclear spin system**

Synchronization, like chaos, is a hallmark of classical nonlinear systems. Quantum synchronization is currently gaining immense interest owing to its applications in many fields such as quantum thermodynamics, quantum networks, time crystals, etc. In this chapter, we experimentally demonstrate phase-synchronization of a four level nuclear spin system with a weak external drive. We develop the theoretical formulation using Husimi distribution to study phase-synchronization, and explain an efficient interferometric technique to bypass quantum state tomography to extract the characteristics of synchronization. We also study the robustness of synchronization against detuning and drive strengths via Arnold tongue behaviour.

#### **Chapter 6 – Simulation of interaction induced Rydberg phenomena in spin systems**

Rydberg blockade is an interaction induced phenomenon between two or more atoms which pro-

hibits the simultaneous excitation of all atoms, and has been shown to have important implications in quantum information processing protocols such as creation of entangled states. Rydberg-biased freezing is another phenomenon where selective weak driving of some atoms in an interacting many-atom system freezes their dynamics, allowing control of desired subsystems. In this work, we experimentally emulate Rydberg blockade and freezing in two- and three-qubit NMR spin registers. We also study the evolution of quantum discord between the qubits to gain deeper understanding of correlations as the systems evolve under blockade and freezing dynamics.



# List of Publications

---

1. **V. R. Krithika**, M. S. Santhanam, and T. S. Mahesh, *NMR investigations of Dynamical Tunneling in Spin Systems*, [arXiv:2212.12350](https://arxiv.org/abs/2212.12350) (2022) [Thesis Chapter 4].
2. **V. R. Krithika**, Parvinder Solanki, Sai Vinjanampathy, and T. S. Mahesh, *Observation of quantum phase-synchronization in a nuclear spin-system*, *Phys. Rev. A* **105**, 062206 (2022) [Thesis Chapter 5].
3. M. Harshanth Ram, **V. R. Krithika**, Priya Batra, and T. S. Mahesh, *Robust Quantum Control using Hybrid Pulse Engineering*, *Phys. Rev. A* **105**, 042437 (2022).
4. B. Sharmila, **V. R. Krithika**, Soham Pal, T. S. Mahesh, S. Lakshmibala, V. Balakrishnan, *Tomographic entanglement indicators from NMR experiments*, *J. Chem. Phys.* **156**, 154102 (2022).
5. T S Mahesh, Deepak Khurana, **Krithika V. R.**, Sreejith G J, C S Sudheer Kumar, *Star-topology Registers: NMR and Quantum Information Perspectives*, *J. Phys.: Condens. Matter* **33** 383002 (2021) [Thesis Chapter 3].
6. **V. R. Krithika**, Soham Pal, Rejish Nath, T. S. Mahesh, *Observation of interaction induced blockade and local spin freezing in a NMR quantum simulator*, *Phys. Rev. Research* **3**, 033035 (2021) [Thesis Chapter 6].
7. Priya Batra, **V. R. Krithika**, and T. S. Mahesh, *Push-Pull Optimization of Quantum Controls*, *Phys. Rev. Research* **2**, 013314 (2020).
8. Deepak Khurana, **V. R. Krithika**, and T. S. Mahesh, *Unambiguous measurement of information scrambling in a hierarchical star-topology system*, [arXiv:1906.02692](https://arxiv.org/abs/1906.02692).
9. **V. R. Krithika**, V S Anjusha, Udaysinh T. Bhosale, and T. S. Mahesh, *NMR studies of quantum chaos in a two-qubit kicked top*, *Phys. Rev. E* **99**, 032219 (2019) [Thesis Chapter 2].



# Contents

<b>Certificate</b>	<b>i</b>
<b>Declaration</b>	<b>iii</b>
<b>Acknowledgments</b>	<b>vii</b>
<b>Abstract</b>	<b>xi</b>
<b>Synopsis</b>	<b>xiii</b>
<b>List of Publications</b>	<b>xvii</b>
<b>1 Introduction</b>	<b>1</b>
1.1 Quantum information and computing . . . . .	2
1.1.1 Qubits . . . . .	2
1.1.1.1 Single-qubit system . . . . .	2
1.1.1.2 Multi-qubit system . . . . .	3
1.1.1.3 Pure and mixed states . . . . .	4
1.1.2 Density matrices . . . . .	5
1.1.2.1 Populations and coherences . . . . .	6
1.1.2.2 Reduced density matrices . . . . .	7
1.1.3 Measurement . . . . .	7
1.1.3.1 Projective measurements . . . . .	8
1.1.3.2 POVM . . . . .	9
1.1.4 Quantum gates . . . . .	9

1.1.4.1	Single qubit gates . . . . .	10
1.1.4.2	Multi-qubit gates . . . . .	11
1.1.5	Quantum correlations . . . . .	11
1.1.5.1	Entanglement . . . . .	12
1.1.5.2	Quantum discord . . . . .	13
1.2	NMR experimental test bed . . . . .	16
1.2.1	NMR qubits . . . . .	16
1.2.1.1	Chemical shift . . . . .	17
1.2.1.2	Interacting qubits . . . . .	17
1.2.1.3	Spin manipulation . . . . .	19
1.2.1.4	Thermal equilibrium . . . . .	20
1.2.1.5	Pulsed field gradient . . . . .	22
1.2.1.6	Relaxation . . . . .	22
1.3	NMR based quantum information processing . . . . .	22
1.3.1	Quantum gates in NMR . . . . .	23
1.3.2	Pseudo-pure states . . . . .	25
1.3.3	Measurement and readout . . . . .	27
1.4	Nonlinear dynamics using NMR . . . . .	28
<b>2</b>	<b>Quantum chaos in a two-qubit kicked top</b>	<b>30</b>
2.1	Introduction . . . . .	30
2.2	Objectives . . . . .	32
2.3	Quantum Kicked top . . . . .	32
2.3.1	Classical limit of QKT . . . . .	35
2.4	QKT with a pair of NMR qubits . . . . .	36
2.4.1	Experimental Setup . . . . .	37
2.4.2	Probing quantum chaos via von Neumann entropy . . . . .	39
2.5	Results and Discussion . . . . .	40
2.5.1	Husimi probability distribution . . . . .	43
2.6	Summary and outlook . . . . .	45

<b>3</b>	<b>Quantum chaos in large spin-registers</b>	<b>47</b>
3.1	Introduction . . . . .	47
3.1.1	Objectives . . . . .	48
3.1.2	Star topology registers . . . . .	48
3.2	Quantum chaos in star topology systems . . . . .	50
3.2.1	Results and discussion . . . . .	51
3.3	Conclusions and outlook . . . . .	53
<b>4</b>	<b>Dynamical tunneling in nuclear spins</b>	<b>54</b>
4.1	Introduction . . . . .	55
4.1.1	Objectives . . . . .	56
4.2	Dynamical tunneling in spin systems . . . . .	57
4.2.1	Quantum Kicked Top (QKT) model . . . . .	57
4.2.2	Dynamical tunneling in QKT model . . . . .	58
4.3	Experimental methodology . . . . .	60
4.3.1	NMR Hamiltonian . . . . .	60
4.4	Experimental Results . . . . .	64
4.4.1	$k = 0$ experiments . . . . .	64
4.4.2	Tunneling in mixed phase space ( $k = 3$ ) . . . . .	65
4.4.3	Robustness of dynamical tunneling . . . . .	71
4.5	Summary and outlook . . . . .	71
<b>5</b>	<b>Quantum phase-synchronization in a nuclear spin system</b>	<b>75</b>
5.1	Introduction . . . . .	75
5.2	Objectives . . . . .	77
5.3	Synchronization of a four-level system . . . . .	79
5.3.1	System with drive . . . . .	81
5.4	Experimental setup . . . . .	82
5.4.1	Spin system and the drive . . . . .	83
5.4.2	Steady state dynamics . . . . .	84
5.4.3	Optimum drive amplitude . . . . .	86

5.4.4	Interferometric measurement of Husimi distribution . . . . .	87
5.5	Results and discussion . . . . .	90
5.5.1	Low power RF calibration . . . . .	90
5.5.2	Synchronization experiments . . . . .	92
5.6	Summary and outlook . . . . .	95
<b>6</b>	<b>Simulation of interaction induced Rydberg phenomena in spin systems</b>	<b>96</b>
6.1	Introduction . . . . .	97
6.2	Objective . . . . .	98
6.3	Rydberg blockade and Rydberg biased freezing . . . . .	98
6.3.1	Rydberg blockade . . . . .	99
6.3.2	Rydberg biased freezing . . . . .	101
6.3.3	Mapping Rydberg atom Hamiltonian to spins . . . . .	101
6.4	Experimental setup and results . . . . .	102
6.4.1	Capturing single spin-1/2 dynamics in a multi-qubit system . . . . .	104
6.4.2	Initialization, Readout, and Modeling Experimental Imperfections . . . . .	106
6.5	Results and Discussion . . . . .	107
6.5.1	Non-interacting spins ( $\mathcal{J}_{ij} = 0$ ) . . . . .	107
6.5.2	Strongly interacting case: Interaction induced excitation blockade . . . . .	108
6.5.3	Strongly interacting case: Local spin freezing . . . . .	111
6.6	Summary and outlook . . . . .	114
	<b>Thesis Summary</b>	<b>115</b>
	<b>Appendix</b>	<b>117</b>
	<b>References</b>	<b>125</b>

# CHAPTER 1

---

## Introduction

---

The invention of transistors revolutionized technology and ushered in the digital era, with monumental developments in electronics ranging from computers, communication technology, to current day smartphones. However, even the most powerful supercomputers of today cannot simulate many of nature's most fundamental quantum mechanical phenomena owing to the enormous complexity of quantum systems [1]. The possible potential of inherently 'quantum' simulators was foreseen by Yuri Manin and Richard Feynman [1] in the 1980s, which quickly caught on in the 90s with multiple works demonstrating the advantages of quantum simulators - Bennett and Brassard's development of BB84 quantum cryptography protocol [2], the Deutsch-Jozsa algorithm to determine if an  $n$ -bit function is constant or balanced [3], Shor's algorithm for prime factorization of large numbers which have applications in cryptography [4], and Grover's search algorithm to identify a marked state in an unstructured database [5], to name a few. The first experimental realization of quantum computing was demonstrated in nuclear magnetic resonance (NMR) architecture independently by Cory, et. al., [6] and Gershenfeld, et. al., [7] in 1997. Today, the field has progressed tremendously with multiple architectures [8–10] apart from NMR such as superconducting qubits [11, 12], trapped ions [13, 14], ultracold atoms [15–17], quantum dots [18–20], and photonic systems [21–24] at the forefront. Even tech leaders such as IBM [25], Google [26], and many independent ventures [27–30] are investing heavily in quantum technologies. The second quantum revolution is well underway, and it holds much promise for far reaching developments across science starting from superconductivity and material research in physics, reaction mechanisms in chemistry, to photosynthesis, protein folding and drug discovery in biology and medicine.

In the following sections, we explain the fundamentals of quantum information processing and how they can be implemented in the NMR architecture.

## 1.1 Quantum information and computing

In this section, we briefly look into the building blocks of quantum information and computation.

### 1.1.1 Qubits

#### 1.1.1.1 Single-qubit system

The basic unit of classical information is a binary digit, or *bit*, which can only take one of two possible values - conventionally labelled 0 and 1. Classical computation proceeds by performing logical operations on such bits giving a string of bit values as the final output. Bits can physically be realized, for instance, by voltage off and on values respectively, while logical operations can be implemented by switching operations of a circuit. The quantum mechanical equivalent of bits, *qubits*, are two-level quantum systems. These can be realized in multiple ways - polarization states of a photon, spin states of an electron or nucleus, non-degenerate energy levels of neutral atoms, etc. However, unlike classical bits which can *only take one value at a time*, qubits can exist in both values simultaneously due to the fundamental principle of *quantum superposition*. The general state of a qubit in the two-dimensional Hilbert space can hence be described in terms of superposition of orthogonal basis states  $|0\rangle$  and  $|1\rangle$  as [31]

$$|\psi\rangle = \alpha|0\rangle + \beta|1\rangle, \quad (1.1)$$

where the complex coefficients  $\{\alpha, \beta\}$  satisfy the normalization condition  $|\alpha|^2 + |\beta|^2 = 1$ . The states  $|0\rangle$  and  $|1\rangle$  are usually represented in the matrix form  $|0\rangle = \begin{pmatrix} 1 \\ 0 \end{pmatrix}$  and  $|1\rangle = \begin{pmatrix} 0 \\ 1 \end{pmatrix}$ , commonly referred to as the computational basis states, rendering a general state in the form  $|\psi\rangle = \begin{pmatrix} \alpha \\ \beta \end{pmatrix}$ . From the definition in Eq. 1.1, we can see that the qubit is exactly in state  $|0\rangle$  for  $\alpha = 1$ , state  $|1\rangle$  for  $\beta = 1$ , and in a superposition for  $\alpha \neq 0 \neq \beta$  (subject to the normalization condition). Hence upon measuring this state, the probability of getting outcome  $|0\rangle$  is  $|\alpha|^2$ , and that of  $|1\rangle$  is  $|\beta|^2$ , which again is in contrast with classical measurements where outcomes are deterministic. A general single-qubit state can be visualized by equivalently expressing Eq. 1.1

in the form

$$|\psi\rangle = \cos(\theta/2)|0\rangle + e^{i\phi} \sin(\theta/2)|1\rangle, \quad (1.2)$$

which geometrically represents a point on a sphere of unit radius, called the Bloch sphere, and is shown in Fig. 1.1. Here,  $\theta \in [0, \pi]$  and  $\phi \in [0, 2\pi]$  can be identified as the polar and azimuthal angles respectively which span all points on the sphere and hence can describe any general state of a qubit. It is evident that the state in Eq. 1.2 is normalized with  $\alpha = \cos(\theta/2)$  and  $\beta = e^{i\phi} \sin(\theta/2)$ .

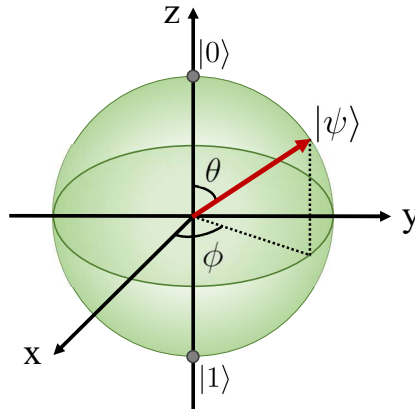


**Figure 1.1:** Bloch sphere representation of a qubit in a state  $|\psi\rangle$ .

### 1.1.1.2 Multi-qubit system

As we increase the number of qubits  $N$ , the corresponding Hilbert space dimension increases exponentially as  $2^N$ , where a multi-qubit system state can be constructed from a tensor product of single-qubit basis states. For instance the two-qubit composite state  $|00\rangle$  is obtained by  $|0\rangle \otimes |0\rangle$ . Thus, a general two-qubit pure state is described by

$$|\psi\rangle = a_1|00\rangle + a_2|01\rangle + a_3|10\rangle + a_4|11\rangle, \quad (1.3)$$

where  $\{|00\rangle, |01\rangle, |10\rangle, |11\rangle\}$  forms the basis set with coefficients satisfying the normalization condition  $|a_1|^2 + |a_2|^2 + |a_3|^2 + |a_4|^2 = 1$ . The definition of an arbitrary pure state can be

generalized to a multi-qubit system as

$$|\Psi\rangle = a_1|00\dots0\rangle + a_2|00\dots1\rangle + a_3|00\dots1\dots0\rangle + \dots + a_N|10\dots0\rangle + \dots + a_{2^N}|11\dots1\rangle, \quad (1.4)$$

where the states  $|\phi\rangle = \prod_N \otimes |i\rangle$  for  $i = 0, 1$  span the basis and coefficients fulfil the condition  $\sum_{i=1}^{2^N} |a_i|^2 = 1$ . Such pure states of multi-qubit systems exist on the hypersphere of their corresponding Hilbert space dimension and hence cannot be visualized easily.

Multi-qubit states come with inherent advantages over single-qubit systems in that they can carry quantum correlations such as entanglement, discord, etc. which have been shown to be extremely useful resources in various quantum information processing tasks [32, 33]. Furthermore, a distinguishing aspect of information processing using qubits is the potential of quantum superposition which can be harnessed to evolve the system under different basis states simultaneously, thereby providing a quantum parallelism. Quantum computation with d-level systems called qudits have also been studied [34, 35].

### 1.1.1.3 Pure and mixed states

Quantum states can be classified into two categories - pure and mixed. A system is said to be in a pure state if it can be described by a single state vector  $|\Psi\rangle = a_1|00\dots0\rangle + a_2|00\dots1\rangle + \dots + a_{2^N}|11\dots1\rangle$ . An ensemble is said to be in a pure state if each system is identically prepared in the same state  $|\Psi\rangle$ . For a single qubit, such a state lies on the surface of the Bloch sphere, as indicated by the red arrow in Fig. 1.1. On the other hand, if the ensemble is a statistical mixture of different pure states, then the state of the whole system cannot be described by a single state vector  $|\Psi\rangle$ . In such a mixture, the outcome of any measurement is dependent on the sub-ensemble being sampled, and is hence not identical over the entire ensemble. To describe such a system, we need to invoke the density operator formalism and is given by

$$\rho = \sum_i p_i |\phi_i\rangle\langle\phi_i|, \quad (1.5)$$

where  $\{|\phi_i\rangle\}$  are pure states, and the probabilities  $p_i$  add to 1. For example, a general mixture of a single-qubit system in the computational basis states can be given by  $\rho = p|0\rangle\langle 0| + (1-p)|1\rangle\langle 1| + \alpha|0\rangle\langle 1| + \alpha^*|1\rangle\langle 0|$ . Here, the probability of a measurement yielding outcome corresponding

to  $|0\rangle$  is  $p$  and that of  $|1\rangle$  is  $(1 - p)$ . It is important to note that the probabilistic distribution of measurements resulting from a mixed state is fundamentally different from that of a (pure) superposition state. For a single qubit, mixed states can lie at any radius from the centre to the surface of the Bloch sphere, based on the degree of mixedness in the system. The maximally mixed state of  $N$  qubits is given by the identity operator  $\mathbb{1}/2^N$ , which lies at the centre of the Bloch sphere (for single qubit)/higher-dimensional hypersphere (for multi-qubit systems).

### 1.1.2 Density matrices

The density matrix formalism is a widely used description to characterize and study the evolution of quantum systems. By definition, a density operator or matrix is given by

$$\rho = |\psi\rangle\langle\psi|, \quad (1.6)$$

for a pure state  $|\psi\rangle$ . However, most natural systems are not pure state ensembles, but rather occur as mixed states which are statistical mixtures of many pure states  $\{|\phi_i\rangle\}$ . The state of such ensembles can only be described using density matrices and are of the form

$$\rho = \sum_i p_i |\phi_i\rangle\langle\phi_i|, \quad \text{with} \quad \sum_i p_i = 1. \quad (1.7)$$

Properties of density matrices:

- (i)  $\text{tr}(\rho) = 1$  which ensures normalization and that all probabilities add to 1
- (ii)  $\rho$  is a positive operator with non-negative eigenvalues. This in-turn implies that the density matrix is Hermitian.

Although  $\text{tr}(\rho) = 1$  for both pure and mixed states,  $\text{tr}(\rho^2) = 1$  only for pure states, while  $\text{tr}(\rho^2) < 1$  for mixed states. The density matrix representation is basis dependent, and even in a given basis, it is not unique since any density matrix can be expressed as a convex sum of other density matrices. Hence, given a density matrix, it is not possible to uniquely determine the ensemble distribution. However, any general density matrix of a single-qubit system can be expressed as

$$\rho = \frac{\mathbb{1} + \sum_{i=x,y,z} r_i \sigma_i}{2}, \quad (1.8)$$

where  $\mathbb{1}$  is the two-dimensional identity matrix,  $r_i$  are components of the three-dimensional Bloch vector, and  $\sigma_i = \{\sigma_x, \sigma_y, \sigma_z\}$  are the Pauli spin operators. The magnitude of the Bloch vector  $|r| = 1$  for pure states and  $|r| < 1$  for mixed states.

### 1.1.2.1 Populations and coherences

The significance of density operator formalism can be appreciated by expanding Eq. 1.6 for a general pure state in an orthonormal basis. This gives matrix elements

$$\rho_{mn} = \langle m|\rho|n\rangle = \langle m|\psi\rangle\langle\psi|n\rangle = \sum_{i,j} a_i a_j^* \langle m|i\rangle\langle j|n\rangle, \quad (1.9)$$

and Eq. 1.7 for a mixed state

$$\rho_{mn} = \sum_k p_k \langle m|\psi_k\rangle\langle\psi_k|n\rangle = \sum_k p_k \sum_{i,j} a_i^k a_j^{k*} \langle m|i\rangle\langle j|n\rangle = \sum_{i,j} \overline{a_i a_j^*} \langle m|i\rangle\langle j|n\rangle, \quad (1.10)$$

where  $\overline{a_i a_j^*}$  denotes the ensemble average. From the above expressions, we can see that cases where  $i = j$  give a diagonal element  $\rho_{mm}$  with the corresponding probability  $|a_m|^2$ , which is interpreted as the *population* of state  $|m\rangle$ . All other cases with  $i \neq j$  represent off-diagonal elements  $\rho_{mn} = \overline{a_m a_n^*}$ , which are interpreted as *coherences*, indicating superposition between the states  $|m\rangle$  and  $|n\rangle$ .

The evolution of a density matrix under a time-independent Hamiltonian  $H$  for time  $t$  can be obtained by solving the von Neumann equation to get

$$\rho(t) = e^{-iHt} \rho(0) e^{iHt}. \quad (1.11)$$

Hence, at any time  $t$ , the populations and coherences can be extracted and studied as a function of the system evolution by performing quantum state tomography (explained in Sec. 1.3.3). The density matrix representation allows for easy handling of pure and mixed states of large ensembles, like those present in many experimental architectures such as NMR and Nitrogen-vacancy (NV) centres.

### 1.1.2.2 Reduced density matrices

Many quantum systems of interest comprise of two or more subsystems, say A,B,...N. Such systems are described in the composite Hilbert space  $H_A \otimes H_B \otimes \dots H_N$ , where  $H_i$  is a subsystem Hilbert space of dimension  $d_i$ . In such cases, it might sometimes be more interesting to study the properties of a subsystem than the whole. This is especially true in situations where quantum correlations (discussed in Sec. 1.1.5) are present in the system. A subsystem ( $\rho_A$ ) can be obtained from the parent composite system ( $\rho_{AB}$ ) by the *partial trace* operation, which is defined as

$$\rho_A = \text{tr}_B(\rho_{AB}) = \text{tr}_B \left( \sum_{i,j,k,l} c_{ijkl} |i_A\rangle\langle j_A| \otimes |k_B\rangle\langle l_B| \right), \quad (1.12)$$

where the composite density matrix ( $\rho_{AB}$ ) has been expressed in the eigenbases of subsystems A and B. Performing the trace over subsystem B, we get

$$\rho_A = \sum_{i,j,k,l} c_{ijkl} |i_A\rangle\langle j_A| \text{tr}(|k_B\rangle\langle l_B|) = \sum_{i,j,k,l} c_{ijkl} |i_A\rangle\langle j_A| \langle l_B|k_B\rangle = \sum_{i,j,k} c_{ijkk} |i_A\rangle\langle j_A|. \quad (1.13)$$

Similarly we can obtain reduced density matrix  $\rho_B = \text{tr}_A(\rho_{AB}) = \sum_{i,k,l} c_{iikl} |k_B\rangle\langle l_B|$ . The above definition of reduced density matrices can be verified to hold true since it correctly explains the outcomes of measurement observables on a subsystem of the composite system [31]. The reduced states of a pure state composite system can reveal information about quantum correlations - like entanglement present in the system. As discussed in Sec. 1.1.5, a separable pure state will give rise to a reduced state that is also pure, thereby satisfying the condition  $\text{tr}(\rho_A^2) = 1 = \text{tr}(\rho_B^2)$ . An entangled state on the other hand is not separable, and results in a mixed reduced state with  $\text{tr}(\rho_i^2) < 1$ .

### 1.1.3 Measurement

To extract information about observables such as position, spin, momentum, etc., from a quantum system, we need to perform measurements on it. However, the very act of measurement - for example, by shining photons - inherently disturbs the system and causes it to collapse (probabilistically) to an eigenstate of the observable. Also, such protocols require coupling the system with an appropriate measuring device, which causes the (system) dynamics to become non-unitary,

even though the evolution of the combined system and measuring device might be unitary. Measurement phenomena on quantum systems are described by a collection of operators  $\{M_m\}$  [31] which act on a state  $|\psi\rangle$  to give an outcome  $m$  described by the post-measurement state

$$|m\rangle = \frac{M_m|\psi\rangle}{\sqrt{p_m}}, \text{ with the probability } p_m = \langle\psi|M_m^\dagger M_m|\psi\rangle. \quad (1.14)$$

Since the sum of probabilities of all possible outcomes must add to one, i.e.,  $\sum_m p_m = 1$ , it automatically imposes the completeness condition on the measurement operators such that  $\sum_m M_m^\dagger M_m = \mathbb{1}$ .

### 1.1.3.1 Projective measurements

There exist special set of measurement observables called projective measurements, which are described by Hermitian operators  $M$ . The spectral decomposition of this Hermitian operator gives the eigenstates  $\{|m\rangle\}$  with eigenvalues  $\{\lambda_m\}$ , and the projective measurement operator is defined as the *projector* ( $P_m$ ) of these eigenstates [31]. Hence,

$$M = \sum_m \lambda_m |m\rangle\langle m| = \sum_m \lambda_m P_m. \quad (1.15)$$

Since the eigenbasis is orthonormal and complete, the projectors are orthogonal to one another, i.e.,  $P_m P_n = \delta_{mn} P_m$ , and  $\sum_m P_m = \mathbb{1}$ . The action of the projector corresponding to an outcome  $|m\rangle$  on a general state  $|\psi\rangle$  is given by

$$|\psi_m\rangle = \frac{P_m|\psi\rangle}{\sqrt{p_m}}, \text{ with probability } p_m = \langle\psi|P_m|\psi\rangle. \quad (1.16)$$

Projective measurements are useful since the average value of a measurement classically is [31]

$$\begin{aligned}
 \overline{M} &= \sum_m p_m \lambda_m \\
 &= \sum_m \lambda_m \langle \psi | P_m | \psi \rangle \\
 &= \langle \psi | \left( \sum_m \lambda_m P_m \right) | \psi \rangle \\
 &= \langle \psi | M | \psi \rangle = \langle M \rangle.
 \end{aligned} \tag{1.17}$$

The average value can equivalently be calculated for a mixed state as  $\overline{M} = \sum_i c_i \langle \psi_i | M | \psi_i \rangle = \text{Tr}(\rho M)$ . Hence, in any experimental ensemble, the average value of an observable gives the required measurement action. On a different note, projective measurements destroy the system state since they cause them to collapse to an eigenstate. Any further computation would require re-preparation of the state before measurement, and hence this may not be a preferred protocol across all experimental settings.

### 1.1.3.2 POVM

A more general measurement scheme makes use of Positive Operator-valued Measurement (POVM), in which the requirement that measurement operators be orthogonal to one another is relaxed [31]. They are described using measurement operators as  $E_m = M_m^\dagger M_m$ , which follow the criteria (a) operators  $E_m$  are positive, and (b) satisfy completeness condition via  $\sum_m E_m = \mathbb{1}$ . Hence, given a POVM operator  $E_m$ , the corresponding probability of outcome  $m$  for a system in state  $|\psi\rangle$  is  $p(m) = \langle \psi | E_m | \psi \rangle$ .

### 1.1.4 Quantum gates

Classical computing and information processing is accomplished by performing logical operations, or gates, on bits, which modify their state. Hence, with careful choice and sequence of such gates, any desired operations on an array of bits can be incorporated. Some of the most commonly used gates are the NOT, OR, AND, NOR, NAND, etc. The analogous operations on qubits are quantum gates, which bring about (unitary) rotations of qubits. With the help of such

single and multi-qubit rotations, the required Hamiltonian evolution can be implemented. Some basic single and multi-qubit gates are discussed below.

### 1.1.4.1 Single qubit gates

Single qubit gates are transformations of a qubit from a state  $|\psi\rangle = \alpha|0\rangle + \beta|1\rangle$  to  $|\psi'\rangle = \alpha'|0\rangle + \beta'|1\rangle$  (note that this definition can be readily extended to mixed states). Any such transformation can be imagined as a rotation of the qubit on the Bloch sphere about a direction  $\vec{n} = n_x\hat{x} + n_y\hat{y} + n_z\hat{z}$  by an angle  $\theta$ . A general rotation operator can be defined in terms of the Pauli spin matrix vector  $\vec{\sigma} = \sigma_x\hat{x} + \sigma_y\hat{y} + \sigma_z\hat{z}$  with  $\sigma_x = \begin{bmatrix} 0 & 1 \\ 1 & 0 \end{bmatrix}$ ,  $\sigma_y = \begin{bmatrix} 0 & -i \\ i & 0 \end{bmatrix}$ , and  $\sigma_z = \begin{bmatrix} 1 & 0 \\ 0 & -1 \end{bmatrix}$  as

$$R_{\vec{n}}(\theta) = \exp\left(\frac{-i\theta\vec{n} \cdot \vec{\sigma}}{2}\right) = \cos\left(\frac{\theta}{2}\right) \mathbb{1} - i \sin\left(\frac{\theta}{2}\right) (\vec{n} \cdot \vec{\sigma}). \quad (1.18)$$

We can see that the rotation operator for  $\theta = 180^\circ$  about the  $x$ -axis has the matrix representation (upto a phase factor) of  $R_x(\pi) = \begin{bmatrix} 0 & 1 \\ 1 & 0 \end{bmatrix}$ . Under the action of this operator, we get the transformation  $|0\rangle \rightarrow |1\rangle$  and vice-versa, which is the quantum analogue of a NOT gate. Similarly,  $\pi$  rotations about  $y$  and  $z$  axes generate different transformations.

An important gate for quantum operations is the Hadamard gate which generates superposition of states as  $|0\rangle \rightarrow \frac{|0\rangle+|1\rangle}{\sqrt{2}}$  and  $|1\rangle \rightarrow \frac{|0\rangle-|1\rangle}{\sqrt{2}}$ . The matrix representation of this gate is given by

$$H = \frac{1}{\sqrt{2}} \begin{bmatrix} 1 & 1 \\ 1 & -1 \end{bmatrix}. \quad (1.19)$$

Another single qubit gate is the phase gate. This operation selectively gives a phase to the state  $|1\rangle \rightarrow e^{i\phi}|1\rangle$  while leaving  $|0\rangle$  undisturbed. The matrix form of this gate is

$$R_\phi = \begin{bmatrix} 1 & 0 \\ 0 & e^{i\phi} \end{bmatrix}. \quad (1.20)$$

### 1.1.4.2 Multi-qubit gates

Multi-qubit gates are operations performed simultaneously on more than one qubit. One of the most important two-qubit gates is the *controlled-not gate*, or CNOT. This gate changes the state of the target qubit (T) conditional to the state of the control qubit (C). The operation proceeds the following way (i) if the control qubit is in state  $|0\rangle$ , then the target qubit is unperturbed (ii) if the control qubit is in state  $|1\rangle$ , then a NOT gate is applied on the target qubit. Hence under the action of this gate (in the computational basis), the states  $\{|0_C0_T\rangle, |0_C1_T\rangle\}$  remain unchanged, while  $|1_C0_T\rangle \rightarrow |1_C1_T\rangle$  and  $|1_C1_T\rangle \rightarrow |1_C0_T\rangle$ . The matrix form of this gate, where the first qubit is the control qubit and second qubit is the target, is given by

$$\text{CNOT} = \begin{bmatrix} 1 & 0 & 0 & 0 \\ 0 & 1 & 0 & 0 \\ 0 & 0 & 0 & 1 \\ 0 & 0 & 1 & 0 \end{bmatrix}. \quad (1.21)$$

In a multi-qubit system, CNOT gates can be applied on any pair with one as control and the other as target. Being a non-local gate, it is essential for generating entangled states. Single qubit gates and the two-qubit CNOT gate form a universal set, i.e., any Hamiltonian evolution can be expressed as a combination of gates in this set [31]. Other commonly used multi-qubit gates include SWAP gate and TOFFOLI gate [31].

### 1.1.5 Quantum correlations

Quantum correlations are a quintessential and defining feature of quantum mechanics. In naive terms, they are connections between subsystems which make it impossible to describe measurement results of each subsystem as independent, non-overlapping quantities [36]. Such quantum correlations, especially entanglement, have been shown to be vital resources in many quantum computing and information processing tasks [32, 33]. We briefly describe some types of quantum correlations and their quantifiers.

### 1.1.5.1 Entanglement

To understand entanglement, we first define a related concept of separability. A pure quantum state is said to be separable if, in the constituent orthonormal bases  $\{|\phi_i^A\rangle\}$  and  $\{|\chi_j^B\rangle\}$  of subsystems A and B respectively,  $|\psi_{AB}\rangle = \sum_i a_i |\phi_i^A\rangle \otimes \sum_j b_j |\chi_j^B\rangle$  [37]. In such a case, the reduced states are also pure, and are given simply by  $|\psi_A\rangle = \sum_i a_i |\phi_i^A\rangle$  and  $|\psi_B\rangle = \sum_j b_j |\chi_j^B\rangle$ . The definition of separability can be extended to mixed states as

$$\rho_{AB} = \sum_i c_i \rho_i^A \otimes \rho_i^B, \quad \text{with } \sum_i c_i = 1, \quad (1.22)$$

which is essentially a convex sum of tensor product states of constituent subsystems. If a bipartite quantum state cannot be expressed as a separable (or product) state, it is said to be entangled [37].

There are multiple quantifiers of entanglement in bipartite systems designed based on whether the composite state of the system is pure or mixed to start with. For a pure state  $\rho_{AB} = |\psi_{AB}\rangle\langle\psi_{AB}|$ , if the reduced states  $\rho_A, \rho_B$  are mixed, then the composite state is necessarily entangled. Hence, purity of reduced states acts as an quantifier for entanglement in pure composite states, and is also referred to as linear entropy. A related measure of entanglement in pure states is the entanglement entropy (which is used in this thesis and is explained in further detail below). For mixed states, measures of entanglement include concurrence, negativity and logarithmic negativity, and positive partial transpose (PPT) criterion [38].

### Entanglement entropy

This entanglement measure uses information content as a quantifier of entropy. Classically, entropy of a random variable  $X$  measures the information gain on learning its value, or the amount of uncertainty in  $X$  before learning this information [31]. It is quantified by the Shannon entropy given by  $H(X) = -\sum_i p_i \log p_i$ , where  $\{p_i\}$  is the probability distribution of the possible outcomes of  $X$ . The quantum mechanical extension of this definition for a system described by  $\rho$  is given by the von Neumann entropy

$$S(\rho) = -\text{tr}(\rho \log \rho) \equiv -\sum_i \lambda_i \log \lambda_i, \quad (1.23)$$

where  $\{\lambda_i\}$  are the eigenvalues of  $\rho$ . The von Neumann entropy of a pure state is always zero. It serves as a convenient measure of entanglement of a composite system  $AB$  when we study the entropy of its reduced subsystems. As mentioned previously, if the reduced state of a system  $\rho_A = \text{tr}_B[\rho_{AB}]$  after partial trace is pure, then the composite state is not entangled. For such a state,  $S(\rho_A) = 0 = S(\rho_B)$ . However, if the reduced state is mixed, then it implies that the parent composite state is entangled. Consequently,  $S(\rho_i) \neq 0$  for  $i = \{A, B\}$ . A state of dimension  $d$  in a maximally mixed state,  $\mathbb{1}/d$  has an entanglement entropy of  $S(\mathbb{1}/d) = \log_2(d)$ . Hence the entanglement entropy quantified using von Neumann entropy of the reduced system in a bipartite system  $AB$  is a useful quantifier of entanglement.

### 1.1.5.2 Quantum discord

Another non-classical correlation that is widely studied is quantum discord [39–43]. First proposed and quantified in Ref. [44], this correlation is defined in terms of the mutual information in a bipartite system. A quantum system can have both classical and quantum correlations [45]. The correlation measure of discord filters out all classical correlations present in the system, and faithfully quantifies only quantum correlations (if any), as described below.

Classical information content in a system, as explained in the previous section, is characterized by Shannon entropy,  $H(X)$ . Mutual information between two subsystems  $A$  and  $B$  is then defined as the common information shared between them. It can be visualized as the region of intersection indicated in green in Fig. 1.2(a). Mathematically, it can be quantified by

$$I(A : B) = H(A) + H(B) - H(A, B).$$

Alternatively, one can use conditional entropy  $H(A|B) = H(A, B) - H(B) = H(A) - I(A : B)$ , which quantifies the information content unique to  $A$  and not shared with  $B$ . Hence, mutual information can also be given by

$$J(A : B) = H(A) - H(A|B).$$

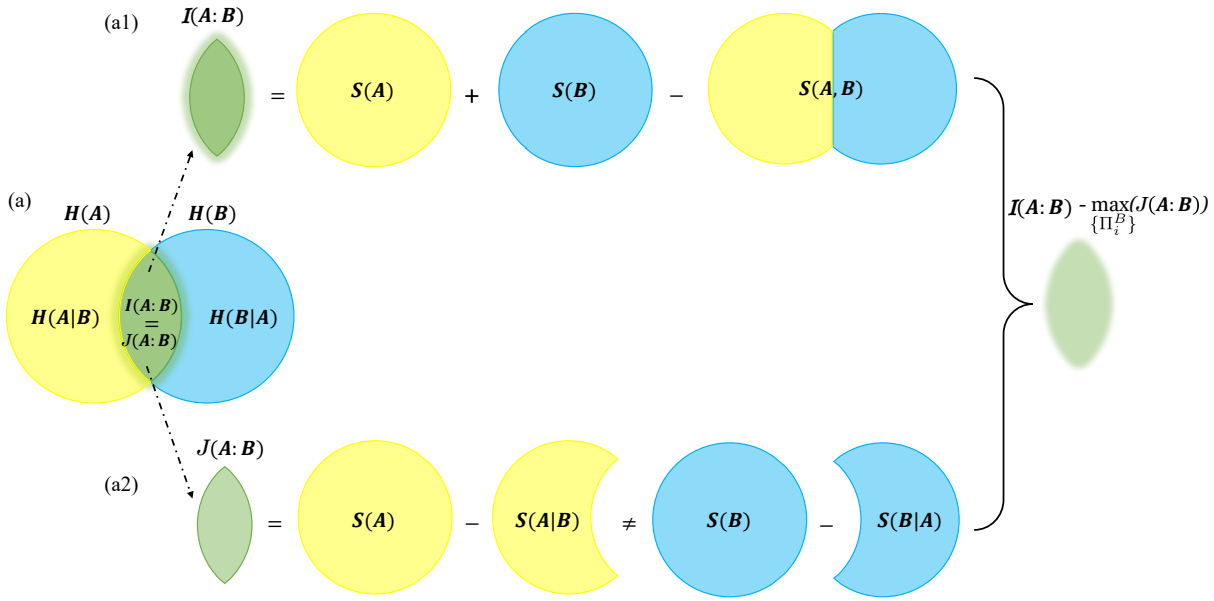


**Figure 1.2:** Mutual information calculated in two different ways for (a) classical scenario, where Shannon entropies of subsystems give  $I(A : B) = H(A) + H(B) - H(A, B)$ , and conditional measurements give  $J(A : B) = H(A) - H(A|B)$ . In this case,  $I(A : B) = J(A : B)$ . The quantum mechanical definition in terms of von Neumann entropy giving (a1)  $I(A : B) = S(A) + S(B) - S(A, B)$ , which contains both classical and quantum correlations (a2) conditional measurement resulting in  $J(A : B) = S(A) - S(A|B)$ , which when maximised over all measurement bases  $\prod_i^B$  of subsystem  $B$  give the total classical correlations in the system. The difference between the two quantum mechanical definitions gives quantum discord.

Note that this definition requires measurement of the subsystem  $B$  [46] since

$$H(A|B) = \sum_j p(b_j)H(A|B = b_j) , \text{ with}$$

$$H(A|B = b_j) = - \sum_i p(A = a_i|B = b_j) \log_2 p(A = a_i|B = b_j).$$

Definitions  $I(A : B)$  and  $J(A : B)$  are classically equivalent, and give identical values of mutual information, as shown in Fi.g 1.2(a). However, this is not the case for quantum systems.

In the quantum scenario, information content in a density matrix  $\rho$  is quantified by the von Neumann entropy  $S(\rho) = -\text{Tr}(\rho \log \rho)$ . For a bipartite quantum system  $AB$ , the mutual information between  $A$  and  $B$  can be defined analogous to  $I(A : B)$  as

$$\mathcal{I}(A : B) = S(A) + S(B) - S(AB), \tag{1.24}$$

where  $S(A)$ ,  $S(B)$  and  $S(AB)$  are von Neumann entropies of subsystems  $A$ ,  $B$ , and the composite system  $AB$  respectively. This definition is depicted in the top panel in Fig 1.2(a1). The alternative definition of mutual information is given by

$$J(A : B) = S(A) - S(A|B), \quad (1.25)$$

where the conditional entropy  $S(A|B) = \sum_j p_j^B S(A|B = b_j)$  is the entropy of subsystem  $A$  conditional to a measurement on subsystem  $B$  giving a result  $b_i$  from the possible outcomes of  $B$ , with probability  $p_j^B$  [44]. This is displayed in Fig. 1.2(a2).

Definitions Eq. 1.24 and Eq. 1.25 are *not* equivalent since the second definition ( $J(A : B)$ ) involves measurement. Measurement is a very intriguing process in quantum physics which is basis dependent and changes the state of the system [31, 46]. Hence, estimates of  $J(A : B)$  can vary depending on the choice of measurement bases, while  $\mathcal{I}(A : B)$  is independent of measurement basis. It is also important to note that  $J(A : B)$  is an estimate of *classical correlations* in the system since measurements trigger the collapse of  $B$ . Following this, the system is in a state  $\rho_{AB} = \sum_i p_i \rho_A \otimes |b_i\rangle\langle b_i|$  from which we can extract the classical correlations [45]. Hence, by maximising  $J(A : B)$  over all possible orthonormal measurement bases of  $B$ , one can determine the total classical correlations in the system. Consequently, the (minimum) difference between the two ways of evaluating mutual information in Eq. 1.24 and Eq. 1.25 gives the *quantum correlations* present in the system, and is called quantum discord. For orthonormal bases  $\{\Pi_i^B\}$  on subsystem  $B$ , discord is given by [44]

$$D(B|A) = \mathcal{I}(A : B) - \max_{\{\Pi_i^B\}} J(A : B), \quad (1.26)$$

Note that discord is not necessarily symmetric under system partitions since it involves measurements. It varies from 0 for states without quantum correlations to 1 for maximally entangled states.

## 1.2 NMR experimental test bed

In this thesis, we have used the NMR test bed to study nonlinear phenomena. Originating from the discovery of Rabi oscillations around the 1940s, NMR has undergone tremendous development both theoretically and experimentally [47]. It has pioneered vast areas of research in the fields of physics, chemistry, biology and medicine, in studies of magnetic properties of materials, structure of chemicals and proteins, tissue imaging via MRI, etc. [48–50]. NMR is also an excellent platform for implementation of quantum information processing tasks [51–53]. Here, we briefly overview the experimental setup and how it can be utilised to study phenomena pertaining to quantum information and computing.

### 1.2.1 NMR qubits

NMR makes use of the intrinsic spin degree of freedom of nuclei. Depending upon the configuration of nucleons in the system, it can have spin  $I = 1/2, 1, 3/2, \dots$ , each of which has an associated spin angular momentum  $\hat{\mathbf{I}}$  and the eigenvalues of the operator  $\hat{\mathbf{I}}^2$  are given by  $I(I+1)\hbar^2$  [49]. A non-zero spin has a magnetic moment given by  $\hat{\boldsymbol{\mu}} = \gamma\hbar\hat{\mathbf{I}}$  where  $\gamma$  is the gyromagnetic ratio. A spin- $I$  system when placed in an external magnetic field  $\hat{\mathbf{B}} = B_0\hat{z}$  interacts with it via Zeeman Hamiltonian which is given by

$$H_0 = -\hat{\boldsymbol{\mu}} \cdot \hat{\mathbf{B}} = -\gamma\hbar B_0 I_z = \hbar\omega_0 I_z, \quad (1.27)$$

where  $I_z = \sigma_z/2$  is the  $z$ -component of the spin angular momentum, and  $\omega_0 = -\gamma B_0$  is the Larmor frequency. Since a non-zero spin is like a tiny magnet, when placed in an external field, it experiences a torque, which causes its magnetic moment to precess about the field at  $\omega_0/2\pi$  frequency. For fields of a few Tesla (typical of commercial NMR spectrometers), the Larmor frequency is of the order of hundreds of MHz. For a spin- $I$  system, energy eigenvalues of the Hamiltonian are  $E = -m_s\hbar\gamma B_0$ , where  $m_s = \{-I, -I+1, \dots, I\}$  are the magnetic quantum numbers, which forms a  $2I+1$  level system with equal energy gaps  $\Delta E = \hbar\gamma B_0 = \hbar\omega_0$ . A spin-1/2 system consequently has two energy levels corresponding to  $m_s = \pm 1/2$ , which forms a qubit with  $|m_s = 1/2\rangle \equiv |0\rangle$  and  $|m_s = -1/2\rangle \equiv |1\rangle$ . Hence, we have established the initial

connection between NMR and quantum information processing.

### 1.2.1.1 Chemical shift

The above description is for a free spin- $I$  system. However, most of the nuclear spin systems used in experiments are not free elements, but molecules dissolved in some solvent. In this case, the local field experienced by a nucleus is different from a free spin due to the chemical environment around the nucleus in the molecule. The electronic cloud distribution from the surrounding elements alter the effective field around the nucleus, giving a modified Zeeman Hamiltonian [48, 49]

$$H = H_0 + \hbar\gamma\boldsymbol{\delta}_j \cdot \hat{\mathbf{B}}, \quad (1.28)$$

where  $\boldsymbol{\delta}_j$  is the *chemical shift tensor* at the site of the  $j$ -th spin. At a strong external field  $\hat{\mathbf{B}} = B_0\hat{z}$ , due to rapid tumbling motion of the molecules in liquid samples, this tensor reduces to an averaged isotropic scalar value  $\bar{\delta}$ . Hence, the above equation becomes  $H = -\hbar\gamma(1 - \bar{\delta})B_0I_z$ , where we can identify the shifted Larmor frequency  $\omega = -\gamma(1 - \bar{\delta})B_0$ . The chemical shift is characteristic of the molecule and helps with addressability of qubits.

### 1.2.1.2 Interacting qubits

Many quantum information processing tasks require at least two interacting qubits. In NMR, interactions naturally present in the system help in this regard. These interactions are of two types [49] -

- (i) electron mediated indirect spin-spin  $\mathcal{J}$ -coupling
- (ii) direct spin-spin coupling through space mediated by dipolar interactions

which are explained below. Spins with  $I \geq 1$ , called quadrupolar spins, have asymmetric electric charge distribution in the nuclei which gives rise to quadrupolar couplings [49]. In this thesis, we only consider spin-1/2 systems, and hence quadrupolar spins and their properties are not discussed here.

#### $\mathcal{J}$ -coupling

The indirect spin-spin coupling is an electron mediated effect via bonds between spins, and is

hence an intramolecular effect. In isotropic liquids, the rapid tumbling motion of the molecules does not average out the  $\mathcal{J}$ -coupling. This interaction is given by the Hamiltonian [48, 49]

$$H_J = \sum_i \omega_i I_{zi} + \sum_{i,j>i} 2\pi \mathcal{J}_{ij} \hat{\mathbf{I}}_i \cdot \hat{\mathbf{I}}_j. \quad (1.29)$$

where  $\hbar = 1$ ,  $\mathcal{J}_{ij}$  is the coupling between  $i$ -th and  $j$ -th spins whose spin operators are given by  $\hat{\mathbf{I}}_i = \{I_{\alpha i}\}$  with  $I_{\alpha i} = \sigma_{\alpha i}/2$  for  $\alpha = \{x, y, z\}$ . Depending on the relative strength of the coupling term with respect to the Zeeman term, the Hamiltonian can be further simplified. In the weak coupling limit at high fields, i.e.,  $|\mathcal{J}_{ij}| \ll |\omega_i - \omega_j|$ , under secular approximation [49], Eq. 1.29 becomes

$$H_J = \sum_i \omega_i I_{zi} + \sum_{i,j>i} 2\pi \mathcal{J}_{ij} I_{zi} I_{zj}. \quad (1.30)$$

This condition is always satisfied for *heteronuclear* systems in which the interacting qubits are of different species (for example  $^1\text{H}$  and  $^{13}\text{C}$ ), whose Larmor frequencies are separated in the range of hundreds of MHz, while their typical  $\mathcal{J}$  coupling values are of the order of few Hz. In the case of *homonuclear* systems, the interacting qubits are of the same species and hence this simplification does not hold. Since this interaction is a through bond effect, the strength of  $\mathcal{J}$ -coupling generally reduces with increasing intramolecular distance between spins.

### Dipolar coupling

Each nuclear spin has a dipole moment by which different spins can directly interact with one another through space. The dipolar coupling Hamiltonian ( $\hbar = 1$ ) can be given by [49]

$$H_D = a_{ij} \left( 3(\hat{\mathbf{I}}_i \cdot \mathbf{e}_{ij})(\hat{\mathbf{I}}_j \cdot \mathbf{e}_{ij}) - \hat{\mathbf{I}}_i \cdot \hat{\mathbf{I}}_j \right), \quad \text{with } a_{ij} = \frac{-\mu_0 \gamma_i \gamma_j}{4\pi r_{ij}^3}, \quad (1.31)$$

where  $\mu_0 = 4\pi \times 10^{-7}$  H/m is the magnetic constant,  $\gamma_i$  is the gyromagnetic ratio of the  $i$ -th spin,  $r_{ij}$  is the spin-spin distance, and  $\mathbf{e}_{ij}$  is a unit vector along the line joining the centres of spins  $i$  and  $j$ . Dipolar coupling interaction can be both intramolecular and intermolecular, and is strongly dependent on the state of the sample. In liquid samples, due to rapid tumbling motion, the dipolar coupling effectively averages to zero. However, it survives in anisotropic liquid crystal samples and solid state samples, which have high degree of order in them [49]. In this thesis, we have

only worked with liquid samples, and hence  $H_D = 0$ .

### 1.2.1.3 Spin manipulation

As explained in Sec. 1.2.1, the energy gaps between spin levels is in the range of hundreds of MHz, which fall under the radio frequency (RF) range. Hence, RF fields can be used to manipulate spins. A linearly polarized RF field applied transverse to the external field can be described by the following time-dependent Hamiltonian [48, 49]

$$H_{\text{RF}}(t) = -\gamma B_{rf}(t)I_x = -\gamma B_1 \cos(\omega_{rf}t + \phi)I_x, \quad (1.32)$$

where  $B_1$  is the RF amplitude,  $\omega_{rf}$  is its angular frequency, and  $\phi$  is its phase. The linearly polarized field can be decomposed into two counter-propagating circularly polarized fields described by

$$\begin{aligned} B_R(t) &= \frac{1}{2}B_1 [\cos(\omega_{rf}t + \phi)\hat{x} + \sin(\omega_{rf}t + \phi)\hat{y}], \\ B_{NR}(t) &= \frac{1}{2}B_1 [\cos(\omega_{rf}t + \phi)\hat{x} - \sin(\omega_{rf}t + \phi)\hat{y}]. \end{aligned}$$

Here, only the component rotating in the *same* direction ( $B_R(t)$ ) as the Larmor precession can effectively couple to it. The *counter-rotating* component ( $B_{NR}(t)$ ) will be precessing with twice the frequency with respect to the Larmor precession, and hence is non-resonant with the spin precession, and is generally ignored. Thus, the effective RF Hamiltonian is just the contribution of the co-rotating component

$$H_{\text{RF}}(t) = -\gamma \frac{B_1}{2} [\cos(\omega_{rf}t + \phi)I_x + \sin(\omega_{rf}t + \phi)I_y].$$

The time dependence in the Hamiltonian can be removed by going to a rotating frame of  $\omega_{rf}$ , which simplifies the above Hamiltonian to

$$H_{\text{eff}} = \Omega I_z + \omega_1 [\cos(\phi)I_x + \sin(\phi)I_y], \quad (1.33)$$

where  $\Omega = \omega_0 - \omega_{rf}$  is the difference between Larmor frequency of the spin and RF (same as rotating frame) frequency and is referred to as *offset*,  $\omega_1 = -\gamma B_1/2$  is called the nutation frequency, which serves as a measure of RF amplitude [49]. Note that the offset term is independent of the RF amplitude. When the RF frequency is exactly equal to the Larmor frequency ( $\omega_{rf} = \omega_0$ ), it is said to be *on-resonant*. This is equivalent to the spin not seeing any field along the  $\hat{z}$  direction in the rotating frame. A non-zero offset value on the other hand retains a residual field in the  $\hat{z}$  direction, and the spins see an effective field oriented between the transverse plane and  $\hat{z}$ .

Effect of RF pulse: application of an RF pulse in the on-resonant scenario induces rotation of the spin about the field direction and the corresponding flip angle is given  $\beta_p = \omega_1 \tau_p$ , where  $\tau_p$  is the pulse duration and  $\omega_1$  is the nutation frequency. Hence, by changing the RF amplitude and duration, one can implement different flip angles and realize the required spin evolution.

#### 1.2.1.4 Thermal equilibrium

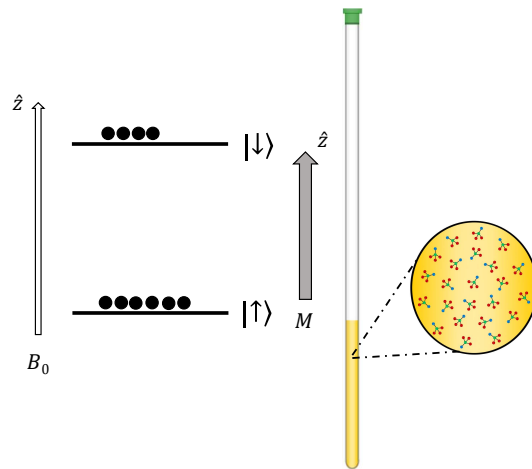


**Figure 1.3:** Schematic of a NMR sample in an external magnetic field. A typical sample contains about  $10^{18}$  molecules, which at thermal equilibrium settle to Boltzmann distribution at a temperature  $T$ . The fractional excess population in the ground state gives rise to a net magnetization  $M$  parallel to the external field.

A typical NMR sample contains about  $10^{18}$  molecules of the solute dissolved in an appropriate solvent. It then becomes impractical to consider the individual spins of each molecule, but rather work with bulk properties of the system. Consider an ensemble of spin-1/2 systems. In the absence of an external field, the spin levels  $|m_s = -1/2\rangle$  and  $|m_s = 1/2\rangle$  are degenerate, and each spin is oriented randomly. Hence, the net magnetic moment is zero. When an external field

$\hat{\mathbf{B}} = B_0 \hat{z}$  is introduced, the degeneracy between different spin levels is lifted, and they try to align along the  $z$ -direction. At ambient temperatures, the thermal energy of the system is much larger than the Zeeman energy splitting. Hence even the higher energy level is populated, and the system at thermal equilibrium at a temperature  $T$  is in a highly mixed state. The corresponding density matrix is diagonal with populations in different energy levels distributed according to the Boltzmann function [49]. The diagonal elements of the density matrix are given by

$$\rho_{\text{eq}}^i = \frac{e^{-E_i/k_B T}}{\sum_i e^{-E_i/k_B T}}, \quad (1.34)$$

where  $E_i$  is the energy of the  $i$ -th spin level and  $k_B$  is the Boltzmann constant. At thermal equilibrium, the ground state ( $|m_s = 1/2\rangle$ ) has slightly higher population than the higher energy level ( $|m_s = -1/2\rangle$ ), and hence there is a net magnetic moment or magnetization parallel to the external applied field, as shown in Fig. 1.3. This is a macroscopic quantity on which cumulative effects from the collection of spins is reflected.

At room temperatures and higher, thermal energy  $k_B T \gg \hbar\omega_0$  the Zeeman energy, and hence the density matrix elements can be approximated as

$$e^{-m_s \hbar\omega_0/k_B T} = 1 - \frac{m_s \hbar\omega_0}{k_B T} + \frac{1}{2!} \left( \frac{m_s \hbar\omega_0}{k_B T} \right)^2 + \dots \approx 1 - \frac{m_s \hbar\omega_0}{k_B T} = 1 + \frac{m_s \hbar\gamma B_0}{k_B T}.$$

For a spin-1/2 ensemble,  $m_s = \pm 1/2$ . Hence the partition function can be approximated as  $\sum_i e^{-E_i/k_B T} = e^{-\hbar\omega_0/2k_B T} + e^{\hbar\omega_0/2k_B T} \approx 2$ . The thermal equilibrium density operator is then given by

$$\rho_{\text{eq}} = \begin{bmatrix} \frac{e^{\hbar\gamma B_0/2k_B T}}{\sum_i e^{-E_i/k_B T}} & 0 \\ 0 & \frac{e^{-\hbar\gamma B_0/2k_B T}}{\sum_i e^{-E_i/k_B T}} \end{bmatrix} \approx \begin{bmatrix} \frac{1}{2} + \frac{\hbar\gamma B_0}{4k_B T} & 0 \\ 0 & \frac{1}{2} - \frac{\hbar\gamma B_0}{4k_B T} \end{bmatrix} = \frac{\mathbb{1}}{2} + \epsilon \frac{\sigma_z}{2}, \quad (1.35)$$

where  $\epsilon = \hbar\gamma B_0/2k_B T \approx 10^{-5}$  is called the *purity factor*, and  $\sigma_z$  is the Pauli- $z$  matrix. As the number of qubits  $N$  increases, the purity decreases exponentially as  $\epsilon = \hbar\gamma B_0/2^N k_B T$ . The uniform background population given by  $\mathbb{1}/2$  does not give rise to any observable signal. All interesting dynamics arises from the *traceless deviation density matrix* given in Eq. 1.35 by  $\rho_{\text{dev}} = \sigma_z/2 = I_z$ .

### 1.2.1.5 Pulsed field gradient

Pulsed field gradients (PFG) are *spatially* varying magnetic fields which are used to introduce space-dependent phases in the sample, based on requirement. They are widely used in imaging techniques, MRI, etc [49]. From an information processing point of view, PFGs are routinely used to destroy coherences, and for coherence order selection and filtering [54–56]. For instance, a gradient applied along the external field direction introduces spatially varying phase along  $z$  in the sample, and hence the net transverse magnetization components average to zero. Further details of PFG are provided in the Appendix A.1.

### 1.2.1.6 Relaxation

No system is truly isolated. All systems interact with an environment, which causes relaxation in the system. In NMR, relaxation occurs due to fluctuations in the magnetic field around spins brought about by thermal motion [49]. These cause transitions and loss of coherence in the system. One of the dominant causes of relaxation in liquid state NMR is the influence of dipole moments of surrounding spins as the molecules tumble, which give rise to fluctuations in the local fields around spins. The inherent relaxation processes can be classified into two categories - (i) Longitudinal relaxation ( $T_1$ ) - also known as spin-lattice relaxation, this mechanism induces transitions in the system and exchange of energy with surrounding nuclei and spins, which restores the equilibrium Boltzmann population distribution with no coherences.  $T_1$  timescale is typically ranges from few ms to s.

(ii) Transverse relaxation ( $T_2$ ) - also known as spin-spin relaxation, this phenomenon is the loss of coherence between spins. It results from fluctuations in the average field around nuclei due to inhomogeneities, which accumulate over time causing spins to start precessing out of phase with respect to one another and hence lose coherence. Time scales of  $T_2$  are typically such that  $T_2 < T_1$ .

## 1.3 NMR based quantum information processing

Here, we describe how properties of NMR systems can be used to study quantum information processing tasks.

### 1.3.1 Quantum gates in NMR

Any quantum computing task can be broken down into single qubit and multi-qubit operations.

In this thesis, these are accomplished in NMR by the following -

(i) Single qubit manipulation  $\leftrightarrow$  RF pulses

(ii) Multi-qubit operations  $\leftrightarrow$   $\mathcal{J}$  coupling

as explained below.

#### Single qubit operations

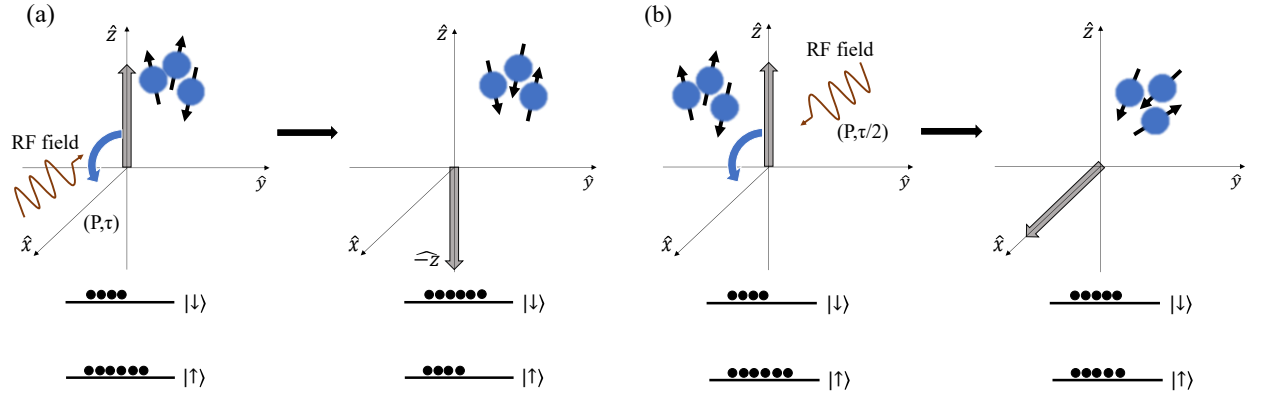


**Figure 1.4:** Effect of (a)  $\pi$  pulse with amplitude  $P$  applied for duration  $\tau$  about the  $x$ -axis which rotates the net magnetization by  $180^\circ$  from  $z$  to  $-z$ . This results in a population inversion, and is the experimental implementation of a NOT gate (b)  $\pi/2$  pulse of amplitude  $P$  applied for duration  $\tau/2$  about the  $y$ -axis rotates the net magnetization by  $90^\circ$  from  $z$  to  $x$ , which equalizes population in the energy levels. This is the implementation of a *pseudo* Hadamard gate.

The effect of RF pulses, as explained in Sec. 1.2.1.3, is to bring about rotations of a qubit. This can be used to apply various gates such as NOT, Hadamard, etc. Consider a single qubit system in thermal equilibrium described by the deviation density matrix  $\rho = \sigma_z/2$ . The net magnetization is parallel to the external field. An RF pulse of amplitude corresponding to  $\omega_1 = -\gamma B_1$  for duration  $\tau$  such that the flip angle  $\beta = \omega_1 \tau = \pi$  and phase  $\phi = 0$  which translates to the  $x$ -axis is given by the operator  $R_x(\pi) = \exp(-i\pi I_x)$  where  $I_x = \sigma_x/2$ . This pulse acts on each spin to induce a rotation by angle  $\pi$  about the  $x$ -axis such that the net magnetization is rotated by  $180^\circ$  from  $+z$  to  $-z$  as shown in Fig. 1.4(a). In quantum computation terms, this transforms the state

$|0\rangle \xrightarrow{R_x(\pi)} |1\rangle$ . The matrix form of the operator is

$$R_x(\pi) = \exp(-i\pi I_x) = -i \begin{bmatrix} 0 & 1 \\ 1 & 0 \end{bmatrix}.$$

The pre-factor  $i$  is a global phase and hence can be ignored.

The Hadamard gate  $H = \frac{1}{\sqrt{2}} \begin{bmatrix} 1 & 1 \\ 1 & -1 \end{bmatrix}$  can be experimentally realized by a sequence of two pulses (i)  $\pi/2$  rotation about  $y$ -axis ( $R_y(\pi/2)$ ), followed by (ii)  $\pi$  rotation about  $x$ -axis ( $R_x(\pi)$ ) whose matrix form is

$$R_x(\pi)R_y(\pi/2) = \exp(-i\pi I_x) \exp(-i\pi/2 I_y) = -i \begin{bmatrix} 0 & 1 \\ 1 & 0 \end{bmatrix} \frac{1}{\sqrt{2}} \begin{bmatrix} 1 & -1 \\ 1 & 1 \end{bmatrix} = \frac{-i}{\sqrt{2}} \begin{bmatrix} 1 & 1 \\ 1 & -1 \end{bmatrix}.$$

Again, the global phase  $-i$  can be ignored. In the above equation, the operators are time ordered from right to left. An experimentally easy way to achieve the Hadamard gate is a *pseudo-Hadamard*, which is just a  $R_y(\pi/2)$  pulse that rotates  $|0\rangle \xrightarrow{R_y(\pi/2)} \frac{|0\rangle+|1\rangle}{\sqrt{2}}$  and  $|1\rangle \xrightarrow{R_y(\pi/2)} \frac{|0\rangle-|1\rangle}{\sqrt{2}}$ . This is illustrated in Fig. 1.4(b). Likewise, any other single qubit gates can be realized by designing a sequence of pulses with appropriate angles and phases to get the desired effect.

### Multi-qubit operations

These operations rely on interactions between qubits. In liquid state NMR, the interaction is provided by  $\mathcal{J}$  coupling and the corresponding Hamiltonian of the system is given by  $H = \sum_{i,j>i} 2\pi \mathcal{J}_{ij} I_{zi} I_{zj}$ . When a qubit is evolved under this Hamiltonian for time  $\tau$ , the corresponding unitary operator is given by

$$U_J = \exp(-iH\tau) = \exp\left(-i \sum_{i,j>i} \pi \mathcal{J}_{ij} \tau 2I_{zi} I_{zj}\right). \quad (1.36)$$

The action of any operator  $\hat{A} = \eta \hat{O}$  on a density matrix  $\rho$  can be computed using the product operator formalism [49, 57]

$$\rho \xrightarrow[\tau]{\eta \hat{O}} \cos(\eta\tau)\rho + \sin(\eta\tau)[\hat{O}, \rho],$$

and the effective rotation achieved is  $\theta = \eta\tau$ . In Eq. 1.36,  $\theta = \pi\mathcal{J}\tau$ . Consider for instance the a two qubit system in a state  $\rho = I_{x1}$  evolving under  $\mathcal{J}$  coupling for duration  $\tau$

$$I_{x1} \xrightarrow[\tau]{2\pi\mathcal{J}I_{z1}I_{z2}} \cos(\pi\mathcal{J}\tau)I_{x1} + \sin(\pi\mathcal{J}\tau)[2I_{z1}I_{z2}, I_{x1}] = \cos(\pi\mathcal{J}\tau)I_{x1} + \sin(\pi\mathcal{J}\tau)2I_{y1}I_{z2}.$$

Hence by choosing the duration  $\tau$ , we can transform a single qubit state to a correlated state. A multi-qubit gate can be decomposed into a combination of single qubit gates and evolution under  $\mathcal{J}$ . The two-qubit CNOT gate with control on the first qubit and target on second qubit can be implemented in NMR by the pulse sequence (time ordered from right to left)

$$U_{\text{cnot}} = \left(\frac{\pi}{2}\right)_y^2(\tau) \left(\frac{\pi}{2}\right)_{-y}^2 \left(\frac{\pi}{2}\right)_{-x}^2 \left(\frac{\pi}{2}\right)_{-z}^1,$$

where  $\tau = 1/(2\mathcal{J}_{12})$  is the duration of free evolution under the internal Hamiltonian of the system  $H = 2\pi\mathcal{J}_{12}I_{z1}I_{z2}$ .

### 1.3.2 Pseudo-pure states

One of the primary requirements in many quantum information processing tasks is the initialization of the system into a desired state, which is most often a pure state [59]. In NMR, due to the extremely low purity factors, preparation of pure states requires unrealistically high magnetic fields or extremely low temperatures. Instead, one can prepare *pseudo-pure states* (PPS) which are of the form

$$\rho_{\text{pps}} = \left(\frac{1-\epsilon}{2}\right) \mathbb{1} + \epsilon|0\rangle\langle 0|. \quad (1.37)$$

Such a state has uniform background population in all states (captured by identity term), and slight excess population in the desired state ( $|0\rangle$  in the above case). The dynamics of a PPS is isomorphic to that of the corresponding pure state [6]. This can be intuitively understood from the form of Eq. 1.37 where identity term remains invariant under evolution and any interesting dynamics is the result of evolution of the other term with  $\epsilon$  purity. Moreover, the identity term does not contribute to the measured NMR signal.

A single qubit system is always in a pseudo-pure state. For two and more qubits, there are various techniques to prepare PPS including spatial averaging [6], temporal averaging [60], and

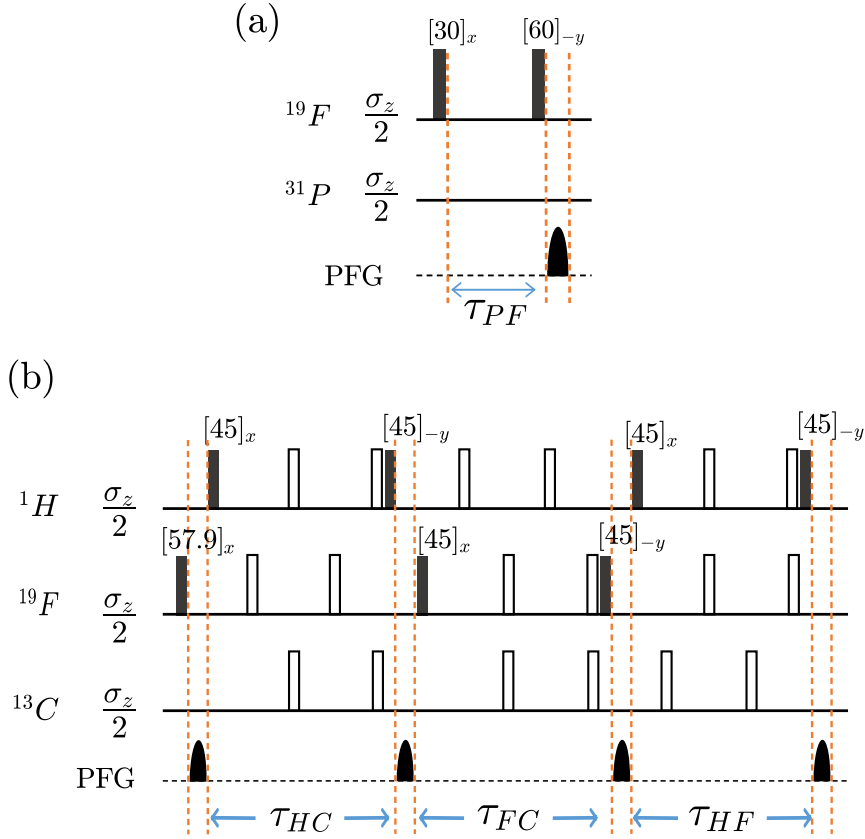


**Figure 1.5:** NMR pulse sequences (as reported in our publication [58]) for preparing PPS (a)  $|00\rangle\langle 00|$  of two qubit system  $^{19}\text{F}$  and  $^{31}\text{P}$  spins of sodium fluorophosphate molecule with  $\tau_{PF} = 1/(2\mathcal{J}_{PF})$  and (b)  $|000\rangle\langle 000|$  of three-qubit system  $^{13}\text{C}$ ,  $^1\text{H}$ , and  $^{19}\text{F}$  spins of dibromofluoromethane molecule with  $\tau_{HC} = 1/(2\mathcal{J}_{HC})$ ,  $\tau_{FC} = 2/|\mathcal{J}_{FC}| - 1/|2\mathcal{J}_{FC}|$ , and  $\tau_{HF} = 1/(2\mathcal{J}_{HF})$ , from thermal equilibrium. The solid bars represent rotations by an angle and about a direction as indicated over them. Blank rectangles represent  $\pi$  pulses and the black half ellipsoids represent PFG along  $+z$  axis to destroy coherences.

logical labelling [7]. We describe the spatial averaging technique which has been used in this thesis. This technique makes use of single and multi-qubit gate to transfer populations between different spin states. These naturally generate coherences, which are destroyed using gradients (PFG), and hence the name spatial averaging. For the two-qubit system formed by  $^{19}\text{F}$  and  $^{31}\text{P}$  nuclei of sodium fluorophosphate molecule and three-qubit system formed by  $^{13}\text{C}$ ,  $^1\text{H}$ , and  $^{19}\text{F}$  spins of dibromofluoromethane molecule used in this thesis, the pulse sequences which prepares PPS from thermal equilibrium are shown in Fig. 1.5. In the two-qubit system, such a sequence

transforms the thermal state as

$$\gamma_1 I_{z1} + \gamma_2 I_{z2} \xrightarrow{PPS} I_{z1} + I_{z2} + 2I_{z1}I_{z2} \equiv |00\rangle\langle 00|. \quad (1.38)$$

### 1.3.3 Measurement and readout

A crucial part of any information processing task is to estimate the state of the system at desired instances in time. Complete knowledge of the density matrix enables extraction of all information about the state, including populations and correlations. In NMR, as explained in Sec. 1.2.1.4, the sample has a net magnetization, which at thermal equilibrium is aligned parallel to the external field. When an RF pulse is applied to tilt it away from this direction, it begins to precess about the  $z$ -axis. In NMR architecture, RF receiver coils are in the transverse plane. Hence, as the magnetization precesses, it cuts through these coils generating a time-varying magnetic flux, which in turn induces an emf in the coils. However, due to inherent relaxation mechanisms, the measured signal decays with time, giving the *free induction decay* (FID) [48, 49]. This signal is proportional to

$$M(t) = \text{tr}[\rho(t)(\sigma_x + i\sigma_y)], \quad (1.39)$$

which gives the transverse magnetization components. The frequency spectrum is obtained by taking a Fourier transform of the time-domain FID signal. A schematic of the NMR spectrometer and components are shown in Fig. 1.6. At this juncture, it is important to note that in the measurement scheme of NMR, only *single quantum coherences* can be measured since the transitions are governed by selection rule  $\Delta m_s = \pm 1$  [49]. Hence, a single measurement is insufficient to provide information about populations and all the off-diagonal elements (coherences) of the density matrix. To estimate the complete density matrix, we employ *quantum state tomography* (QST) which involves a series of experiments from whose measurements all the elements of  $\rho(t)$  can be estimated [61, 62]. The intuitive idea of QST is to apply unitary operations which will transfer information about populations and different coherence orders to the single quantum coherence order (or the measurement basis in the architecture used), which is then experimentally measured. This is akin to measuring in different bases, since unitary rotations on the state are simply basis transformations. The series of measurements gives a set of linear equations in the elements of  $\rho(t)$ , which is solved to individually estimate each density matrix element. Detailed

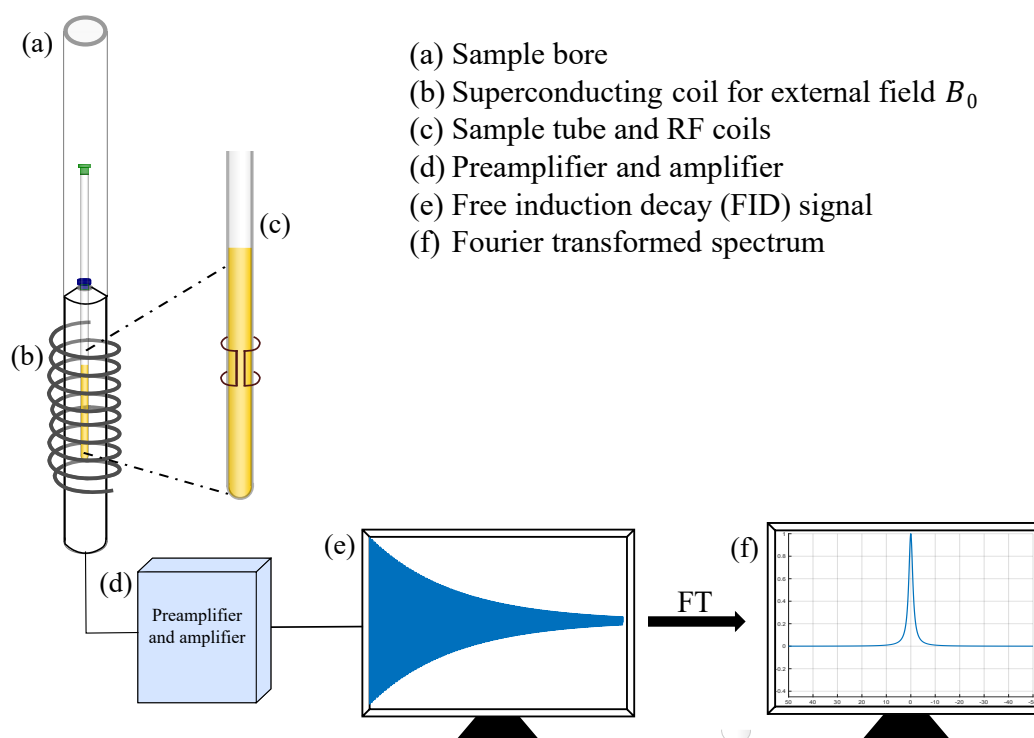


**Figure 1.6:** Schematic of a NMR spectrometer. The sample is inserted through a bore (a), where it sits in a region of uniform external magnetic field  $B_0$  generated by a superconducting coil (b). The RF coils lie inside, closer to the sample (c). The preamplifier and amplifier (d) help apply pulses and collect the signal from the sample. The FID signal (e) collected from the sample is Fourier transformed to get the frequency spectrum (f).

information of the QST experiments used in this thesis are given in the Appendix A.2.

## 1.4 Nonlinear dynamics using NMR

Nonlinearity is a fundamental concept describing functions whose dependent variables do not vary linearly with the independent variables, mathematically defined by behaviours  $f(x + y) \neq f(x) + f(y)$  and  $f(\alpha x) \neq \alpha f(x)$ . It is essentially true of systems characterized by multiple parameters and interactions ranging from celestial bodies, coupled oscillators, chemical reactant concentrations, atmospheric systems, to predator-prey models, population dynamics, circadian rhythms, economies, markets, and stocks [63–66]. The ubiquity of nonlinear effects in classical mechanics prompts the question - how does nonlinearity manifest in the quantum domain? This is a natural curiosity that arises in the light of Bohr's correspondence principle which says that

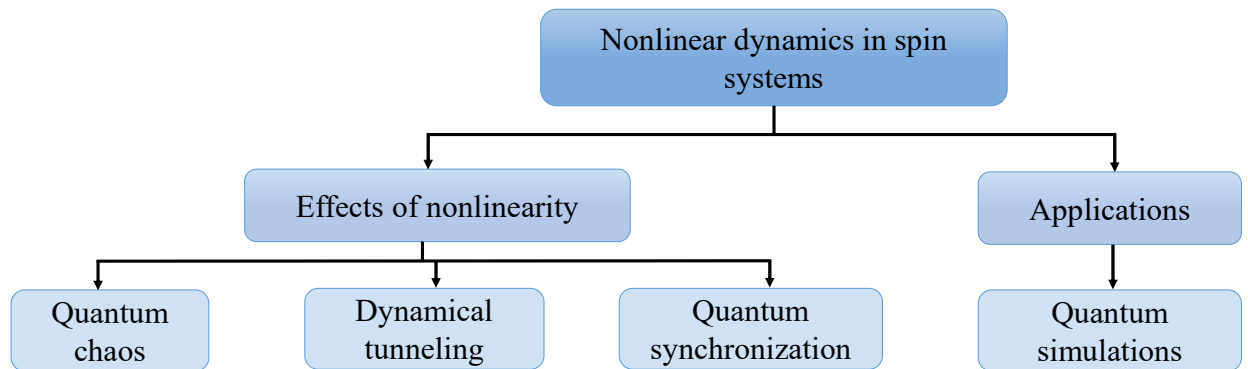


**Figure 1.7:** A brief overview of the thesis. We have studied some fundamental effects of nonlinearity such as quantum chaos, dynamical tunneling and quantum synchronization. From an application perspective, we have studied the role of nonlinear interactions in simulating quantum dynamics of Rydberg atoms.

classical mechanics is a limiting case of quantum mechanics. However, a direct extension of classical principles of nonlinearity to the quantum regime is not straightforward since the dynamics are governed by the Schrodinger equation, which is *linear*. There have been developments to include nonlinear principles in quantum dynamics such as the nonlinear Schrodinger equation, Gross-Pitaevskii equation, Hatree-Fock approximation, etc. In this thesis, we study this subject from the aspect of nonlinearity in the *Hamiltonian operators* under which the system evolves, and the effects that arise therein. These can be simulated in nuclear spin systems by a combination of RF pulses and scalar spin- $\mathcal{J}$  coupling interactions. Hence, using the concepts of NMR and quantum information processing introduced here, we study the following topics:

- (i) Quantum chaos in small and large spin registers
- (ii) Dynamical tunneling
- (iii) Quantum phase-synchronization
- (iv) Simulating interaction induced Rydberg blockade and freezing in spin systems, as shown in the flowchart in Fig. 1.7.

## CHAPTER 2

---

### Quantum chaos in a two-qubit kicked top

---

#### Abstract

In this chapter, we experimentally study chaos in a two-qubit system comprising of a pair of spin-1/2 nuclei using the quantum kicked top model in nuclear magnetic resonance architecture. We simulate the kicked top by a series of linear kicks realized using radio-frequency pulses, and the nonlinear interaction realized using indirect spin-spin coupling. After a variable number of kicks, we employ quantum state tomography to reconstruct the single-qubit reduced density matrices, using which we extract von Neumann entropies and Husimi distributions. These measures enable the study of correspondence with classical phase space as well as probing distinct features of quantum chaos, such as symmetries and temporal periodicity in the two-qubit kicked top.

#### Reported in

**V. R. Krithika**, V. S. Anjusha, Udaysinh T. Bhosale and T. S. Mahesh, *NMR studies of quantum chaos in a two-qubit kicked top*, [Phys. Rev. E 99, 032219 \(2019\)](#).

## 2.1 Introduction

Chaos is one of the hallmarks of nonlinear systems. Classical chaos is an extremely well studied field in physics, both theoretically and experimentally. Classically chaotic systems are deterministic systems, with exact equations of motion to describe the evolution of system parameters, but are nonetheless unpredictable over long time scales [63]. Such systems exhibit extreme sensitivity to initial conditions and are characterized by Lyapunov exponents which capture the exponential divergence of nearby trajectories. Nonlinear systems are ubiquitous, and chaos has been shown to have far-reaching applications beyond physics, in fields ranging from biology, chemistry, earth

science to finances [63, 65, 66].

A natural extension of classical chaos is to the quantum domain following Bohr's correspondence principle, which states that classical mechanics is a limiting case of quantum mechanics [67, 68]. This prompts the question - are there signatures of chaos in the quantum regime? If so, how do we study them? It might seem that a direct extension of the principles of classical chaos to quantum mechanics would be straightforward. That is however not the case due to two main constraints (i) the uncertainty principle in quantum mechanics which renders it impossible to estimate system parameters simultaneously at the initial instant and at later times with arbitrary precision, and (ii) quantum dynamics is governed by the Schrodinger equation, which is linear and preserves the overlap of states. Hence, contrary to classical trajectories diverging exponentially, quantum dynamics preserves the overlap between states, i.e., the overlap within an initial pair of states is equal to that of the transformed pair. The bridge between classical chaotic systems and their quantum counterparts has thus been a major subject of study both theoretically and experimentally [68–84].

Understanding quantum chaos is not only of interest from fundamental perspectives, but is also crucial for building operable quantum computers. Studies have probed the interplay of quantum chaos with quantum algorithms [85–87], and have also shown that chaotic interactions in a system can have deleterious effects on the functionality of quantum computers [88–90]. Since classical measures of chaos cannot be extended to the quantum domain, quantum chaos needs to be defined and characterized by inherent quantum mechanical properties. Signatures of quantum chaos have been studied using various quantities like entanglement [91–95], Lyapunov exponents and Husimi probability distributions [96], the dynamics of quantum discord [97], level statistics of chaotic Hamiltonians [72, 98], the dynamics of open quantum systems undergoing continuous quantum measurement [99], etc. Quantum chaos has also investigated for its relation with other phenomena in quantum systems such as decoherence [100–109], and thermalization [81, 110–118]. More recently, the relation between quantum chaos and out-of-time-order correlations has gained immense attention [119–132].

Quantum chaos has been studied in a host of models such as billiards, kicked rotor, etc. [133–142]. In this work, we use the kicked top model, which is apt for spin systems. This model is a classic example for studying chaos, which shows transition from regular to chaotic behaviour as a

function of the chaoticity parameter. It has been studied theoretically [72, 91–94, 143–149], and has also been realized experimentally in various systems including laser-cooled cesium atoms [78] and superconducting circuits [81]. Recently, the kicked top consisting of just two qubits, which is in a deep quantum regime, has also been studied theoretically in detail [93, 150]. It has been shown that the model is exactly solvable for up to four qubits [148]. In this work, we use nuclear magnetic resonance (NMR) as the experimental platform to study quantum chaos. NMR is a versatile technique that offers long coherence times, precise control over spin dynamics, and efficient readout of output states [49]. It has been a successful test bed for implementing various quantum information processing tasks and for understanding quantum correlations [52, 53].

## 2.2 Objectives

In this project, we study quantum chaos in a two-qubit system formed by a pair of spin-1/2 nuclei in NMR architecture. We implement the quantum kicked top (QKT) Hamiltonian using spin-spin interaction between two nuclear spins as the nonlinear evolution and intermittent radio-frequency pulses as linear kicks. We initialize the system to different initial conditions and system parameters. Following this, we

- (i) Apply variable number of kicks and characterize the final state via quantum state tomography from which we obtain the von Neumann entropy
- (ii) Capture the signatures of correspondence between the classical phase space and the quantum dynamics using entanglement as a witness via the time averaged von Neumann entropy
- (iii) Further analyse the single qubit Husimi distributions to understand the contrasting dynamics between regular and chaotic regions in the quantum regime.

These studies help us understand and characterize the behaviour of systems in the deep quantum regime, and thereby aid in building efficient quantum protocols for quantum computing and information processing tasks.

## 2.3 Quantum Kicked top

We first introduce the quantum kicked top (QKT) model [72, 151] and its classical limit. The quantum kicked top is described by the piecewise Hamiltonian consisting of periodic linear  $x$

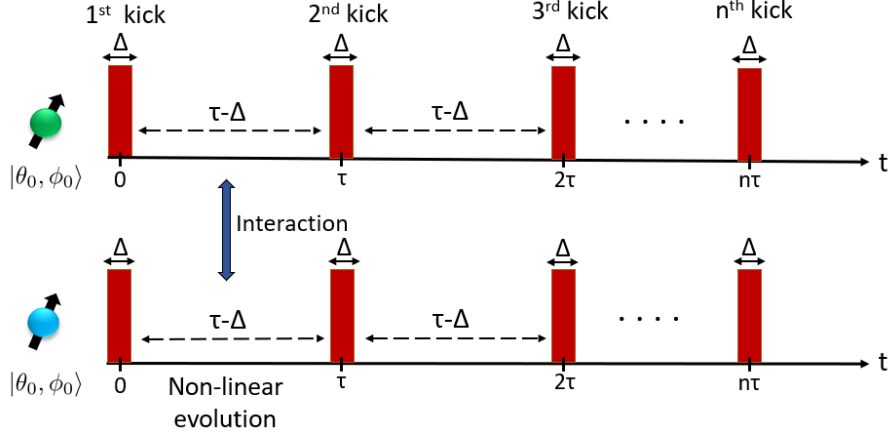


**Figure 2.1:** Schematic of the quantum kicked top model for a two-qubit system, initialized into a coherent state  $|\theta_0, \phi_0\rangle \otimes |\theta_0, \phi_0\rangle$ . The filled rectangles represent linear kicks, which together with the nonlinear evolutions simulate a QKT.

kicks of width  $\Delta$  and strength  $p$  separated by nonlinear evolutions each of an interval  $\tau \gg \Delta$  (see Fig. 2.1)

$$\begin{aligned}
 H(t) &= pJ_x, \text{ for } t \in \left[ n\tau - \frac{\Delta}{2}, n\tau + \frac{\Delta}{2} \right] \text{ and} \\
 H(t) &= \frac{k}{2j\tau} J_z^2, \text{ otherwise}
 \end{aligned} \tag{2.1}$$

where  $\mathbf{J} = [J_x, J_y, J_z]$  is the total angular momentum vector. The value of  $\hbar$  has been set to 1. The time lapse of the  $n$ -th kick is given by  $[n\tau - \frac{\Delta}{2}, n\tau + \frac{\Delta}{2}]$ . The nonlinear term in Eq. 2.1 describes a torsion about the  $z$  axis wherein  $k$  is the chaoticity parameter and  $j$  is the total spin size. A spin- $j$  QKT can be simulated using  $2j$  number of qubits which are symmetric under exchange, a property which has earlier been used to study various quantum correlations [97]. We simulate a QKT of  $j = 1$  using a pair of interacting qubits. We set  $p\Delta = \pi/2$  to simplify the quantum and classical maps [94, 151]. The time evolution of the system is governed by the Floquet unitaries

$$U_{\text{kick}} = e^{-i\frac{\pi}{2}J_x}, \quad U_{\text{NL}} = e^{-i\frac{k}{2j}J_z^2}, \quad \text{and } U_{\text{QKT}} = U_{\text{NL}}U_{\text{kick}}. \tag{2.2}$$

The overall unitary  $U_{\text{QKT}}$  is applied repeatedly to realize the desired number of kicks. In the Heisenberg picture, the evolution of the angular momentum operator for any time step is given

by [94]

$$\mathbf{J}' = U_{\text{QKT}}^\dagger \mathbf{J} U_{\text{QKT}}. \quad (2.3)$$

The  $x$  and  $y$  components of  $\mathbf{J}$  can be expressed in terms of raising and lowering operators as  $J_x = (J_+ + J_-)/2$  and  $J_y = (J_+ - J_-)/2i$ , which can then be studied in the  $J_z$  eigenbasis  $\{|m\rangle\}$  following the ladder equations

$$J_+|m\rangle = c_m|m+1\rangle \text{ and } J_-|m\rangle = d_m|m-1\rangle. \quad (2.4)$$

We first show the calculation of  $J_+$  component evolution since  $J_-$  will simply be its Hermitian conjugate (H.c):

$$\mathbf{J}'_+ = U_{\text{QKT}}^\dagger \mathbf{J}_+ U_{\text{QKT}} = U_{\text{kick}}^\dagger U_{\text{NL}}^\dagger J_+ U_{\text{NL}} U_{\text{kick}}. \quad (2.5)$$

The action of  $U_{\text{NL}}$  on the operator  $J_+$  in the  $|m\rangle$  basis can be computed as

$$\begin{aligned} \langle m|U_{\text{NL}}^\dagger J_+ U_{\text{NL}}|n\rangle &= \langle m|e^{i\frac{k}{2j}J_z^2} J_+ e^{-i\frac{k}{2j}J_z^2}|n\rangle \\ &= \exp\left\{i\frac{k}{2j}(m^2 - n^2)\right\} \langle m|J_+|n\rangle \\ &= \exp\left\{i\frac{k}{2j}(m^2 - n^2)\right\} c_n \delta_{m,n+1} \\ &= \begin{cases} e^{i\frac{k}{j}(n+\frac{1}{2})} c_n, & \text{if } m = n + 1, \\ 0, & \text{otherwise} \end{cases} \\ &= \langle m|J_+ e^{i\frac{k}{j}(J_z+\frac{1}{2})}|n\rangle, \end{aligned} \quad (2.6)$$

so that

$$U_{\text{NL}}^\dagger J_+ U_{\text{NL}} = J_+ e^{i\frac{k}{j}(J_z+\frac{1}{2})}. \quad (2.7)$$

Following this, the kick Floquet unitary is applied on the above operator. The action of the kick unitary is to bring about a clockwise rotation of angle  $\pi/2$  about the  $x$  axis giving  $U_{\text{kick}}^\dagger (J_x, J_y, J_z) U_{\text{kick}} = (J_x, -J_z, J_y)$ , which gives

$$\begin{aligned} J'_+ &= U_{\text{QKT}}^\dagger J_+ U_{\text{QKT}} = U_{\text{kick}}^\dagger J_+ e^{i\frac{k}{j}(J_z+\frac{1}{2})} U_{\text{kick}} \\ &= (J_x - iJ_z) e^{i\frac{k}{j}(J_y+\frac{1}{2})}. \end{aligned} \quad (2.8)$$

The transverse components of the angular momentum operator after one iteration of QKT evolution are thus

$$\begin{aligned} J'_x &= \frac{J'_+ + J'_-}{2} = \frac{1}{2} \left[ (J_x - iJ_z) e^{i\frac{k}{j}(J_y + \frac{1}{2})} + H.c. \right], \\ J'_y &= \frac{J'_+ - J'_-}{2i} = \frac{1}{2i} \left[ (J_x - iJ_z) e^{i\frac{k}{j}(J_y + \frac{1}{2})} - H.c. \right]. \end{aligned} \quad (2.9)$$

The  $J_z$  component of angular momentum operator commutes with the nonlinear Floquet unitary and hence remains invariant under the unitary  $U_{\text{NL}}$ . It however evolves under the kick unitary which causes a  $\pi/2$  rotation about the  $x$  axis giving  $U_{\text{kick}}^\dagger J_z U_{\text{kick}} = J_y$ , such that

$$J'_z = J_y. \quad (2.10)$$

Eqs. 2.9 and 2.10 describe the evolution of the components of the angular momentum operator in the QKT model. In the following section, we study the classical limit of QKT .

### 2.3.1 Classical limit of QKT

It is insightful to first look into the classical behaviour of the QKT in the semiclassical limit, i.e.,  $j \rightarrow \infty$ . Scaling the variables as  $X = J_x/j$ ,  $Y = J_y/j$ , and  $Z = J_z/j$ , we obtain the commutation relation  $[X, Y] = iZ/j$ , which vanishes in the large  $j$  limit. In this classical limit, Eqs. 2.9 and 2.10 give the iterative map [94, 151]

$$\begin{aligned} X' &= X \cos(kY) + Z \sin(kY), \\ Y' &= X \sin(kY) - Z \cos(kY), \\ Z' &= Y. \end{aligned} \quad (2.11)$$

Since the total angular momentum of the system is conserved, these components can be parametrized in terms of polar coordinates  $(\theta, \phi)$  as  $X = \sin \theta \cos \phi$ ,  $Y = \sin \theta \sin \phi$ , and  $Z = \cos \theta$ . The nature of the phase space is determined by the chaoticity parameter  $k$ , and as the value of  $k$  increases, the phase space undergoes a transition from regular to a combination of regular and chaotic regions before becoming predominantly chaotic for large values of  $k$ . The

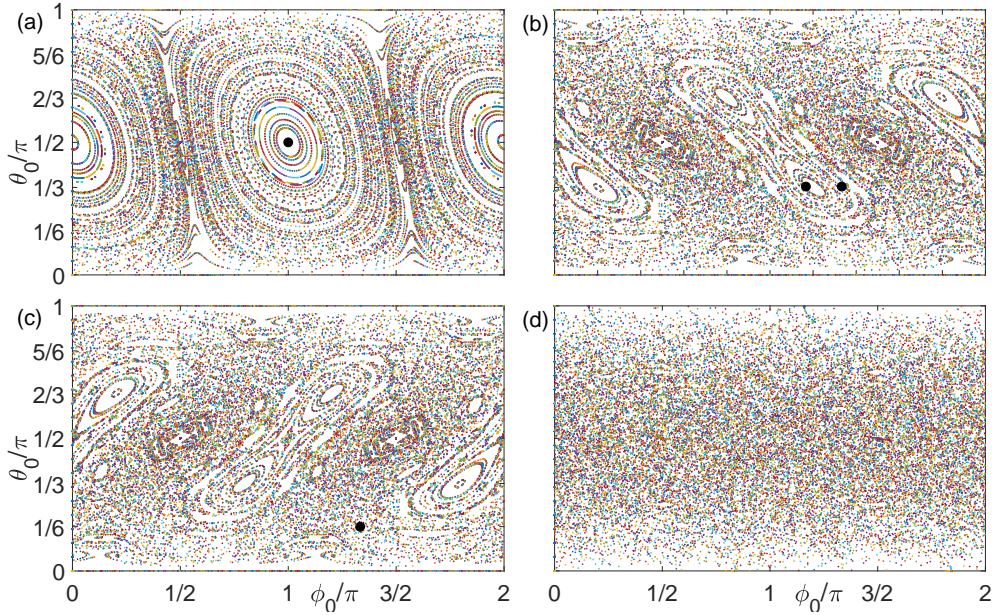


**Figure 2.2:** Classical trajectories of the kicked top in  $|\theta, \phi\rangle$  phase space for chaoticity parameter values (a)  $k = 0.5$ , (b)  $k = 2.5$ , (c)  $k = -2.5$ , and (d)  $k = 2\pi + 2.5$ . The phase space points chosen for detailed analysis are marked by black dots.

classical phase space for different values of  $k$  is shown in Fig. 2.2. The trivial fixed points at  $(\theta, \phi) = (\pi/2, 0)$  and  $(\pi/2, \pi)$  which can be seen in Fig. 2.2(a) for  $k = 0.5$  become unstable at  $k = 2$ . At  $k = 2$  new fixed points are born and they move away as  $k$  is increased as shown in Fig. 2.2(b). For large values of  $k > 5$  the phase space becomes mostly chaotic as shown in Fig. 2.2(d).

## 2.4 QKT with a pair of NMR qubits

In this section, we explain how the QKT model can be implemented in a pair of NMR qubits. We consider a kicked top of spin  $j = 1$  realized using a pair of interacting qubits with spin angular momentum operators  $I_1$  and  $I_2$  respectively. Denoting the total  $z$  component of the system as  $J_z = I_{z1} + I_{z2}$ , we can expand the nonlinear term as  $J_z^2 = \mathbb{1}/4 + \mathbb{1}/4 + 2I_{z1}I_{z2}$ . The identity terms only introduce global phases in the evolution, and can hence be dropped. The nonlinear dynamics can thus be realized using the bilinear term  $2I_{z1}I_{z2}$ . Such an interaction occurs naturally in a pair of coupled nuclear spins via indirect spin-spin interaction under weak-coupling limit [49], i.e.,

$$H_{\mathcal{J}} = 2\pi\mathcal{J}I_{z1}I_{z2}. \quad (2.12)$$

Here  $\mathcal{J}$  is the strength of the indirect spin-spin coupling. The estimation of  $\mathcal{J}$  in a two-qubit system is explained in detail in the Appendix A.3. The spins also interact with the external magnetic field via Zeeman interaction. For an external field  $\mathbf{B} = B_0\hat{z}$ , the spins precess about the magnetic field with Larmor frequency  $\omega_i = \gamma_i B_0$ , where  $\gamma_i$  is the gyromagnetic ratio of the  $i$ -th spin species [49]. For a pair of heteronuclear spins, these Zeeman Hamiltonian can be ignored by moving to a doubly rotating frame resonant with the Larmor frequencies of the individual spins. Comparing Eq. 2.12 with the nonlinear term in Eq. 2.1, we obtain  $k = 2\pi\mathcal{J}\tau$ .

The linear kicks are realized using radio-frequency (RF) pulses with the Hamiltonian

$$H_{\text{rf}} = \frac{\pi}{2\Delta}(I_{x1} + I_{x2}), \quad (2.13)$$

on both the qubits. Comparing this with the linear term in Eq. 2.1, we choose  $\pi/(2\Delta) = p$ . The RF pulse duration  $\Delta \ll k/(2\pi\mathcal{J}) = \tau$ , the duration of nonlinear evolution corresponding to the chaoticity parameter  $k$  (see Fig. 2.1). Thus in our experiment,  $U_{\text{kick}} = \exp(-iH_{\text{rf}}\Delta)$ ,  $U_{\text{NL}} = \exp(-iH_{\mathcal{J}}\tau)$ , which helps realize the QKT Floquet  $U_{\text{QKT}} = U_{\text{NL}}U_{\text{kick}}$  (see Eq. 2.2) using a pair of qubits.

### 2.4.1 Experimental Setup

In our experiments, the pair of qubits was formed by  $^{19}\text{F}$  and  $^{31}\text{P}$  spins of sodium fluorophosphate molecules dissolved in  $\text{D}_2\text{O}$  (5.3 mg in 600  $\mu\text{l}$ ) shown in Fig. 2.3. All the experiments were performed on a 500 MHz Bruker NMR spectrometer at ambient temperatures and on-resonant conditions. The indirect spin-spin coupling constant in this system was  $\mathcal{J} = 868$  Hz. The experiments consisted of two parts, i.e., preparation of initial states  $(\theta_0, \phi_0)$ , followed by simulating the QKT unitary, as illustrated in Fig. 2.1.

In NMR systems, owing to the low nuclear polarization at an ambient temperature  $T$  and a typical external field  $B_0$ , the initial thermal equilibrium state

$$\rho_0 = \frac{\mathbb{1}}{4} + \epsilon\tilde{\rho}$$

is in a highly mixed state with a low purity factor  $\epsilon = \hbar B_0/(2^n k_B T) \sim 10^{-5}$ , which accounts for a finite nuclear magnetization. The uniform background population represented by identity remains

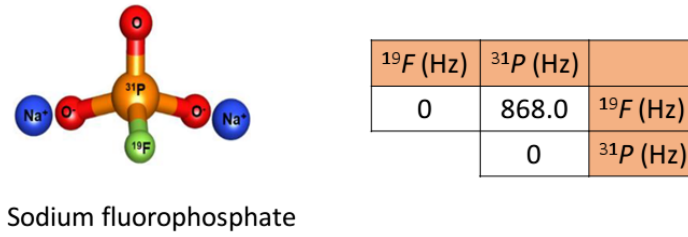


**Figure 2.3:** Sodium fluorophosphate molecule comprising the two-qubit  $^{19}\text{F}$  and  $^{31}\text{P}$  system. The table shows the Hamiltonian parameters of the system, with diagonal elements indicating offsets, and off-diagonal element indicating scalar  $\mathcal{J}$  coupling constant.

invariant under unitary evolution while the traceless deviation density matrix  $\tilde{\rho} = \gamma_1 I_{z1} + \gamma_2 I_{z2}$  evolves and captures all the interesting dynamics. Preparing a pure state in NMR systems requires very low temperatures and unrealistically high magnetic fields. The routine protocol thus involves preparing a pseudopure state [6], which is isomorphic to pure states and mimics their dynamics, as explained in Sec. 1.3.

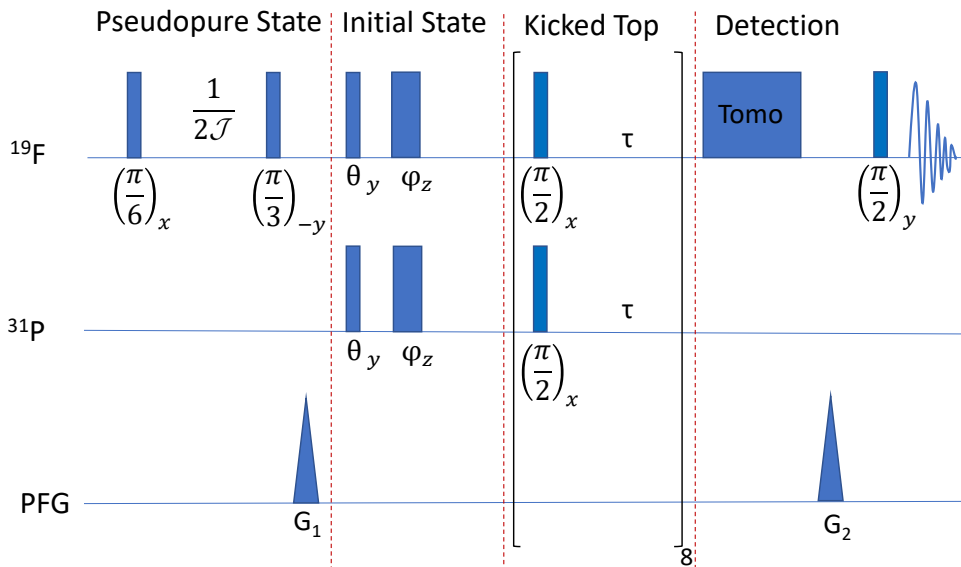


**Figure 2.4:** NMR pulse sequence for simulating a QKT in a two-qubit system. The flip angles and phases (subscripts) are shown under each radio-frequency pulse. Here  $G_1$  and  $G_2$  correspond to pulsed-field-gradients (PFG).

The NMR sequence for the entire experiment is shown in Fig. 2.4. We use the  $\{|0\rangle, |1\rangle\}$  eigenbasis of  $I_z$  as the computational basis. First, we prepared the pseudopure state equivalent to  $|00\rangle$  by transforming  $\tilde{\rho}$  into  $I_{z1} + I_{z2} + 2I_{z1}I_{z2}$  using spatial averaging technique with a pair of RF

pulses followed by a pulsed field gradient (PFG), which introduces a spatially inhomogeneous magnetic field across the sample volume, thereby destroying any transverse components of the magnetization.

After preparing the pseudopure state, we initialized the system into spin-coherent states since they are closest to a classical state [152, 153]. The spin coherent states were prepared by a  $\theta_y$  pulse followed by a  $\phi_z$  rotation (as shown in Fig. 2.4) which prepares the two qubits in the state

$$\rho_{\theta,\phi} \approx (1 - \epsilon) \frac{\mathbb{1}}{4} + \epsilon [|\theta, \phi\rangle\langle\theta, \phi| \otimes |\theta, \phi\rangle\langle\theta, \phi|], \quad (2.14)$$

where

$$|\theta, \phi\rangle = \cos(\theta/2)|0\rangle + e^{i\phi} \sin(\theta/2)|1\rangle \quad (2.15)$$

is the corresponding Bloch vector for each qubit. In the classical limit, the above initialization is analogous to initializing the kicked top into the point  $(\theta, \phi)$  on the phase space. The  $\phi_z$  pulses for different angles were generated by an optimal control technique [154].

Subsequently, we implemented the QKT unitary  $U_{\text{QKT}}$  using RF pulses of duration  $\Delta$  and evolution under the interaction between the qubits for duration  $\tau$ , as explained in Sec. 2.4. The Floquet unitary  $U_{\text{QKT}}$  was applied up to  $n$  times and the reduced density operator of  $^{19}\text{F}$   $\rho_n = \text{Tr}_{\text{P}}[U_{\text{QKT}}^n \rho_{\theta,\phi} U_{\text{QKT}}^{n\dagger}]$  was estimated using single-qubit pure-phase quantum state tomography [155]. The tomography protocol consisted of three NMR experiments: (i) A PFG to destroy all the coherences followed by a  $(\pi/2)_y$  pulse to obtain the diagonal elements of the density matrix; (ii)  $(\pi/2)_{-y}$  pulse followed by a PFG and  $(\pi/2)_y$  pulse to obtain the real part of the off-diagonal coherence element; (iii)  $(\pi/2)_{-x}$  pulse followed by a PFG and  $(\pi/2)_y$  pulse to obtain the imaginary part of the off-diagonal coherence element. In this way, the single-qubit deviation density matrix  $\tilde{\rho}_n$  can be reconstructed from only the pure-phase NMR signals, which are easy to quantify.

## 2.4.2 Probing quantum chaos via von Neumann entropy

In this section, we explain the characterization of quantum chaos in a two-qubit system using von Neumann entropy measure. It has been observed that a kicked top initialized in a state corresponding to a classically chaotic region results in higher entanglement production [91, 94].

Of course, since we are considering closed quantum dynamics, the full system remains pure and the entropy of the entire system remains invariant under QKT dynamics. However, the qubits can get entangled during the evolution, which will result in a reduced single-qubit state that has higher mixedness than the composite system. The degree of entanglement, and hence the degree of chaos, can then be quantified by the von Neumann entropy given by

$$S(\rho_n) = - \sum_{\lambda_{\pm} \neq 0} \lambda_{\pm} \log_2 \lambda_{\pm} \quad (2.16)$$

of the reduced density operator  $\rho_n$  with eigenvalues  $\lambda_{\pm} = (1 \pm \epsilon \alpha_n)/2$ . Here,  $\pm \alpha_n$  are eigenvalues of the traceless deviation density matrix  $\rho_n$ . However, in low-purity conditions, the von Neumann entropy is already close to unity,

$$S(\rho_n) \cong 1 - \epsilon^2 \alpha_n^2,$$

due to the dominant contribution of the identity term in  $\rho_n$ . Consequently, the contrast in the entropy between regular and chaotic regions is low. In order to address this issue, we define an  $n$ -kick order parameter

$$s_n = \frac{1 - \frac{1}{n} \sum_{m=1}^n S(\rho_m)}{\epsilon^2} \cong \langle \alpha_n^2 \rangle, \quad (2.17)$$

which extracts information from only the deviation part after different number of kicks, and hence serves as a convenient measure of chaos. Smaller values of the order parameter correspond to higher chaoticity and larger order parameter values indicate higher regularity. We use this order parameter to characterize the QKT dynamics of the two-qubit system.

## 2.5 Results and Discussion

We now present the experimental results for the two-qubit NMR system. We carried out four sets of experiments for chaoticity parameter values  $k \in \{0.5, 2.5, 2\pi - 2.5, 2\pi + 2.5\}$ . Following the experimental sequence shown in Fig. 2.4, we initialized the system into different initial spin coherent states and then applied the QKT evolution for  $n$ -kicks, and finally estimated the single-qubit reduced density matrix via quantum state tomography. To evaluate the effectiveness of the

experimental protocol, we estimated the state fidelity [156]

$$F(\tilde{\rho}_n, \tilde{\rho}_n^{\text{th}}) = \frac{\text{Tr}[\tilde{\rho}_n \tilde{\rho}_n^{\text{th}}]}{\sqrt{\text{Tr}[\tilde{\rho}_n^2] \text{Tr}[(\tilde{\rho}_n^{\text{th}})^2]}} \quad (2.18)$$

of the  $n$ -kick experimental state  $\tilde{\rho}_n$  with the corresponding theoretical deviation state  $\tilde{\rho}_n^{\text{th}}$  for all initialization points  $(\theta, \phi)$  and for all  $k$  values. The average fidelity versus kick number is displayed in Fig. 2.5 which indicates high fidelities of above 0.95 up to six kicks and above 0.8 up to eight kicks. We hence restricted the number of QKT iterations in the system to eight.

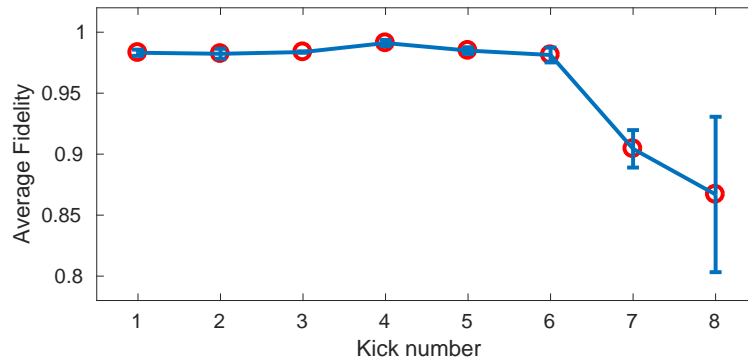


**Figure 2.5:** Average fidelity of the experimental states for various kick numbers. The error bars indicate one standard deviation of distribution.

Next, using experimental data we reconstructed the reduced density matrix and estimated the order parameter  $s_n$  for the number  $n$  of kicks ranging from 1 to 8. The contours the experimental order parameter  $s_n$  for various values of  $n$  and chaoticity parameter values  $k$  are displayed in Fig. 2.6. The colour background in each plot was obtained from numerical simulation and is provided as a comparison for experimental data. The average rms deviation  $\delta$  between the experimental and simulated values were calculated to be (i) 0.14 for  $k = 0.5$ , (ii) 0.033 for  $k = 2.5$ , (iii) 0.031 for  $k = 2\pi - 2.5$ , and (iv) 0.032 for  $k = 2\pi + 2.5$ . The experimental and simulated values hence seemed to be in general agreement.

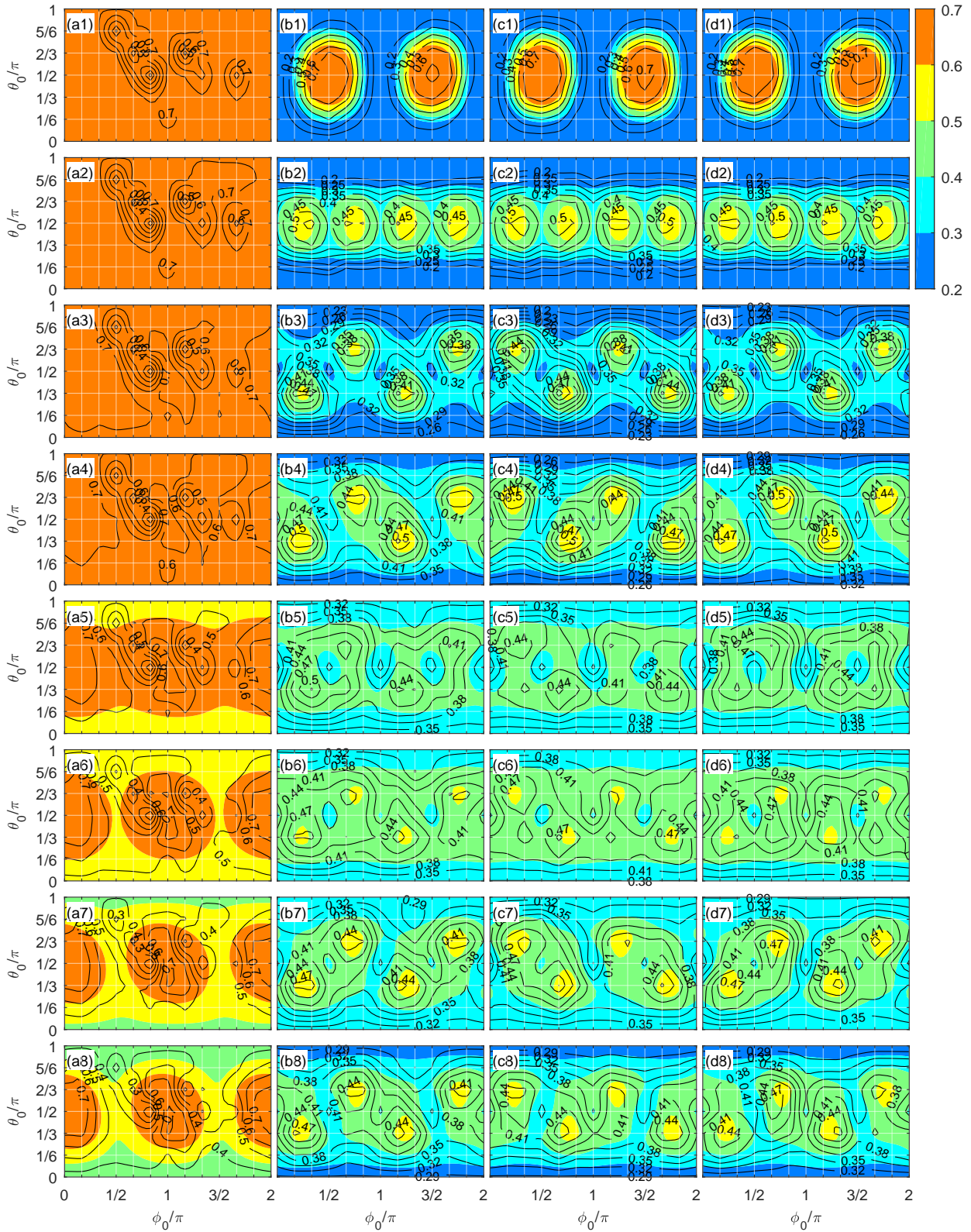


**Figure 2.6:** Contours represent experimental order parameter averaged over  $n$  kicks ( $s_n$ ) for chaoticity parameter  $k = 0.5$  [(a1)–(a8)],  $k = 2.5$  [(b1)–(b8)],  $k = 2\pi - 2.5$  [(c1)–(c8)], and  $k = 2\pi + 2.5$  [(d1)–(d8)]. Background colour maps represent the corresponding simulated values.

For one kick at  $k = 0.5$  we observed almost uniformly high order parameter  $s > 0.6$ , while for other  $k$  values, we observed similar patterns with a pair of highly ordered regular islands. Gradually, with increasing number of kicks, the averaged order parameter settled to a characteristic pattern that resembled the corresponding classical phase space, except for  $k = 2\pi + 2.5$ . Ultimately, we obtained domains of regular islands corresponding to high order parameter for all  $k$  values. In accordance with expectation, we observed overall high order parameters for  $k = 0.5$ . On the other hand, for the high value  $k = 2\pi + 2.5$ , unlike the classical phase space which is highly chaotic, in the quantum scenario, the regular islands survived. This feature can be attributed to the periodicity of the order parameter with respect to the chaoticity parameter, i.e.,  $s(k) = s(\text{mod}(k, 2\pi))$  for the two-qubit ( $j = 1$ ) case considered here. This was evident from the similarity between the contours of columns 2 and 4 in Fig. 2.6 as well as from the reflection symmetry between the columns 2 (or 4) and 3. The periodicity of entropy distribution as a function of chaoticity parameter  $k$  and the number of qubits has been theoretically studied in detail in [150].

The results presented in Fig. 2.6 show clear distinction in the values of the order parameter between regular and chaotic regions. For all values of  $k$ , we observed that the time-averaged order parameter for regular regions was higher than that of chaotic regions. This in turn reinforces the fact that the time averaged entropy of regular regions is lesser than that of chaotic regions. It is evident that the time-averaged order parameter could capture the correspondences and deviations between classical and quantum behaviour under QKT dynamics. Theoretical studies of von Neumann entropy in the deep quantum regime with mixed phase space [92, 147] have shown that there are instances where entropy of initial states in regular regions leads to high entanglement generation. However, its time average were shown to be less than that of the chaotic region [92], which is in agreement with our NMR experiments. Hence, time-averaged order parameter (and hence time-averaged entropy) serves as a good witness for quantum chaos.

### 2.5.1 Husimi probability distribution

The von Neumann entropy captures the entanglement between the qubits that constitute the QKT. However, it is not sensitive to the angular location of the single-qubit reduced state on the Bloch sphere. The Husimi probability distribution function measures the overlap of reduced state  $\rho_n$

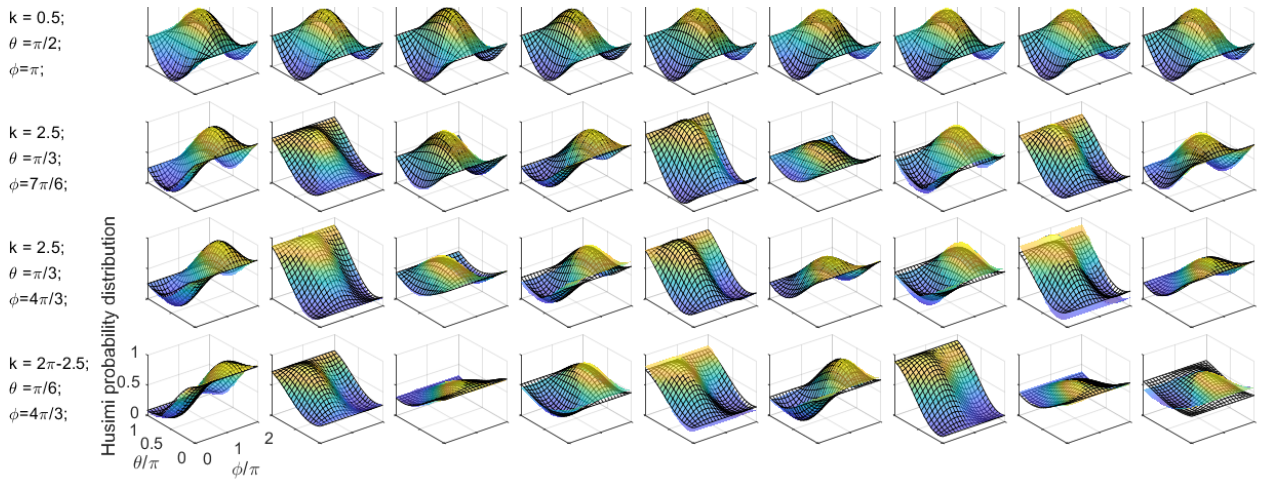


**Figure 2.7:** Experimental (mesh grids) and simulated (color background) Husimi probability distributions (in units of  $1/\pi$ ) for certain  $k$  values and initial states (as indicated in the left of each row) after kick numbers  $n = 0$  to 8 (from left to right).

with Bloch vectors  $\{|\theta, \phi\rangle\}$  on the phase space, and is defined as [157, 158]

$$Q(\theta, \phi, n) = \frac{1}{\pi} \langle \theta, \phi | \rho_n | \theta, \phi \rangle. \quad (2.19)$$

Using the Husimi probability distribution function, we could visualize the dynamics of the reduced state as it evolved under the QKT unitary. The results of the normalized Husimi distributions for select values of  $k$  and initial states are shown in Fig. 2.7. Here the mesh-grid lines represent the experimental distribution while the color background represents the numerically simulated distribution. A state initialized in a regular region had a corresponding Husimi probability distribution that is either stationary or highly periodic. This is clearly evident for the state initialized at  $|\pi/2, \pi\rangle$  for  $k = 0.5$  which lies in the high-order parameter region, and whose distribution remained localized throughout the evolution time. On the other hand, for a state initialized into a chaotic region, the distribution showed more intricate dynamics. The distribution corresponding to such states showed periodic temporal modulations and exhibited significant delocalization over the Bloch sphere.

To capture the delocalization better, we tracked the dynamics of the first 20 extrema, that is, the values closest to the highest and lowest values of the normalized Husimi probability distribution. As shown in Fig. 2.8, the extrema regions for  $k = 0.5$  were localized after the evolution, whereas they spread out on the phase space for higher values of  $k$ . Interestingly, the mismatch

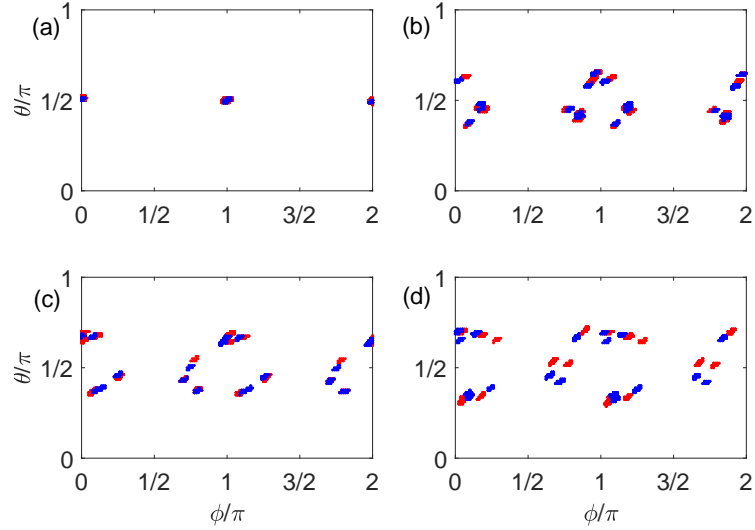


**Figure 2.8:** Distribution of extrema neighborhood of Husimi probability function on the Bloch sphere. Blue dots represent simulated data and red dots represent experimental data for the values of  $k$  and initial angles (a)  $k = 0.5, |\pi/2, \pi\rangle$ , (b)  $k = 2.5, |\pi/3, 7\pi/6\rangle$ , (c)  $k = 2.5, |\pi/3, 4\pi/3\rangle$ , and (d)  $k = 2\pi - 2.5, |\pi/6, 4\pi/3\rangle$ .

between experiment and simulation data increased with increasing  $k$ , implying the sensitivity of the system dynamics to initial conditions and experimental imperfections. This observation highlighted the notion that quantum chaos could pose a hurdle in quantum information processing tasks, whose detrimental effects might have to be mitigated [88].

## 2.6 Summary and outlook

In summary, we experimentally investigated the quantum signatures of chaos in a two-qubit NMR system using kicked top model. We could characterize the dynamics in two distinct ways:

(i) We studied the correspondence between classical phase space and quantum dynamics using order-parameter profiles extracted from the von Neumann entropy of the reduced system. These profiles could capture good correspondence with classical phase space features for low chaoticity parameter values. Additionally, they could also capture the inherent periodicity and symmetry in the quantum dynamics for larger chaoticity parameters, a feature absent in the classical equivalent. The order-parameter could pick up clear distinguishing features despite the quantum state purity of the NMR system being well below the threshold for entanglement.

(ii) We also studied the localization and delocalization of the reduced quantum state on the Bloch

sphere using the Husimi probability distribution function. We observed the localization of the profiles for low chaoticity conditions and significant delocalization otherwise. The Husimi distribution profiles also showed temporal periodicity that is characteristic of the quantum system. Moreover, the study emphasised the sensitivity of the distribution to experimental imperfections, particularly at higher values of the chaoticity parameter.

It is interesting to note that the system considered here, comprising only two-qubits, is in the deep quantum regime, but still exhibits the marks of quantum chaos. Further investigation of other quantum correlation measures such as discord, negativity, etc. under more varied parameter regimes will help better understand the bridge between chaos in quantum and classical systems. Another topic that is currently gaining significant momentum is the study of out-of-time-order-correlations (OTOC) in the Heisenberg model and its relation to quantum chaos and the quantum equivalent of Lyapunov exponent. These can be systematically studied in spin systems of varying sizes to understand and characterize quantum chaos.

In the next chapter, we use the kicked top model to study quantum chaos in large star-topology spin registers.

## CHAPTER 3

---

### Quantum chaos in large spin-registers

---

#### Abstract

In this chapter, we numerically study chaos in a star-topology system using the quantum kicked top model. Star-topology registers consist of a central spin uniformly coupled to identical and indistinguishable satellite spins. We numerically study the behaviour of different sizes of star-topology registers when evolved under varying degrees of chaos. We initialize the systems to a definite region in the phase space and use entanglement entropy to characterize its dynamics when evolved under the kicked top model. These large spin registers being much larger systems, are closer to the classical limit and help understand the quantum-classical bridge of chaos.

#### Reported in

T S Mahesh, Deepak Khurana, **V. R. Krithika**, G J Sreejith and C S Sudheer Kumar, *Star-topology registers: NMR and quantum information perspectives*, [J. Phys.: Condensed Matter 33 383002 \(2021\)](#).

### 3.1 Introduction

Quantum chaos manifests in interacting spin systems and it is important to understand the fundamental aspects of the phenomenon for developing robust quantum technology, where such interactions might be detrimental. In the previous chapter, we studied quantum chaos in a two-qubit system. A natural extension would be the study of large spin systems, which are closer to the classical limit, thus bridging the quantum and classical domains. Star topology systems are convenient candidates for such studies.

### 3.1.1 Objectives

In this work, we numerically study quantum chaos in star-topology spin registers. We begin with a brief description of star systems and their Hamiltonian. Following this, we investigate -

- (i) how star systems can be used to simulate the dynamics of quantum kicked top (QKT) with disorder using NMR spin registers
- (ii) the behaviour of star systems of different sizes evolving under QKT dynamics with varying degrees of chaos via entanglement entropy.

### 3.1.2 Star topology registers

Star topology registers (STR), as shown in Fig. 3.1, are systems with a central spin coupled uniformly to many surrounding identical and indistinguishable satellite spins, with no effective couplings between the satellite spins. In liquid state NMR, such samples allow control over the central spin and the satellite spins collectively. These systems also possess a high degree of symmetry since the system remains invariant under exchange of satellite spins. Such geometry and interaction configuration is advantageous for the generation of highly entangled and correlated states. Some such states have been shown to be highly useful for sensing applications [159, 160], microscopy and imaging [161, 162], diffusion studies [54], algorithmic cooling [163], quantum Fisher information amplification [164], time crystal studies [165], quantum batteries [166], and quantum state tomography [167] to name a few.

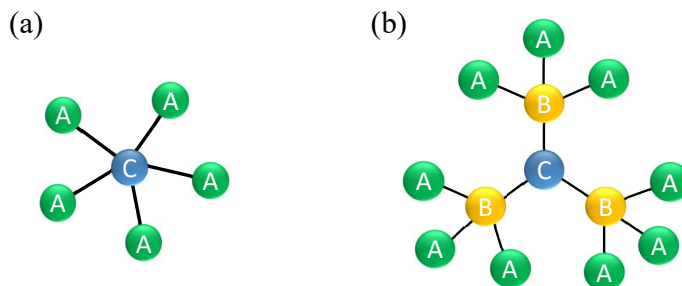


**Figure 3.1:** Schematic of (a) star topology (b) hierarchical star topology systems

A general star topology liquid state NMR system with central spin ( $C$ ) and  $N - 1$  satellite

spins ( $A$ ) has a Hamiltonian of the form

$$H = \omega_C I_z^C + \omega_A \sum_{i=1}^{N-1} I_{zi}^A + 2\pi \mathcal{J}_{CA} I_z^C \sum_{i=1}^{N-1} I_{zi}^A, \quad (3.1)$$

where  $\omega_C = -\gamma_C B_0$  and  $\omega_A = -\gamma_A B_0$  are the Larmor frequencies of central and satellite spins respectively, and  $\mathcal{J}_{CA}$  is the strength of scalar  $\mathcal{J}$ -coupling between them. The eigenstates of this Hamiltonian are product states of individual qubits in Zeeman basis (computational basis)  $\{|0\rangle, |1\rangle\}$ . Single-qubit gates can be realized on the central spin, while only collective rotations can be implemented in the satellite spins due to lack of individual addressability. This enables creation of NOON states which are of the form

$$|\psi\rangle = \frac{|0\rangle_C \otimes |0_1 0_2 \dots 0_{N-1}\rangle_A + |1\rangle_C \otimes |1_1 1_2 \dots 1_{N-1}\rangle_A}{\sqrt{2}} \equiv \frac{|N, 0\rangle + |0, N\rangle}{\sqrt{2}}, \quad (3.2)$$

where the notation  $|N, 0\rangle$  is representative of  $N$  spins in state  $|0\rangle$  and zero spins in  $|1\rangle$ , while  $|0, N\rangle$  implies the vice-versa, which gives these states their signature name. For a three-spin system, with one central qubit and two satellite qubits, this is nothing but the  $GHZ$  state  $|\psi_{GHZ}\rangle = \frac{|000\rangle + |111\rangle}{\sqrt{2}}$ . These states can be prepared in systems with any geometry, but it is easier in star systems due to collective control over satellite spins. Starting from the pure ground state  $|\psi\rangle = |0\rangle_C \otimes |0_1 0_2 \dots 0_{N-1}\rangle_A$ , applying a Hadamard gate ( $U_{\text{had}}$ ) on the central spin followed by CNOT ( $C_C NOT_A$  with control on  $C$  and target on  $A$ ) on the satellite spins gives

$$\begin{aligned} |0\rangle_C \otimes |0_1 0_2 \dots 0_{N-1}\rangle_A &\xrightarrow{U_{\text{had}}^C} \frac{|0\rangle + |1\rangle}{\sqrt{2}} \otimes |0_1 0_2 \dots 0_{N-1}\rangle_A \\ &\xrightarrow{C_C NOT_A} \frac{1}{\sqrt{2}} |0\rangle_C \otimes |0_1 0_2 \dots 0_{N-1}\rangle_A + \frac{1}{\sqrt{2}} |1\rangle_C \otimes |1_1 1_2 \dots 1_{N-1}\rangle_A, \end{aligned} \quad (3.3)$$

which is the  $NOON$  state. The same protocol applied to thermal equilibrium state with Boltzmann population distribution gives a mixed state with combination of different coherence order states  $|\psi\rangle = |M, S\rangle + |S, M\rangle$  where  $|M, S\rangle$  implies  $M$  spins in state  $|0\rangle$  and  $S$  spins in state  $|1\rangle$  and  $|S, M\rangle$  implies the vice-versa. Depending on the exact values of  $M, S$ , the states have different coherence orders. Consider the previously mentioned three-qubit example. For  $M = 3, S = 0$ , this gives the  $NOON$  state (also  $GHZ$  state in this case). For  $M = 2, S = 1$ , we get states of the form  $\frac{|001\rangle + |110\rangle}{\sqrt{2}}$  and their permutation in satellite spins, i.e.,  $\frac{|010\rangle + |101\rangle}{\sqrt{2}}$ . The *coherence or-*

der ( $m_q$ ) of a state can be estimated from the net of eigenvalues of  $|M, S\rangle$  and  $|S, M\rangle$ , taking  $m_s(|0\rangle) = 1/2$ ,  $m_s(|1\rangle) = -1/2$ , as

$$m_s(|M, S\rangle) = M/2 - S/2, \quad m_s(|S, M\rangle) = S/2 - M/2, \quad m_q = m_s(|M, S\rangle) - m_s(|S, M\rangle).$$

A state with desired coherence order can be filtered from the mixture of all coherence orders using a pair of pulsed field gradients [54, 56]. Though such states can be prepared in systems with other topologies, it is easier in star-systems due to the high symmetry and collective addressability of satellite spins. They have been shown to be good candidates for studying out-of-time-order correlation function behaviours [55], spreading of correlations [168], etc. Here, we use star-systems to numerically study quantum chaos using the kicked top model. Since these are large spin registers, they are closer to the classical limit, and are ideal systems to understand the bridge between classical and quantum chaos.

## 3.2 Quantum chaos in star topology systems

In this work, the kicked top model (introduced in the previous chapter) is extended to the star topology systems. The Hamiltonian of a single kicked top for a spin- $j$  system is given by

$$H_{\text{QKT}} = pJ_x \sum_n \delta(t - n\tau) + \frac{k}{2j\tau} J_z^2, \quad (3.4)$$

where  $J_\alpha = \sum_i I_{\alpha i}$ ,  $\alpha = x, y, z$  are the net spin angular momentum components with  $I_{\alpha i}$ , denoting the spin operators of constituent qubits.

The Hamiltonian of a star-system with RF pulse of duration  $\Delta_\alpha$  for  $\alpha \in C, A$  on both the central and satellite spins is given by

$$H = \frac{\pi}{2\Delta_C} I_x^C + \frac{\pi}{2\Delta_A} \left( \sum_i I_{xi}^A \right) + 2\pi \mathcal{J}_{CA} I_z^C \sum_i I_{zi}^A, \quad (3.5)$$

such that  $\pi/2\Delta_C = p = \pi/2\Delta_A$ . We can see that Eq. 3.5 can be mapped to Eq. 3.4 using  $J_x \equiv I_x^C + \sum_i I_{xi}^A$ , and  $\frac{k}{2j} J_z^2 \equiv 2\pi \mathcal{J}_{CA} I_z^C \sum_i I_{zi}^A$  and setting  $p = \pi/2$ . An important point to note here is that  $J_z^2$  would necessitate couplings between all spins in the system, i.e.,  $\mathcal{J}_{CA} I_z^C \sum_i I_{zi}^A$

and  $\mathcal{J}_{i,j} I_{z_i}^A I_{z_j}^A$ . However, in a star-system, all-to-all coupling is absent and only the centre-satellite interaction term is present as described in the previous section. Hence, in liquid-state NMR, a star-system can be used to simulate a *kicked top with disorder* where, since some couplings are absent, we get a set two-qubit kicked-tops with  $j = 1$ , each of which is constituted by an ancillary qubit and the common central qubit. Moreover, such a model does not have a well-defined equivalent in the classical limit. It hence provides an almost exclusive study of chaotic behaviour in quantum systems with coupling configurations as present in STR. Different values of chaoticity parameter  $k$  can be realized by changing evolution time  $\tau$  under the scalar  $\mathcal{J}$ -coupling term since  $k = 2\pi\mathcal{J}_{CA}\tau$ . In the following numerical analysis, we thus set  $j = 1$ , and simulate the dynamics of a star-topology system with varying number of satellite spins for different values of  $k$ .

### 3.2.1 Results and discussion

We use entanglement entropy as a measure for diagnosing quantum chaos, as done in the previous chapter. Fig. 3.2(a)-(d) shows the von Neuman entropy of an STR of size  $N = 10$  with  $\mathcal{J}_{CA} = 50$  Hz and varying chaoticity parameter  $k$ . In each case, the STR qubits were initialized to the phase-space point  $(\theta, \phi)$  in the Bloch sphere, followed by the evolution under the Hamiltonian in equation Eq. 3.5. We can see that for  $k = 0$  (Fig. 3.2(a)), the entropy is identically  $\approx 0$  over the entire phase space, and as the chaoticity parameter increases, the average von Neumann entropy of the system increases as well (Fig. 3.2(b)-(d)). Moreover, for smaller  $k$  values, the phase space shows distinct islands of low entropy surrounded by high entropy regions. Such distributions can be interpreted as a quantum equivalent of regular and chaotic regions of the classical phase space. Furthermore, to study the role of STR size in the dynamics of the system, we initialized the system to a fixed point in the phase space  $(\theta, \phi) = (\pi/2, \pi/2)$  and evolved the system for 200 kicks while varying the number of ancillas from 1 to 9. The von Neumann entropy of the central spin averaged over the last hundred kicks is shown in figures Fig. 3.2(e)-(f). Interestingly, we can see that the dynamics shows oscillatory behavior for both odd and even number of ancillas. For small systems, we can expect such oscillations due to the small dimension of the Hilbert space. However, the system with any even number of ancillas shows more prominent oscillations, compared to odd number of ancillas, in the von Neumann entropy

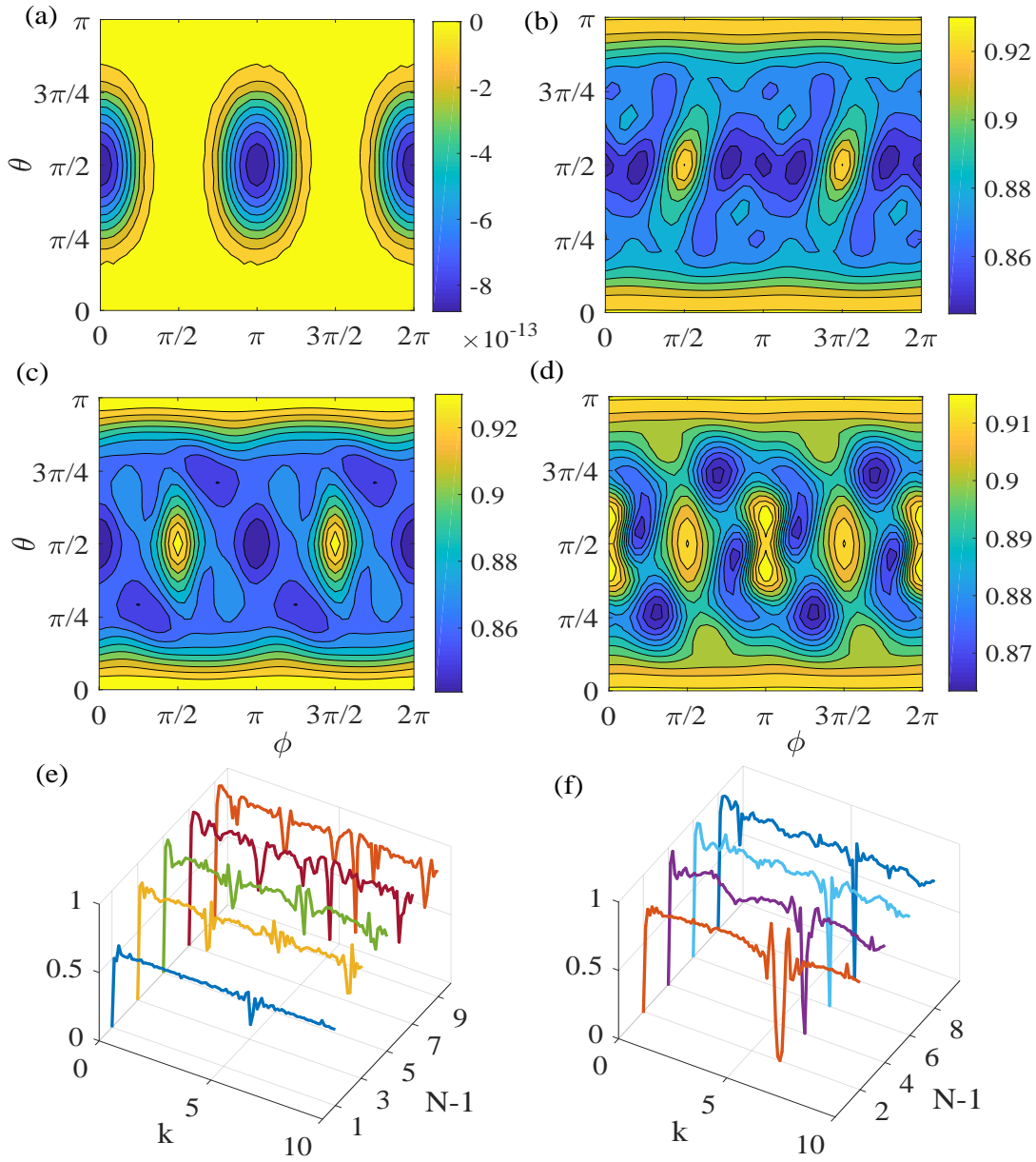


**Figure 3.2:** Quantum chaos in an STR. von Neumann entropy of the central qubit for (a)  $k = 0$ , (b)  $k = 2$ , (c)  $k = 5$ , and (d)  $k = 10$ . Entropy as a function of STR size for (e) odd and (f) even number of ancillary qubits for the fixed initial state  $(\theta, \phi) = (\pi/2, \pi/2)$ . In all the cases  $\mathcal{J}_{CA} = 50$  Hz and the entropy is averaged over the last 100 out of a total of 200 kicks.

of the central spin for large values of  $k$ . Such a characteristic can be attributed to symmetries in the system in the different cases considered. Moreover, these results also indicate that the role of multiple-quantum coherences, which is fundamentally linked to the size of the system. The interplay between multiple quantum coherences and chaos is yet to be probed and is crucial for understanding chaos in such systems.

### 3.3 Conclusions and outlook

Star-topology registers are large spin systems with ease of coherent control for studying various quantum information processing tasks. They are ideal candidates for producing highly entangled and correlated states which have proven to be extremely useful for versatile applications, mainly quantum sensing and metrology. Here, we have numerically studied quantum chaos in STR using the kicked top model for different values of chaoticity parameter  $k$ . However in STR due to absence of all-to-all couplings, these systems can be understood to simulate a kicked top with disorder. Using time averaged entanglement entropy as a witness for quantum chaos, we observed islands of low-entropy regions separated by sea of high entropy regions, much like the entropy patterns for a well defined two-qubit kicked top model. Furthermore, we studied the dynamics of the system as a function of size of STR when initialized to a fixed region in the phase space corresponding to  $(\theta, \phi) = (\pi/2, \pi/2)$ . We observed oscillations in the time averaged entropy for STR with both odd and even number of satellite spins, with system with even number of ancillary spins showing more prominent oscillations. These features can be ascribed to the symmetries in system for odd and even number of satellite spins. The dynamics of such a system are intimately linked to the generation and spreading of correlations within the system with time evolution. Studies to probe the relation between different orders of coherences and quantum chaos will be very fruitful not just for building the foundations of quantum chaos, but will also contribute to deeper understanding of Floquet systems, open system dynamics, and for applications including quantum information processing and computing tasks.

## CHAPTER 4

---

### Dynamical tunneling in nuclear spins

---

#### Abstract

In chaotic Hamiltonian systems, dynamical tunneling refers to quantum tunneling between states whose classical limit correspond to symmetry-related regular regions separated by a chaotic zone. In usual quantum tunneling, a low-energy quantum particle penetrates across a physical barrier of higher potential energy, by traversing a classically forbidden region, and finally escapes into another region. In a similar scenario, a classical particle inside a closed regular region is dynamically bound from escaping to other regions of the phase space, whereas tunneling in the quantum regime permits escape through dynamical barrier. In this chapter, we report an experimental realization of dynamical tunneling in spin systems using nuclear magnetic resonance (NMR) architecture. In particular, dynamical tunneling in quantum kicked tops of spin-1 and spin-3/2 systems using two- and three-qubit NMR registers is investigated. By extracting time-dependent expectation values of the angular momentum operator components, size-dependent tunneling behaviour for various initial states is systematically investigated. Further, by monitoring the adverse effects of dephasing noise on the tunneling oscillations, we assert the importance of quantum coherence in enabling dynamical tunneling.

#### Reported in

**V. R. Krithika**, M. S. Santhanam and T. S. Mahesh, *NMR Investigations of Dynamical Tunneling in Nuclear Spin Systems*, [arXiv:2212.12350](https://arxiv.org/abs/2212.12350) (2022).

## 4.1 Introduction

In this chapter, we study another facet of dynamics that arises from a quantum kicked top, namely dynamical tunneling. Quantum tunneling usually refers to the phenomenon by which a wave packet penetrates and transits through a physical potential barrier despite having lesser energy than the barrier height [169]. Classically, this is a forbidden process, though it is allowed in a quantum system. The quantum tunneling phenomenon has been studied extensively and has found applications in various fields ranging from nuclear physics, superconductivity, and electronics to microscopy [169–176].

In chaotic Hamiltonian systems, quantum tunneling manifests into a much richer and more complex phenomenon due to the complexity of underlying classical dynamics [73, 177]. Interestingly, it was realized that the quantum tunneling phenomenon can be extended to scenarios even without any physical barrier. In such cases, the potential barriers are replaced by dynamical barriers formed by invariant phase space structures in the classical limit. Hence, this is often called dynamical tunneling and was first studied by Davis and Heller [178, 179] in a two-dimensional nonlinear system. Dynamical tunneling happens when a wave packet tunnels between symmetry-related regular regions such as elliptic islands. It is important to note that the regular regions are separated, not necessarily by potential barriers, but by dynamical constraints. A classical particle initialized in one such regular region can never couple with the other, and hence any transport between these regions is forbidden. In a semiclassical sense, these regular regions would contribute to degenerate eigenstates. However, if tunneling is present between these regular classical regions, we expect the disconnected classical regions to be coupled by quantum dynamics and the degeneracy is lifted. This results in characteristic tunneling doublets in the energy spectrum. The corresponding eigenstates are symmetric and anti-symmetric linear combinations of wavefunctions that predominantly localize on these regular regions [73, 175, 178, 180, 181]. This can be effectively modelled as a two-state process (a two-level system) involving these nearly-degenerate states. It was found that the tunneling rate between the regular regions can be further enhanced if these regions are separated by a sea of chaos [73]. In this case, the tunneling wave function has an overlap also with the chaotic region, which aids the tunneling process. In this case dynamical tunneling, termed as chaos-assisted tunneling, can be thought of as a process involving

three levels – the two nearly-degenerate states coupled through an intermediate chaotic state. The chaotic state can be modelled as a typical state drawn from an appropriate random matrix ensemble. It must also be pointed out that a similar mediation by the classical nonlinear resonances, called the resonance assisted tunneling, in near-integrable regime also leads to enhanced tunneling rates between low and high excited states lying within the same nonlinear resonance region [182–188]. The rate of tunneling in integrable systems comparatively is much slower due to the absence of resonances and chaos. It is evident that quantum tunneling behaviour can be strongly influenced by the underlying classical structures arising from integrability and non-integrability of the systems [177, 181].

Though dynamical tunneling has been theoretically explored for the last three decades, experimental demonstrations are far fewer [73, 75, 76, 189–195]. They are limited to essentially two chaotic test-beds, namely, a driven cold atomic cloud [75, 76, 191] and microwave annular billiards [189, 192]. Despite the popularity of kicked models within the fold of quantum chaos, especially the ones based on spins such as the kicked top model [151], only one experimental demonstration until now has employed kicked systems [78]. A theoretical study of dynamical tunneling in quantum kicked top (QKT) had been reported in Refs. [196] and [148]. Ref. [196] showed that in the presence of dynamical tunneling between regular regions, the expectation values of angular momentum operator components display periodic revivals. To our knowledge, this feature has not been explicitly shown through experiments so far. Here we study this feature in spin-1 and spin-3/2 systems.

### 4.1.1 Objectives

In this work, we carry out NMR investigation of dynamical tunneling in a QKT model formulated as a collection of periodically kicked and interacting spins. By monitoring the expectation values of the angular momentum operators of the QKT, we performed a systematic experimental investigations into

- (i) dynamical tunneling in spin systems for different initial states
- (ii) system size dependence of tunneling period with two different system sizes, and
- (iii) effect of dephasing noise on the robustness of tunneling.

This model is useful because the approach to classical limit can be attained by expanding the

Hilbert space, by either increasing the number of spins, or the spin number, or both. Hence, this system provides a convenient route to study dynamical tunneling and pushing it towards the classical limit.

## 4.2 Dynamical tunneling in spin systems

### 4.2.1 Quantum Kicked Top (QKT) model

As explained in Chapter 2, the QKT model of a spin- $j$  system is described by the Hamiltonian (with  $\hbar$  set to unity) [151, 196]

$$H_{\text{qkt}} = \begin{cases} H_{\text{kick}} = \frac{\pi}{2\Delta} J_y, & \text{for } t \in [n\tau - \frac{\Delta}{2}, n\tau + \frac{\Delta}{2}] \\ H_{\text{nl}} = \frac{k}{2j\tau} J_z^2, & \text{otherwise.} \end{cases} \quad (4.1)$$

Here  $J_\alpha$  with  $\alpha = x, y, z$  are components of the angular momentum operator, and  $\Delta$  is the kick duration that produces a  $\pi/2$  rotation about the y-axis described by the unitary operator  $U_{\text{kick}} = \exp\{-iH_{\text{kick}}\Delta\}$ . The second term describes the nonlinear evolution governed by the chaoticity parameter  $k$  for a time period  $\tau$  with the corresponding unitary  $U_{\text{nl}} = \exp\{-iH_{\text{nl}}\tau\}$ . The effective Floquet operator can then be written as  $\mathcal{F} = U_{\text{nl}}U_{\text{kick}}$ . The dynamics of the system can be evaluated from the evolution of angular momentum components of the QKT under the Floquet evolution after the  $n$ -th kick as  $J_\alpha(n+1) = \mathcal{F}^\dagger J_\alpha(n)\mathcal{F}$ , for  $\alpha = \{x, y, z\}$ . The classical map can be obtained from the scaled variables  $V = J_\alpha/j$  in the limit  $j \rightarrow \infty$  [151] which leads to the following equations of motion:

$$\begin{aligned} X' &= Z \cos(kX) + Y \sin(kX) \\ Y' &= -Z \sin(kX) + Y \cos(kX) \\ Z' &= -X. \end{aligned} \quad (4.2)$$

Since the total angular momentum of the system is conserved, the dynamics of the system can be parameterized in terms of two parameters  $(\theta, \phi)$  such that  $X = \sin\theta \cos\phi$ ,  $Y = \sin\theta \sin\phi$ ,  $Z = \cos\theta$ . For low values of the chaoticity parameter,  $k \sim 0.5$  the system is highly

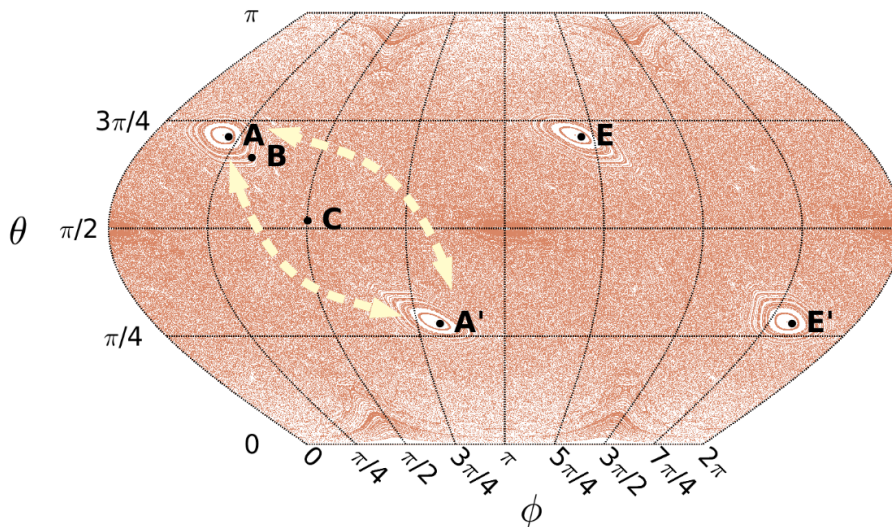
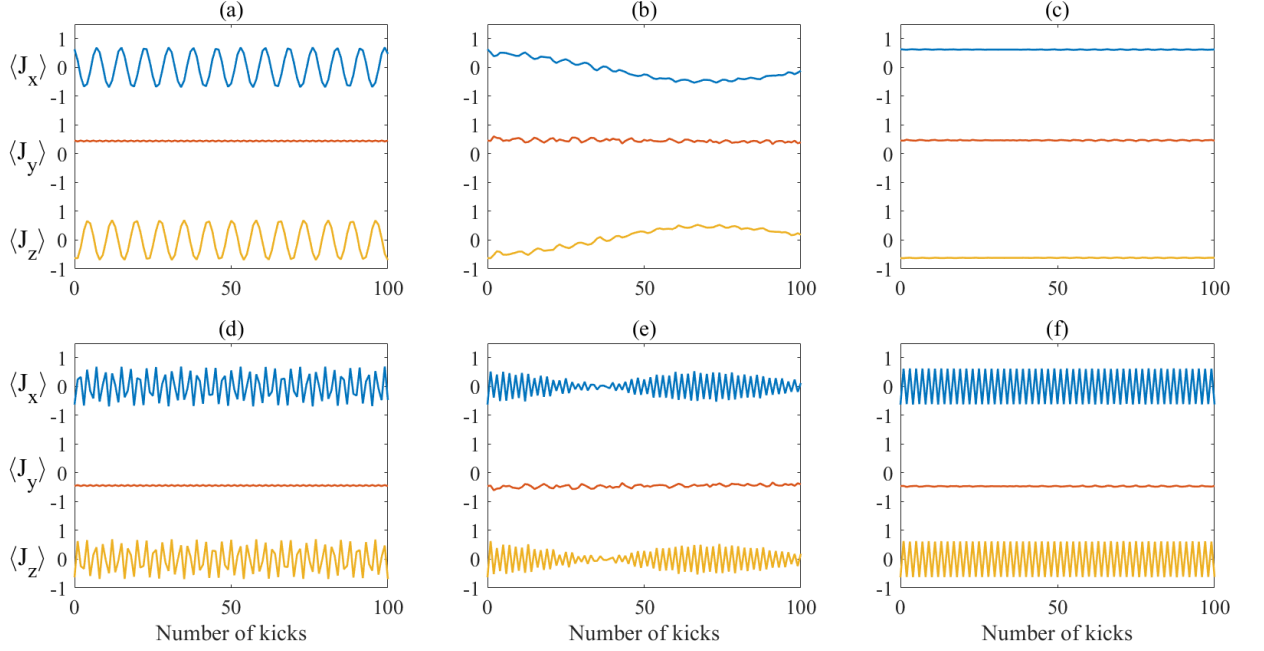


**Figure 4.1:** Classical phase space of the kicked top model for chaoticity parameter  $k = 3$ . The mixed phase space has distinct regular islands separated by a chaotic sea. A classical system initialized in the regular regions, labelled by **A** and **A'**, will continue to remain there throughout the dynamics, while that initialized in the near-regular region, labelled by **B**, can move along its periodic orbit, and that initialized in the chaotic region, labelled by **C**, can explore the phase space. The regions labelled by **E** and **E'** form a period-two orbit and keep jumping from one to the other with every kick. The dynamics of a QKT initialized in the states **A**, **B**, and **C** studied here reveal dynamical tunneling between **A** and **A'** as indicated by the arrows.

regular, but transitions to a mixed phase space as  $k$  is increased before becoming almost completely chaotic at around  $k = 6$  [146]. This map has time reversal symmetry and reflection symmetry about the  $y$ -axis [151]. The classical phase space for  $k = 3$  is shown in Fig. 4.1.

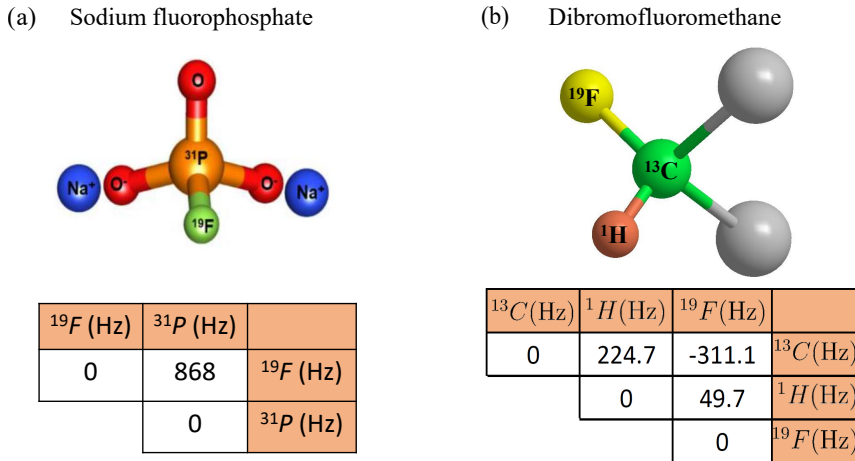
## 4.2.2 Dynamical tunneling in QKT model

Fig. 4.1 displays the stroboscopic map of the classical kicked top with  $k = 3$ . Under classical evolution, even as time  $t \rightarrow \infty$ , the initial conditions indicated by **A** and **A'** in Fig. 4.1 will remain trapped in their respective regular regions. However, if the system is initialized in a chaotic region, indicated by **C** in Fig. 4.1, it can then explore the entire connected chaotic layer of the phase space. In contrast, a QKT initialized in one of the regular regions can defy the classical dynamical barrier and periodically tunnel to and from the other regular region of appropriate symmetry [180]. The periodic tunneling behaviour of such a system was studied earlier using the expectation values  $\langle J_\alpha \rangle$  of the angular momentum operator [196]. Interestingly, a QKT initialized in a chaotic region does not show such clear periodicity.



**Figure 4.2:** Normalized expectation values of angular momentum operator components  $\langle J_\alpha \rangle$  obtained from numerical simulations with  $k = 3$  starting from the states **A** (a-c) and **E** (d-f) for spin sizes  $j = 1$  (a,d),  $j = 10$  (b,e) and  $j = 100$  (c,f). As the spin size increases the system tends towards the classical limit exhibiting prolonged tunneling periods. For the latter initial state (d-f), the oscillations in expectation values  $\langle J_\alpha \rangle$  are maintained for all spin sizes, with the system exhibiting clear period-two oscillations as it tends to the classical limit, which can be seen prominently for  $j = 100$  (f).

We first look into the system size dependence of tunneling behaviour for chaoticity parameter  $k = 3$ . As the system size increases ( $j \rightarrow \infty$ ), the classical limit is approached, and the tunneling behaviour is suppressed. Let us consider the initial state  $\mathbf{A} \equiv |\theta_{\mathbf{A}}, \phi_{\mathbf{A}}\rangle \equiv (2.25, 0.63)$  at the centre of one of the regular regions and its symmetry related state  $\mathbf{A}' \equiv \exp(-i\pi J_y)|\theta_{\mathbf{A}}, \phi_{\mathbf{A}}\rangle \equiv (\pi - 2.25, \pi - 0.63)$  (see Fig. 4.1). The numerical simulations of  $\langle J_\alpha \rangle$  for the QKT model for different spin sizes starting from **A** are shown in Fig. 4.2(a)-(c). It is clear that  $\langle J_x \rangle$  and  $\langle J_z \rangle$  show rapid oscillations for  $j = 1$  (Fig. 4.2(a)) indicating tunneling between **A** and **A'**. However, for a larger system with  $j = 10$  (Fig. 4.2(b)) the period is elongated, and for  $j = 100$  (Fig. 4.2(c)) the system shows no sign of periodicity in the chosen time range. It is interesting to note that the other pair of similar-looking regular regions, labelled by  $\mathbf{E} \equiv |\theta_{\mathbf{E}}, \phi_{\mathbf{E}}\rangle = (2.25, 0.63 + \pi)$  and  $\mathbf{E}' \equiv \exp(-i\pi J_y)|\theta_{\mathbf{E}}, \phi_{\mathbf{E}}\rangle \equiv (\pi - 2.25, 2\pi - 0.63)$ , have a totally different behaviour, as shown in Fig. 4.2(d)-(f). They form a period-two orbit and oscillate between one another with every kick in the classical limit [151]. This is clearly observed for a large spin system, such as  $j = 100$



**Figure 4.3:** Experimental systems used for tunneling experiments. (a) The two-qubit system of sodium fluorophosphate used to simulate a single spin-1 system and (b) three-qubit system of dibromofluoromethane used to simulate a single spin-3/2 system, along with their Hamiltonian parameters shown in the tables below. The diagonal elements indicate chemical shifts, while off-diagonal elements indicate the scalar  $\mathcal{J}$ -coupling constant values.

in Fig. 4.2(f). For smaller spin sizes, such as  $j = 1$  and  $j = 10$  (Fig. 4.2(d,e)), the values of  $\langle J_x \rangle$  and  $\langle J_z \rangle$  show irregular oscillations with beat patterns.

## 4.3 Experimental methodology

### 4.3.1 NMR Hamiltonian

To study the size dependent behaviour of dynamical tunneling, we simulated the QKT in spin-1 and spin-3/2 systems using two- and three-qubit NMR systems respectively. The two-qubit system comprised  $^{19}\text{F}$  and  $^{31}\text{P}$  of sodium fluorophosphate (Fig. 4.3(a)) dissolved in  $\text{D}_2\text{O}$ , and the three-qubit system comprised  $^{13}\text{C}$ ,  $^1\text{H}$  and  $^{19}\text{F}$  spins of dibromofluoromethane (Fig. 4.3(b)) dissolved in deuterated acetone. All the experiments were performed on samples containing about  $10^{15}$  nuclear spins maintained at 300 K on a Bruker 500 MHz high resolution spectrometer with a static magnetic field  $B_0\hat{z}$  with  $B_0 = 11.7$  T. As explained in Chapter 2, by moving to a rotating frame resonant with the Larmor frequencies of the spins, their chemical shifts can be set to zero [49]. The effective NMR Hamiltonian in the weak-coupling limit is then given only by the scalar

$\mathcal{J}_{ij}$  coupling interaction and takes the form

$$H_{\mathcal{J}} = \sum_{i,j>i} 2\pi \mathcal{J}_{ij} I_{zi} I_{zj}. \quad (4.3)$$

The spins can further be manipulated by radio frequency (RF) pulses resonant with the corresponding characteristic Larmor frequencies and described by the Hamiltonian

$$H_{\text{RF}} = \sum_i \frac{\pi}{2\Delta_i} I_{yi}, \quad (4.4)$$

where  $\Delta_i$  is the pulse duration corresponding to the  $i$ -th spin species. Hence the NMR system with the RF pulses is described by the combined Hamiltonian [197]

$$H_{\text{NMR}} = \sum_i \frac{\pi}{2\Delta_i} I_{yi} + \sum_{i,j>i} 2\pi \mathcal{J}_{ij} I_{zi} I_{zj}. \quad (4.5)$$

In systems with three or more qubits, we can realize an uniform evolution under a single effective scalar coupling constant  $\mathcal{J}$  by using the standard spin echo methods [48], such that

$$\begin{aligned} H_{\text{NMR}}^{\text{eff}} &= H_{\text{RF}} + H_{\mathcal{J}}^{\text{eff}} \\ &= \sum_i \frac{\pi}{2\Delta_i} I_{yi} + \mathcal{J} \sum_{i,j>i} 2\pi I_{zi} I_{zj}. \end{aligned} \quad (4.6)$$

Comparing this with Eq. 4.1, we can see that the linear term  $H_{\text{kick}}$  can be mapped to the RF term  $H_{\text{RF}}$ . Since we realize the spin- $j$  QKT using a collection of  $2j$  qubits [91, 146], the nonlinear

term in Eq. 4.1 can be expanded as

$$\begin{aligned}
\frac{k}{2j\tau} J_z^2 &= \frac{k}{2j\tau} \left( \sum_{i=1}^{2j} I_{zi} \right)^2 \\
&= \frac{k}{2j\tau} \left[ \sum_{i=1}^{2j} I_{zi}^2 + 2 \sum_{i=1, j>i}^{2j} I_{zi} I_{zj} \right] \\
&= \frac{k}{2j\tau} \left[ \sum_{i=1}^{2j} \frac{\mathbb{1}}{4} + 2 \sum_{i=1, j>i}^{2j} I_{zi} I_{zj} \right] \\
&\equiv \frac{k}{2j\tau} 2 \sum_{i=1, j>i}^{2j} I_{zi} I_{zj}. \tag{4.7}
\end{aligned}$$

Thus, the nonlinear term can be mapped to the scalar  $\mathcal{J}$  coupling term  $H_{\mathcal{J}}^{\text{eff}}$  up to the identity term which only introduces an unobservable global phase. Moreover, comparing Eq. 4.7 with  $H_{\mathcal{J}}^{\text{eff}}$ , we can see that  $k = 2j\pi\mathcal{J}\tau$ , which enables us to vary the chaoticity parameter  $k$  by tuning the duration  $\tau$  of the effective  $\mathcal{J}$  evolution. Since the duration of the RF pulse  $\Delta_i \ll \tau = k/(2j\pi\mathcal{J})$ , we ignore  $H_{\mathcal{J}}^{\text{eff}}$  during the RF pulse and hence decompose the Floquet evolution  $\mathcal{F}_{\text{NMR}} = U_{\mathcal{J}} U_{\text{RF}}$ , where  $U_{\text{RF}} = \exp(-iH_{\text{RF}}\Delta)$  and  $U_{\mathcal{J}} = \exp(-iH_{\mathcal{J}}^{\text{eff}}\tau)$ .

### Initial state preparation

At ambient temperatures, the thermal energy  $k_B T$  of the NMR spin system is much larger than the Zeeman energy splitting  $\hbar\gamma_i B_0$ . Hence, an  $n$ -qubit system is in a highly mixed state and is given by the Boltzmann distribution [49]

$$\rho_{\text{eq}} \simeq \frac{\mathbb{1}}{2^n} + \sum_i \epsilon_i I_{zi}, \tag{4.8}$$

where  $\mathbb{1}/2^n$  captures the uniform population background, and the purity factor  $\epsilon_i = \hbar\gamma_i B_0 / (2^n k_B T) \sim 10^{-5}$  captures the deviation from uniform population distribution.

To simulate the dynamics of a QKT, it is conventional to initialize the system into coherent states as these are closest to a classical state [152, 153]. We simulate a spin- $j$  QKT using  $2j$  qubits initialized in the spin coherent state defined as

$$|\theta, \phi\rangle = U_{\theta\phi} |0\rangle^{\otimes n}, \text{ where } U_{\theta\phi} = e^{-i\phi \sum_i I_{zi}} e^{-i\theta \sum_i I_{yi}}. \tag{4.9}$$

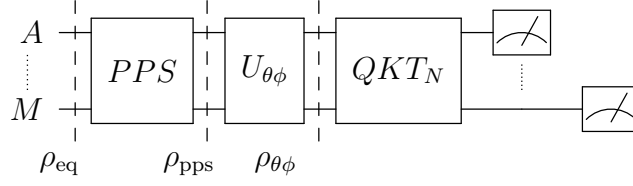


**Figure 4.4:** An experimental circuit to realize the QKT model in a system of  $M$ -qubits. Starting from the state  $\rho_{\text{eq}}$  in thermal equilibrium, a pseudopure state  $\rho_{\text{pps}}$  is prepared. This is followed by preparation of initial state  $\rho_{\theta\phi}$ . We then implement the QKT model for  $N$  kicks and finally readout each qubit.

To realize this in a multi-qubit NMR spin system, we first transform the thermal equilibrium state  $\rho_{\text{eq}}$  to a pseudo-pure state of the form  $\rho_{\text{pps}} = (1 - \epsilon)\mathbb{1}/2^n + \epsilon|\psi\rangle\langle\psi|$  whose dynamics can be mapped isomorphically to the dynamics of a pure state  $|\psi\rangle$  [6, 7]. The detailed NMR pulse sequences for preparing PPS of the two- and three-qubit spin systems considered here are given in Fig. 1.5. These states can then further be transformed into coherent states  $|\theta, \phi\rangle$  for an  $n$ -qubit system

$$\rho_{\theta\phi} = U_{\theta\phi}\rho_{\text{pps}}U_{\theta\phi}^\dagger \equiv |\theta, \phi\rangle\langle\theta, \phi|. \quad (4.10)$$

The system is thus initialized to a required  $(\theta, \phi)$  coordinate in the phase space and the QKT Floquet operator  $\mathcal{F}_{\text{NMR}}$  is subsequently applied  $N$  times to study the time evolution. An experimental circuit, showing the line-up of successive operations for simulating a QKT is displayed in Fig. 4.4.

### Measurement of $\langle J_\alpha \rangle$

In an NMR system, the direct signal measurement by quadrature detection gives  $\langle I_{xi} \rangle + i\langle I_{yi} \rangle$  [49]. To extract  $\langle I_{zi} \rangle$ , we apply the following in succession: (i) a pulsed field gradient (PFG) which destroys the  $x$  and  $y$  magnetization components of the system and following this, (ii) a  $(\pi/2)$  pulse about the  $y$ -axis to rotate the  $z$ -component of magnetization to the  $x$ -axis, and then detect the transverse magnetization. Note that measurement of the angular momentum components of individual spins suffices to estimate the total expectation values  $\langle J_\alpha \rangle$ . The general state  $\rho$  of the

multi-qubit system can be expanded in the product operator basis of constituent spins as

$$\rho = \frac{\mathbb{1}}{2^n} + \sum_i c_{\alpha i} I_{\alpha i} + \sum_{ij\alpha\beta} c_{\alpha\beta ij} I_{\alpha i} I_{\beta j} + \dots, \quad (4.11)$$

where higher order spin correlation terms are not shown. The total expectation value  $\langle J_\alpha \rangle$  for the linear term can then be estimated as

$$\langle J_\alpha \rangle = \text{Tr} \left[ \rho \sum_i I_{\alpha i} \right] = \sum_i c_{\alpha i} I_{\alpha i} = \sum_i \text{Tr} [\rho_i I_{\alpha i}], \quad (4.12)$$

where  $\rho_i = \frac{\mathbb{1}}{2} + \sum_i c_{\alpha i} I_{\alpha i}$  are the reduced density matrices of the constituent spin systems. In the following, we discuss the results of the above mentioned protocols for studying dynamical tunneling in two- and three-qubit spin systems.

## 4.4 Experimental Results

### 4.4.1 $k = 0$ experiments

As a control, we first studied the behaviour of the system in the absence of chaos, *i.e.*,  $k = 0$ . In this case, the system just evolves under  $(\pi/2)$  kicks applied about the  $y$ -axis. The classical equations of motion (Eq. 4.2) at  $(N + 1)$ -th kick relate to the  $N$ -th kick as follows :

$$\begin{aligned} X(N + 1) &= Z(N) \\ Y(N + 1) &= Y(N) \\ Z(N + 1) &= -X(N). \end{aligned} \quad (4.13)$$

The  $y$ -component of the system remains invariant under evolution, while the  $x$  and  $z$  components evolve with each kick. The evolution is thus restricted to circles in the  $xz$  plane for any given initial state. The results of this control experiment are displayed in Fig. 4.5 for the system initialized in to the phase space region characterized by  $|\theta, \phi\rangle = (2.25, 0.63)$ .

The experimental data shows a decay in the amplitude of the oscillation due to accumulation of pulse errors with each kick. We can see that both the two- and three-qubit systems have oscil-

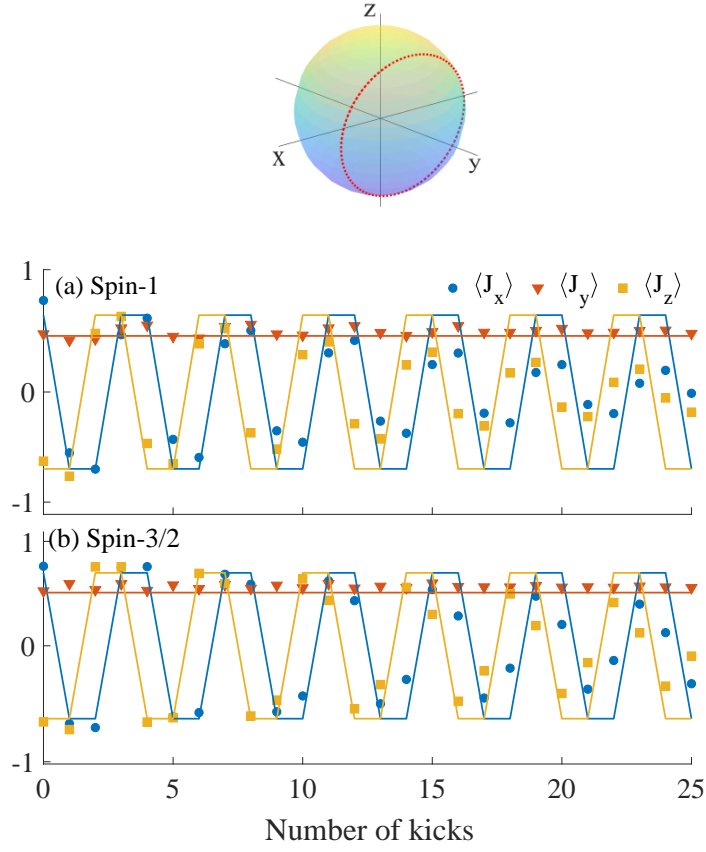


**Figure 4.5:** Control experiments with  $k = 0$  for the two- and three-qubit systems. (a) Denotes the classical trajectory for different initial states. (b) Shows the data from two- and three-qubit systems respectively. The symbols indicate experimental data, while dashed lines indicate simulations. We can see that the experimental data is in good agreement with simulated data. The decay in experimental data points is due to relaxation in the systems.

lating  $J_x, J_z$  values, while the value of  $J_y$  remains constant. Moreover, the period of oscillation is same in both cases. To understand the frequency of oscillations better, we computed the Fourier transform of the time evolution of the system. The frequency domain analysis of the evolution (displayed in Fig. 4.6(a)) shows that the period of oscillation, as anticipated, is independent of the system size.

#### 4.4.2 Tunneling in mixed phase space ( $k = 3$ )

As explained above, we initialize the two- and three-qubit based QKT systems to different regions of the mixed phase space at  $k = 3$ , and study the tunneling behaviour via  $\langle J_\alpha \rangle$  for  $\alpha \in [x, y, z]$ . Following Sanders and Milburn's work (Ref. [196]) we chose the initial state **A** (see Fig. 4.1) in the regular region of phase space, while the initial state **B** lies in the border between regular

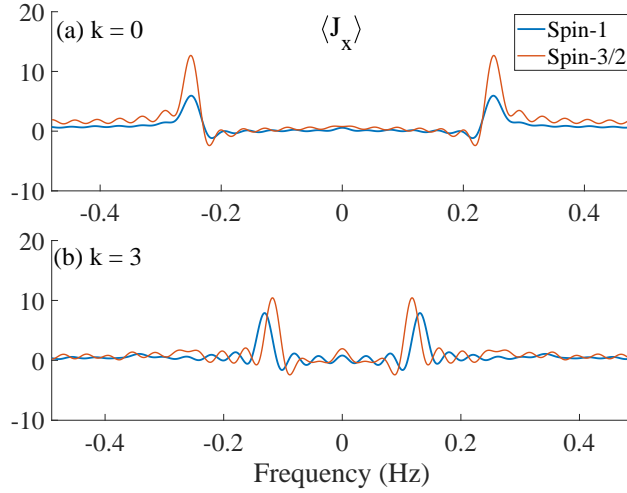


**Figure 4.6:** Fourier transform of (a) control experiments (b) tunneling experiments for spin-1 and spin-3/2 systems. We can see that in the case of control experiments, the frequency of oscillation is same for both the systems. In the case of tunneling experiments, there is a clear shift in the frequency of the three-qubit system as compared to the two-qubit system. This is in accordance with the expectation that as system size increases the tunneling effect should get suppressed.

region and chaotic sea. The initial state  $\mathbf{C}$  lies entirely in the chaotic sea. The system was evolved for  $N = 25$  kicks and  $\langle J_\alpha \rangle$  was measured after each kick. Note that a classical system initialized in state  $\mathbf{A}$  in the regular region is dynamically bound and cannot escape to other regions, such as the state  $\mathbf{A}'$ .

When working with such small quantum systems, the spreading of wavefunctions (outside the phase space region of interest) might be significant and hence needs to be monitored to ensure that tunneling we observe is not due to leakage of probability density. To quantify the overlap of the the time-evolving state with the initial coherent state in regular region  $\mathbf{A}$  and the symmetry-related tunneling region  $\mathbf{A}'$ , we study the trace fidelity defined as [156]

$$F_{\mathbf{S}}(t) = \frac{\text{tr}(\rho(t)\rho_{\mathbf{S}})}{\sqrt{\text{tr}(\rho(t)^2)\text{tr}(\rho_{\mathbf{S}}^2)}}, \quad (4.14)$$

where  $\rho(t)$  is the traceless deviation density matrix of the instantaneous state of the system at time  $t$ ,  $\rho_S$  for  $S \in \{\mathbf{A}, \mathbf{A}'\}$  are the deviation density matrices of coherent states  $\mathbf{A}$  and  $\mathbf{A}'$ . The experimentally measured (symbols) and theoretically estimated (dotted lines) trace fidelity of systems evolving under QKT dynamics with initial state  $\mathbf{A}$  are shown in Fig. 4.7 for spin-1 (a) and spin-3/2 (b) systems respectively. Note that the trace fidelity can take negative values since

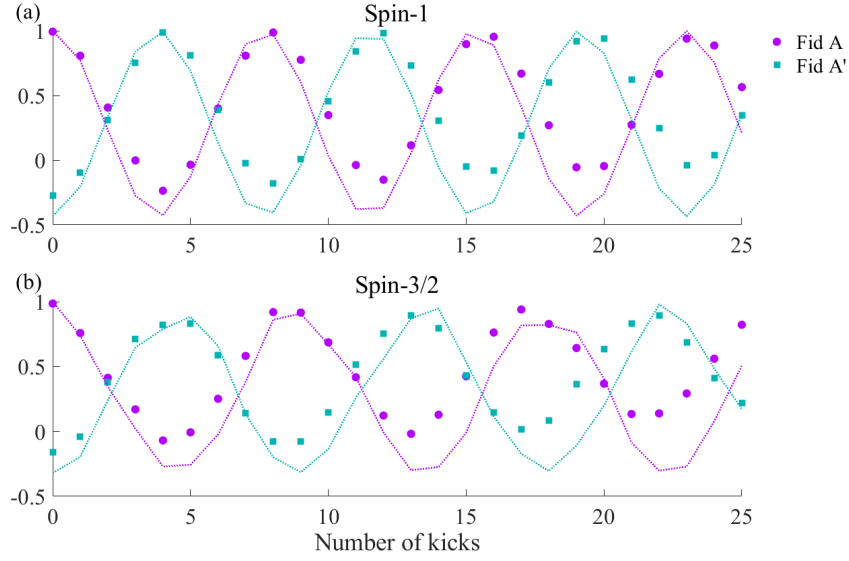


**Figure 4.7:** Trace fidelity of the instantaneous state of the system initialized in the regular region **A** for spin-1 (a) and spin-3/2 (b) systems with respect to the tunneling regions **A** and **A'**. Experimentally extracted values of fidelity are indicated by symbols overlaid on simulated values indicated by dotted lines.

the numerator in Eq. 4.14 is the product of two traceless matrices. Exact overlap is quantified by  $F_S(t) = 1$ , while orthogonality is quantified by  $F_S(t) = 0$ . Non-zero negative values indicate partial overlap and opposite phases between states. From Fig. 4.7(a-b), it is evident that the initial coherent state has maximum overlap with the regular region **A** and a modest overlap with **A'** in spin-1 and even smaller overlap in spin-3/2. Moreover, as the system evolves under QKT dynamics, it periodically localizes in **A** and **A'** with fidelity  $> 0.94$  in spin-1 system and  $> 0.83$  in spin-3/2 system. Let us now look at the extent of overlap between states localized in regions **A** and **A'**. Fig. 4.8 shows the theoretical trace fidelity computed using Eq. 4.14 of the instantaneous state of a system initialized in **A** and undergoing QKT dynamics for  $k = 3$  for spin-1 (a), spin-5 (b) and spin-20 (c) systems. It is evident that as the system size increases, the degree of overlap of states localized in **A**(**A'**) with **A'**(**A**) decreases. This behaviour also emphasises the importance of chaotic states in dynamical tunneling. As the system size increases, the overlap of a localized state in a regular region (**A**,**A'**) with the surrounding chaotic state decreases, which in turn hampers the tunneling efficiency as is reflected in the prolonged time periods in Fig. 4.8(b,c). The fidelity of a single spin- $j$  system in coherent state **A** with the corresponding state **A'** as a function of spin size is shown in Fig. 4.8(d). It can be seen that to achieve overlap  $< 0.1$  between **A** and **A'**, we need at least spin-5, i.e., ten qubits, while overlap  $< 0.01$  requires at least spin-50 (or hundred qubits),

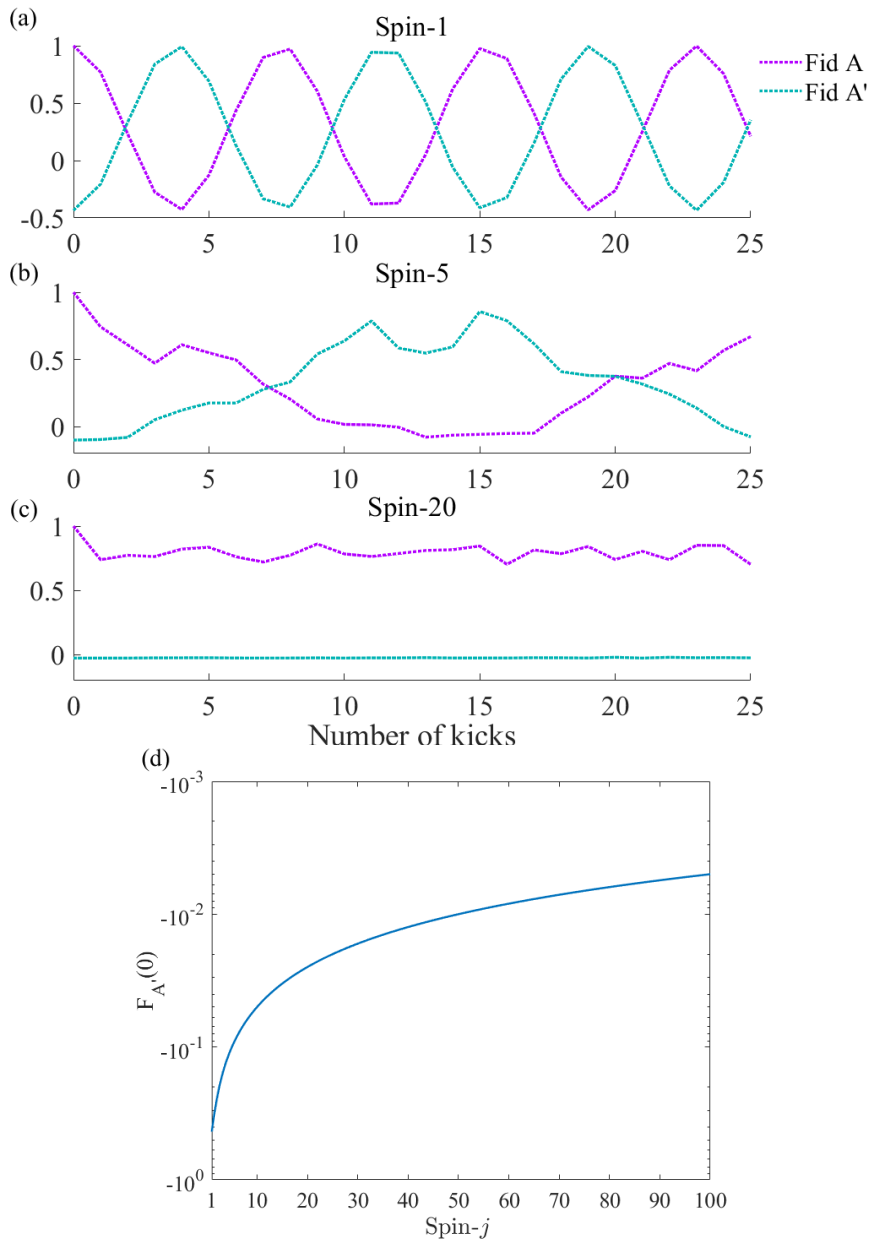


**Figure 4.8:** Trace fidelity of the instantaneous state of QKT with  $k = 3$  initialized in the regular region **A** for spin-1 (a) and spin-5 (b) and spin-20 (c) systems with respect to the tunneling regions **A** and **A'**. Fidelity of coherent state **A** with **A'** as a function of spin- $j$  size (d).

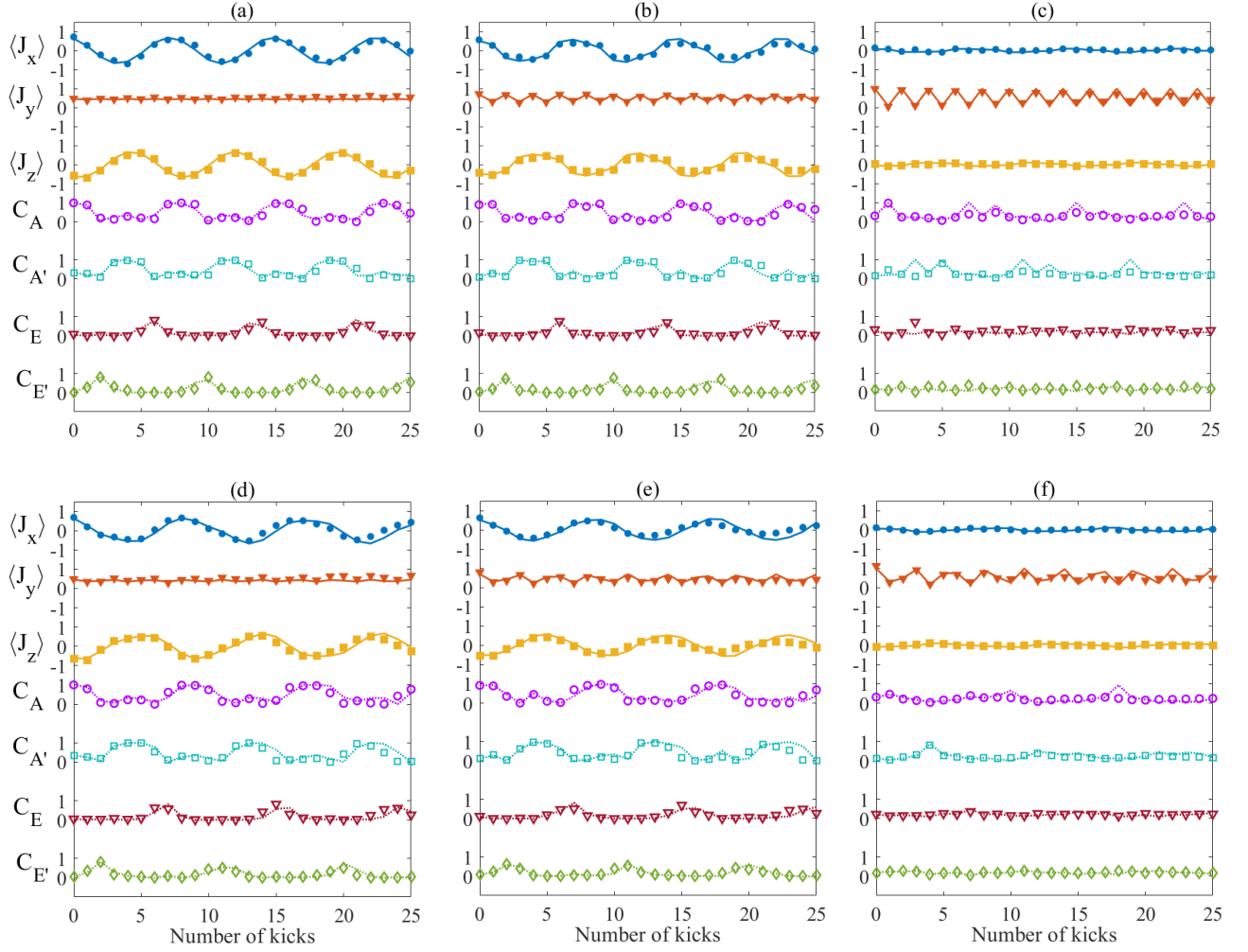


**Figure 4.9:** Dynamics of QKT in two-qubit spin-1 system (a-c) and three-qubit spin-3/2 system (d-f) corresponding to initialization in states **A** (a,d), **B** (b,e), and **C** (c,f). The symbols indicate experimental data while dashed lines indicate simulation. The upper three traces represent  $\langle J_\alpha(t) \rangle$  and the lower four traces represent  $C_S(t)$ . In (a,d) we see that both the systems show clear tunneling patterns for initialization in the regular region with good agreement between simulation and experiments. The revival patterns are observed for the near-regular region as well (b,e), but are not as prominent as those of the regular region. The patterns for chaotic initial state (c,f) show no clear periodicity.

which is beyond the reach of current state of the art quantum simulators.

Fig. 4.9 shows the experimental results (symbols) and numerical simulations (dotted lines) for spin-1 system realized using two-qubits (Fig. 4.9(a-c)) and spin-3/2 system realized using three-qubits (Fig. 4.9(d-f)) initialized in states  $\mathbf{Q} \in \{\mathbf{A}, \mathbf{B}, \mathbf{C}\}$  of the classical phase space shown in Fig. 4.1. In all cases, we set the chaoticity parameter  $k = 3$  and initialized the systems in states  $\mathbf{A}$  (Fig. 4.9(a,d)),  $\mathbf{B}$  (Fig. 4.9(b,e)), and  $\mathbf{C}$  (Fig. 4.9(c,f)). In all the graphs, the top three traces show the expectation values  $\langle J_\alpha^{\mathbf{Q}}(t) \rangle$ . For the initialization into state  $\mathbf{A}$  in the regular region, we observe prominent oscillations in the expectation values of  $J_x$  and  $J_z$ , while that of  $J_y$  remains constant as the system is symmetric about  $y$ -kicks (see Fig. 4.9(a,d)). A state initialized in  $\mathbf{B}$  near the border of regular and chaotic region shows similar periodicity, though not as prominent as that for  $\mathbf{A}$  (see Fig. 4.9(b,e)). For initial state  $\mathbf{C}$  in the chaotic region, we observe no clear periodicity, although the  $J_y$  component shows oscillation as the system periodically gets localized and delocalized with kicks (see Fig. 4.9(c,f)). The experimental data shows a decay in the oscillations due to decoherence and other experimental imperfections. We note that relatively longer time period of three-qubit oscillations compared to that of the two-qubit system. Comparing the periodicity of oscillation, we can see that the period slightly longer for the three-qubit system which completes about three oscillations in 25 kicks, while the two-qubit system completes three and a half oscillations in the same duration. In the case of  $k = 3$ , the period of oscillations decreases with increasing system size. This is clear from the frequency domain picture shown in Fig. 4.6. This is expected since as the system size increases, it approaches the classical limit, thereby suppressing quantum behaviour.

In all the plots, the lowest four traces show correlations

$$C_{\mathbf{S}}(t) = |\langle J^{\mathbf{S}} | J^{\mathbf{Q}}(t) \rangle|^2 \quad (4.15)$$

between  $J^{\mathbf{S}}$  of state  $\mathbf{S}$  and the instantaneous total angular momentum operators  $J^{\mathbf{Q}}(t)$ . The overlap measure allows us to track the localization of the system in states  $\mathbf{A}$  and  $\mathbf{A}'$  as it tunnels between these regular regions. As expected, when the system is initialized in state  $\mathbf{A}$ , we see clear periodic and out-of-phase tunneling oscillations of  $C_{\mathbf{A}(\mathbf{A}')} (t)$  (see Fig. 4.9(a,d)). These tunneling oscillations persist even for near-regular initialization in state  $\mathbf{B}$  due to significant spreading of the low dimensional quantum systems considered here (see Fig. 4.9(b,e)). However, such tunneling

oscillations are washed out for chaotic initialization in state **C** ((see Fig. 4.9(c,f)). Furthermore, the correlation measures  $C_S(t)$  indicate that for the chaotic state, it is widely delocalized. The bottom two traces in Fig. 4.9 capture brief leakage amplitudes to the regions **E** and **E'**, which is the consequence of deep-quantum systems considered here.

### 4.4.3 Robustness of dynamical tunneling

Now that we observe tunneling across a dynamical barrier, it is interesting to see the role of quantum coherence in sustaining tunneling. To this end, we monitor the robustness of dynamical tunneling between regular regions **A** and **A'** under dephasing noise. For this purpose, we use pulsed field gradients (PFG) which introduce a linearly varying magnetic field along the  $z$ -direction and accordingly distributing Larmor frequencies over the length of the sample [48]. PFG along with translational diffusion of molecules, effectively induces strong dephasing in the system. The experimental impact of dephasing on dynamical tunneling are shown in Fig. 4.10 for  $j = 1$  (Fig. 4.10(a-c)) and  $j = 3/2$  systems (Fig. 4.10(d-f)) and for PFG strengths 0 G/cm (Fig. 4.10(a,d)), 0.005 G/cm (Fig. 4.10(b,e)), and 0.05 G/cm (Fig. 4.10(c,f)). The 0 G/cm scenario in Fig. 4.10(a,d) is the same as Fig. 4.9(a,d) and has been replotted here for visual comparison. For reference, we have plotted the theoretical lines in Fig. 4.10 without any dephasing effects. We find that in both  $j = 1$  and  $j = 3/2$  cases, the tunneling behaviour is weakened by dephasing noise. In the two-qubit system, the periodic oscillations survive, but with decaying tunneling amplitudes (see Fig. 4.10(b,c)). In the three-qubit case, even in the presence of weak PFG of 0.005 G/cm the oscillations decay much faster (see Fig. 4.10(e,f)). Here, the correlation measure indicates that the system preferentially larger overlap with the regular region **A** compared to other regular regions. These results indicate the fragility of dynamical tunneling under dephasing noise, and thereby establish the importance of quantum coherence in sustaining the phenomenon.

## 4.5 Summary and outlook

Dynamical tunneling, such as the chaos-assisted tunneling, is a well studied phenomenon and has been demonstrated experimentally in driven cold atomic cloud, microwave annular billiard and has most recently been used to generate NOON states [194]. However, a systematic study

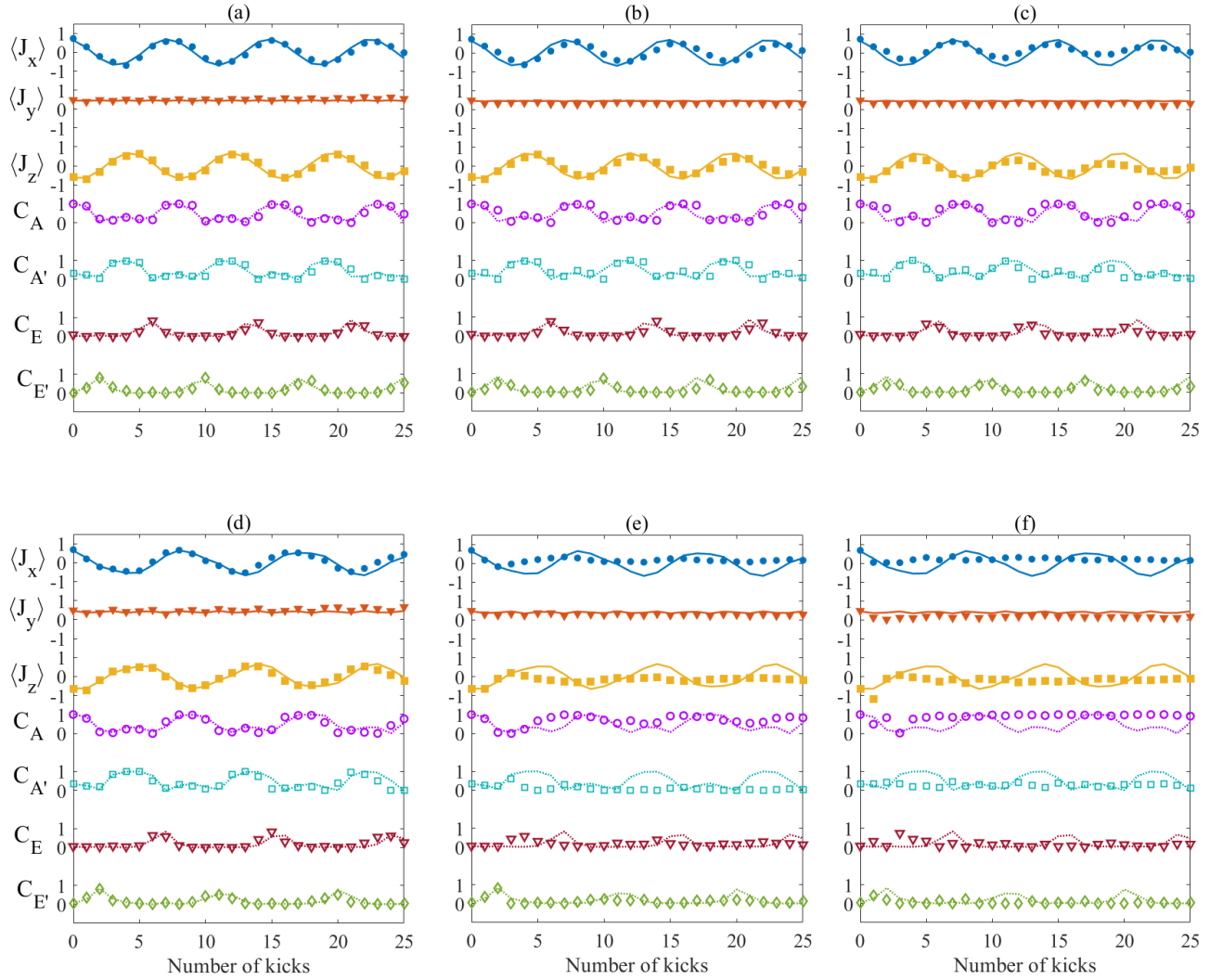


**Figure 4.10:** Effects of dephasing noise on dynamical tunneling in spin-1 QKT realized with two-qubits (a-c) as well as spin-3/2 QKT realized with three-qubits (d-f), with PFG strengths 0 G/cm (a,d), 0.005 G/cm (b,e), and 0.05 G/cm (c,f). In all the cases, the system was initialized in state **A** inside a regular region of Fig. 4.1. The symbols indicate experimental data overlaid on dashed lines corresponding to ideal simulations without any dephasing noise. The upper three traces represent  $\langle J_\alpha(t) \rangle$  and the lower four traces represent  $C_S(t)$ . While both the systems are susceptible to dephasing noise the  $j = 1$  system is relatively more robust in comparison to  $j = 3/2$  system wherein the oscillations have decayed more severely with noise.

of tunneling with system size and different initial conditions was not available. In this work, we have experimentally demonstrated chaos-assisted tunneling in two- and three-qubit systems using NMR based test bed. We initialized the systems to different regions of the phase space – regular, near-regular (border region between regular and chaotic) and chaotic. Following [196], we use  $\langle J_\alpha \rangle$ , the components of the angular momentum operator, as probes to study dynamical tunneling. We observe that the systems initialized in the regular region show periodic oscillation in  $\langle J_\alpha \rangle$ . Systems initialized in the near-regular also show periodicity in  $\langle J_\alpha \rangle$ , but the oscillations are not as perfect as those for the case of initial state in a regular region. Further, systems initialized in a chaotic region show no periodicity. Additionally, by analyzing the norm-distance between the instantaneous total angular momentum operator and that corresponding to either of regular regions, we monitor the periodic tunneling of the system between these regions for different initial conditions.

To understand the significance of quantum coherence in maintaining dynamical tunneling, we studied the robustness of tunneling against dephasing noise. Experimental results showed that while both the spin  $j = 1$  and  $j = 3/2$  systems are susceptible to dephasing noise, the effect was severe for the larger system, wherein the revivals of  $\langle J_\alpha \rangle$  were almost completely destroyed in the presence of dephasing noise.

Tunneling suppression for increasing number of qubits will be related to the  $\hbar$ -scaling in the kicked top model. For the QKT, quantum correlations are known to decay in a power-law form as a function of  $\hbar$  [146]. It will be useful to explore the validity of this prediction for dynamical tunneling in future studies. This is likely to be a challenging exercise from an experimental point of view since it will require maintaining coherence with large number of interacting spins. Further, while it might not be entirely surprising that introduction of noise kills tunneling effects, there are Floquet engineering techniques that allow calibrated disorder while still suppressing decoherence [198, 199]. It will be interesting to explore if such Floquet schemes help sustain chaos-assisted tunneling even in the presence of noise. Another interesting topic to consider would be a scenario of quantum tunneling in the simultaneous presence of a potential-energy barrier as well as a dynamical barrier.

In Chapter 2, we had studied how to characterize quantum chaos in a two-qubit quantum system. It is interesting to note that the same system and model also exhibit dynamical tunneling.

This highlights the multi-faceted aspect of quantum chaos. Quantum chaos is not just a by-product of interacting multi-qubit systems, but has important applications in many other fields - such as generating highly entangled states via dynamical tunneling [194], studying information scrambling using OTOCs and Loschmidt echo [200, 201], thermalization or the lack of it (many-body scars) [113, 202, 203]. Despite extensive interest for decades, quantum chaos and its various aspects are yet to be completely understood.

## CHAPTER 5

---

### Quantum phase-synchronization in a nuclear spin system

---

#### Abstract

Recently there has been significant interest in studying the synchronization of quantum systems. In this work, we experimentally study phase-synchronization in a pair of interacting nuclear spins subjected to an external drive in nuclear magnetic resonance architecture. A weak transition-selective radio-frequency field applied on one of the spins is observed to cause phase-localization, which is experimentally established by measuring the Husimi distribution function under various drive conditions. Moreover, since synchronization experiments require long wait times to allow for the system to reach a steady state, noise in the system overwhelms the signal and standard state tomography techniques prove ineffective. To this end, we have developed a general interferometric technique to directly extract values of the Husimi function via the transverse magnetization of the undriven nuclear spin. We further verify the robustness of synchronization to detuning in the system by studying the Arnold tongue behaviour.

#### Reported in

**V. R. Krithika**, Parvinder Solanki, Sai Vinjanampathy, and T. S. Mahesh, *Observation of quantum phase-synchronization in a nuclear spin-system*, [Phys. Rev. A 105, 062206 \(2022\)](#).

## 5.1 Introduction

In this chapter, we move to a quintessential feature of nonlinear systems - synchronization. Synchronization is the entrainment of a self-sustained oscillator to an external drive or another oscillator via mutual coupling between the systems [204]. It is a ubiquitous phenomenon in classical

nonlinear systems and has been a subject of widespread study in systems ranging from coupled pendula to syncing of flashing in fireflies and neuronal firing activities [204]. Motivated by the stability and universality of classical synchronization, quantum synchronization has also been a field of intense study. Platforms that exhibit quantized dynamics have inspired theoretical studies in systems such as trapped ions [205, 206], superconducting circuits [207], atomic ensembles [208], optomechanical systems [209–212] and nanomechanical systems [213, 214]. Theoretical studies have shown fundamental implications of synchronization to other fields such as entanglement generation [215, 216], thermodynamics [217, 218], quantum networks [219] and continuous time crystals [220].

Following the definition of classical synchronization [204], quantum synchronization can be understood as the adjustment of rhythms of quantum limit cycle oscillators under the effect of weak coupling or an external drive [216, 218, 221, 222]. Quantum synchronization proceeds by first considering the quantum analogue of phase space, which is one of many quasiprobability distributions such as Husimi function and Wigner function [223]. In order to study synchronization in a quantum system, a valid limit cycle which is robust against external perturbations and possesses a neutral free phase [204] must first be established. Thermal states were shown to be examples of such limit cycle states, showing equiprobable distribution of phases in phase space [217]. Such phase space distribution functions have been used to construct measures of synchronization [210, 224–227]. Following several studies of synchronization in specific systems, unified measures of quantum synchronization based on relative entropies have also been formulated [222]. They used information theoretic measures based on quantum correlations, which have been shown to measure synchronization [216, 228, 229]. These measures reduce to the phase space based measures under the system specific conditions [222].

Following the theoretical interest in this subject [210, 211, 216–218, 221, 222, 230–236], quantum synchronization has been experimentally demonstrated recently in the IBM quantum computer [237] and spin-1 cold atoms [238]. The experimental demonstration of quantum synchronization is in general a challenging task owing to the difficulty in extracting required parameters. Quantum synchronization measurements typically require the system to settle into a steady state, which necessitates the need for long waiting times. Such long wait times allow for other experimental noise sources to interfere with the signal. Besides this, tomographic reconstruction

of the state scales with the system size, requiring  $O(n^2)$  measurements for a system of dimension  $n$  [239]. Thus, the steady state characteristics of the system are in general challenging to measure and are often inferred by extrapolating transient dynamics or by devising complicated measurement schemes. In this work, we resolve the aforementioned issues and report the observation of synchronization in nuclear spins using NMR. NMR architecture's ease of control and manipulation in addition to inherent relaxation mechanisms, which cause the system to thermalize, offers an ideal platform to observe synchronization

## 5.2 Objectives

In this work, we experimentally study quantum phase-synchronization in a four-level system. This system is constituted by a pair of interacting spin-1/2 nuclei, and we observe its synchronization with a weak transition-selective RF field applied on one of the spins in the following way:

- (i) We develop the theoretical formulation to characterize the phase space using Husimi distribution function for the four-level system.
- (ii) Typically, experimental estimation of Husimi distribution requires quantum state tomography (QST) [197]. However, QST after a long external drive proved to be highly inefficient because, as the steady state is approached, the irradiated levels saturate and relevant transitions become too faint. We overcame this by introducing a new interferometric technique that can experimentally capture the Husimi distribution directly.
- (iii) Using this technique, we study the limit cycle behaviour and demonstrate synchronization of the system with a weak external drive for different drive durations, which allows us to investigate transient as well as steady state behaviour.
- (iv) We also explore the robustness of synchronization against detuning frequency and drive strength via the Arnold tongue.

From such studies, one can envisage implications of quantum synchronization in areas such as spectroscopy, quantum computing, and quantum thermodynamics.

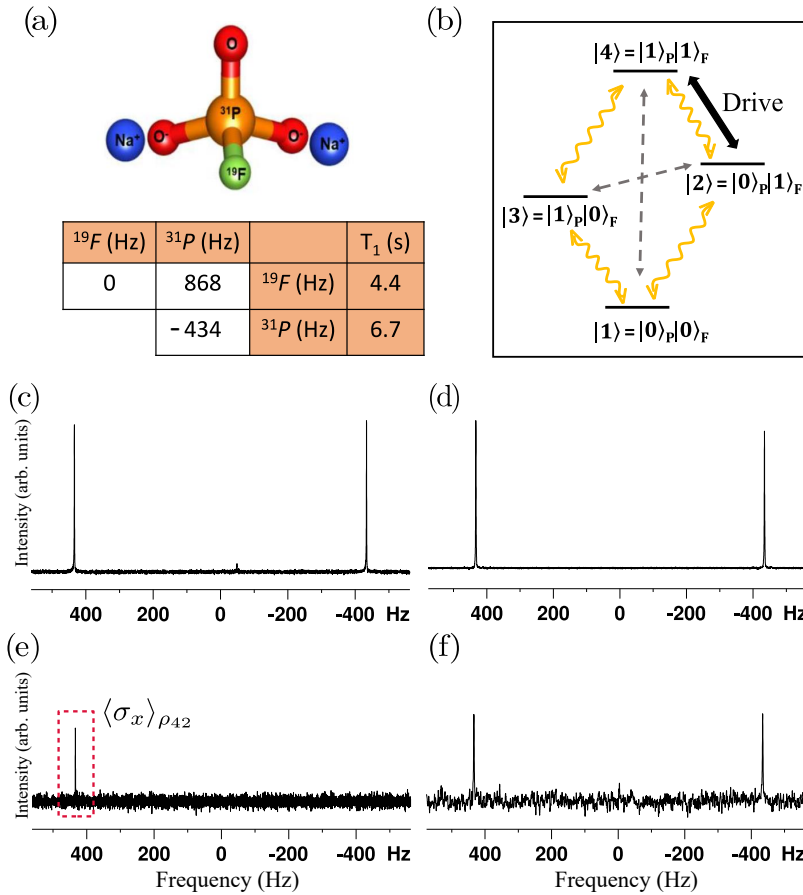


**Figure 5.1:** (a) Sodium fluorophosphate molecular structure with its Hamiltonian parameters and the spin-lattice relaxation time constants ( $T_1$ ) shown in the table. The diagonal elements represent the offset, while off-diagonal element represents the scalar  $J$  coupling constant. Figure (b) represents the energy levels of the two-qubit system with four non-degenerate energy eigenstates. The numerical model presented here considers only the single-quantum relaxation pathways (yellow curved arrows) and ignores the zero- and double-quantum pathways (dashed grey arrows). Figures (c,d) show reference NMR spectra of  $^{31}\text{P}$  and  $^{19}\text{F}$  spins respectively, each obtained with a  $90^\circ$  pulse on thermal equilibrium state, while (e) shows the  $^{31}\text{P}$  NMR signal after 100 s drive on the  $|2\rangle \leftrightarrow |4\rangle$  transition. Intensity of the  $\rho_{42}$  element is indicated in the dashed box, which is used for the Arnold tongue analysis. Figure (f) shows the  $^{19}\text{F}$  NMR spectrum at the end of interferometric circuit from which we can directly extract the Husimi distribution at a particular  $\theta$  and  $\phi$  values.

### 5.3 Synchronization of a four-level system

We consider a non-degenerate four-level system composed of  $^{19}\text{F}$  and  $^{31}\text{P}$  nuclei in sodium fluorophosphate molecule, as shown in Fig. 5.1(a,b) and study the phase synchronization of the system with an external drive. It is customary to use spin coherent states, whose evolutions are closest to classical trajectories, to study synchronization [240]. Furthermore, they are used to characterize the phase space using Husimi distribution function, as explained below. For a spin-1/2 particle, the  $z$  projection of the spin angular momentum  $S_z$  is quantized into  $2s+1$  levels  $|S, m_s\rangle$  with eigenvalues  $m_s = -1/2, 1/2$ . The spin coherent state for this spin in  $\text{SU}(2)$  group can be described as a rotation of the extremal state  $|S, S\rangle$  such that [152, 241]

$$|\hat{n}_2\rangle = |\theta, \phi\rangle = e^{-i\phi S_z} e^{-i\theta S_y} |S, S\rangle = \begin{pmatrix} \cos \frac{\theta}{2} \\ e^{i\phi} \sin \frac{\theta}{2} \end{pmatrix}, \quad (5.1)$$

where  $\theta \in [0, \pi]$  and  $\phi \in [0, 2\pi]$ . It is obvious that spin-1/2 coherent states can be mapped to points on the surface of the Bloch sphere. The recursive construction of spin coherent state vectors for an  $n$ -level non-degenerate system proposed by Kae Nemoto [241] is as follows

$$|\hat{n}_n\rangle = \begin{pmatrix} \cos \frac{\theta}{2} \\ 0 \\ \vdots \\ 0 \end{pmatrix} + e^{i\phi} \sin \frac{\theta}{2} \begin{pmatrix} 0 \\ \vdots \\ |\hat{n}_{n-1}\rangle \end{pmatrix}. \quad (5.2)$$

Note that each lower-level vector  $|\hat{n}_{n-1}\rangle$  is made up of a new pair of angular variables. For the four-level  $\text{SU}(4)$  system used in this work, the extent of phase localization of the system in a state  $\rho$  can be quantified using the Husimi-Kano Q representation function [157, 158], which can be defined as

$$Q(\theta_1, \theta_2, \theta_3, \phi_1, \phi_2, \phi_3) = \frac{24}{\pi^3} \langle \hat{n}_4 | \rho | \hat{n}_4 \rangle, \quad (5.3)$$

where

$$|\hat{n}_4\rangle = \begin{pmatrix} C_{\theta_1} \\ e^{i\phi_1} S_{\theta_1} C_{\theta_2} \\ e^{i\phi_2} S_{\theta_1} S_{\theta_2} C_{\theta_3} \\ e^{i\phi_3} S_{\theta_1} S_{\theta_2} S_{\theta_3} \end{pmatrix}. \quad (5.4)$$

is SU(4) coherent state [241–243] with  $C_{\theta_i} = \cos(\theta_i/2)$  and  $S_{\theta_i} = \sin(\theta_i/2)$ . The normalization of the Q-function arises from the completeness relation of coherent state  $|\hat{n}_4\rangle$  defined as

$$\int |\hat{n}_4\rangle\langle\hat{n}_4| d\mu = \frac{\pi^3}{24} \mathbb{1}, \quad (5.5)$$

where the integration is taken over the Haar measure and volume element given by [241]

$$d\mu = d\theta_1 d\theta_2 d\theta_3 d\phi_1 d\phi_2 d\phi_3 C_{2\theta_1} S_{2\theta_1}^5 C_{2\theta_2} S_{2\theta_2}^3 C_{2\theta_3} S_{2\theta_3}.$$

For a system with internal Hamiltonian  $H_0 = \sum_{i=1}^4 \omega_i |i\rangle\langle i|$  having characteristic frequencies  $\omega_i$ , they evolve as

$$e^{-iH_0 t} |\hat{n}_4\rangle \rightarrow \begin{pmatrix} C_{\theta_1} \\ e^{i(\phi_1 - \omega_{21}t)} S_{\theta_1} C_{\theta_2} \\ e^{i(\phi_2 - \omega_{31}t)} S_{\theta_1} S_{\theta_2} C_{\theta_3} \\ e^{i(\phi_3 - \omega_{41}t)} S_{\theta_1} S_{\theta_2} S_{\theta_3} \end{pmatrix}, \quad (5.6)$$

where  $\omega_{i1} = \omega_i - \omega_1$ . From the above equation, we can see that under free evolution of internal Hamiltonian,  $\phi_i$ s represent the free phases (akin to free phases in classical oscillators) oscillating with the respective frequencies  $\omega_{i1}$  while  $\theta_i$ s govern the populations of the system which remains fixed. In the absence of any external perturbation, the steady state reached by thermalization has uniform phase distribution, and the Husimi Q-function remains independent of  $(\phi_1, \phi_2, \phi_3)$ . This points to the fact that the given system has free phases available. Along with the existence of free phases, a system needs to be nonlinear in nature to exhibit limit cycle behaviour. Since the dynamics of a multilevel quantum system is generally nonlinear, the availability of free phases makes it a perfect candidate to study synchronization. On application of a weak external drive

the system may develop a definite phase relationship with the drive, thus resulting in a localized phase distribution. This phenomenon, known as phase synchronization, is captured and quantified by

$$S(\phi_1, \phi_2, \phi_3) = \int d\Theta Q(\theta_1, \theta_2, \theta_3, \phi_1, \phi_2, \phi_3) - \frac{1}{(2\pi)^3}, \quad (5.7)$$

where  $d\Theta = d\theta_1 d\theta_2 d\theta_3 C_{2\theta_1} S_{2\theta_1}^5 C_{2\theta_2} S_{2\theta_2}^3 C_{2\theta_3} S_{2\theta_3}$ . For the four-level system considered here, the above expression leads to

$$S(\phi_1, \phi_2, \phi_3) = \frac{1}{16\pi^2} \text{Re} \left[ \rho_{43} e^{i\phi_1} + \rho_{42} e^{i\phi_2} + \rho_{41} e^{i\phi_3} + \rho_{32} e^{i(\phi_2 - \phi_1)} + \rho_{31} e^{i(\phi_3 - \phi_1)} + \rho_{21} e^{i(\phi_3 - \phi_2)} \right], \quad (5.8)$$

where  $\rho_{ij} = \langle i | \rho | j \rangle$ .

Under the effect of thermal baths and in the absence of external perturbations/drive, the system reaches its thermal equilibrium state, that is diagonal in the energy eigenbasis of the internal Hamiltonian. The Husimi Q-function for a diagonal state reduces to a uniform distribution showing no phase localization. Therefore the thermal state constitutes a valid limit cycle state which is stable to external perturbation and has free phases [217, 222]. Furthermore, the synchronization measure  $S(\phi_1, \phi_2, \phi_3)$  registers zero for such limit cycle state.

### 5.3.1 System with drive

We now consider the entrainment of the given limit cycle oscillator with an external drive. A drive having strength  $\Omega$  and frequency  $\omega_d$  is applied on the  $|2\rangle \leftrightarrow |4\rangle$  transition (see Fig. 5.1 b). The Hamiltonian describing the system with this drive is given by

$$H = \sum_{i=1}^4 \omega_i |i\rangle \langle i| + \Omega (|2\rangle \langle 4| e^{i\omega_d t} + |4\rangle \langle 2| e^{-i\omega_d t}). \quad (5.9)$$

In the rotating frame of the drive described by the unitary transformation

$$\exp(i\{(\omega_d + \omega_2)|4\rangle \langle 4| + \omega_3|3\rangle \langle 3| + \omega_2|2\rangle \langle 2| + \omega_1|1\rangle \langle 1|\}t),$$

the total Hamiltonian becomes  $H_R = \Delta|4\rangle\langle 4| + \Omega(|2\rangle\langle 4| + |4\rangle\langle 2|)$ , where  $\Delta = (\omega_4 - \omega_2) - \omega_d$ . For the  $|2\rangle \leftrightarrow |4\rangle$  drive considered here, the only surviving coherence under steady state is  $\rho_{42}$  (and its adjoint  $\rho_{24}$ ). Therefore dropping all other coherence terms, and relabelling  $\phi_2$  as  $\phi$ , the Q-function defined in Eq. (5.3) can be expressed as

$$Q(\theta_1, \theta_2, \theta_3, \phi) = \text{Re}(\rho_{42}e^{i\phi}) S_{\theta_1} S_{\theta_2} C_{\theta_3} + \rho_{11} S_{\theta_1}^2 S_{\theta_2}^2 S_{\theta_3}^2 + \rho_{22} S_{\theta_1}^2 S_{\theta_2}^2 C_{\theta_3}^2 + \rho_{33} S_{\theta_1}^2 C_{\theta_2}^2 + \rho_{44} C_{\theta_1}^2. \quad (5.10)$$

Since the drive is not sensitively affecting the levels  $|1\rangle$  and  $|3\rangle$ , without any loss of generality we can effectively set  $\theta_2 = \pi$ ,  $\theta_3 = 0$  and replace  $\theta_1 \rightarrow \theta$  in the above equation, which further simplifies the Husimi function to

$$Q(\theta, \phi) = \rho_{44} C_{\theta}^2 + \text{Re}(\rho_{42}e^{i\phi}) S_{2\theta} + \rho_{22} S_{\theta}^2. \quad (5.11)$$

From the above equation it is clear that non-zero  $\rho_{42}$  leads to the localization of the corresponding phase variable  $\phi$  in Husimi Q-function. Such a state corresponds to the synchronized state. The synchronization measure  $S(\phi_1, \phi_2, \phi_3)$  corresponding to Eq. (5.8) also reduces to

$$S(\phi) = \frac{\text{Re}(\rho_{42}e^{i\phi})}{16\pi^2} \text{ and } \max[S(\phi)] = \frac{|\rho_{42}|}{16\pi^2}, \quad (5.12)$$

which is non-zero only for  $\rho_{42} \neq 0$ , similar to [217].

## 5.4 Experimental setup

In this section, we explain the spin system used to study quantum phase-synchronization, followed by the numerical model to simulate the open system dynamics, the optimization of drive amplitude to observe synchronization derived from the numerical model, and finally the interferometric technique developed to directly readout the Husimi distribution function value in the experiments.

### 5.4.1 Spin system and the drive

In this work, we considered a two-qubit system formed by the spin-1/2 nuclei  $^{19}\text{F}$  and  $^{31}\text{P}$  of sodium fluorophosphate molecule dissolved in  $\text{D}_2\text{O}$  solvent (5.3 mg of solute in 600  $\mu\text{l}$  of solvent) and maintained at an ambient temperature of 298 K. All experiments were performed on a high resolution Bruker 500 MHz NMR spectrometer operating at a magnetic field strength of  $B_0 = 11.4$  T. Fig. 5.1(a) displays the spin system and its Hamiltonian parameters including scalar spin-spin coupling constant ( $\mathcal{J}$ -coupling), as well as the RF offsets  $\nu_P, \nu_F$  with respect to the Larmor frequencies  $\omega_P = -\gamma_P B_0, \omega_F = -\gamma_F B_0$ , where  $\gamma_i$  are the gyromagnetic ratios. Note that  $\nu_P$  is set to  $-\mathcal{J}/2$ , while  $\nu_F$  is set to zero. Fig. 5.1(b) shows the Zeeman energy level diagram of this two-qubit system. The lab-frame Hamiltonian is of the form

$$H_{\text{NMR}} = \omega_P I_z^P + \omega_F I_z^F + 2\pi \mathcal{J} I_z^P I_z^F. \quad (5.13)$$

As explained in Sec. 1.3 of Chapter 1, the thermal energy in NMR systems at ambient temperatures is much greater than the Zeeman energy splitting. Hence, an  $n$ -qubit system at thermal equilibrium is in a highly mixed state given by

$$\rho^{\text{eq}} = \exp\left(\frac{-H_0}{k_B T}\right) = \mathbb{1}/2^n + \sum_i \epsilon_i I_z^i, \quad (5.14)$$

where  $\epsilon = \hbar\gamma_i B_0 / (2^n k_B T) \sim 10^{-5}$  is the purity factor. The population distribution in the high-temperature limit follows the Boltzmann distribution. The inherent relaxation ( $T_1$ ) mechanism facilitates dissipation, and helps establish equilibrium population distribution, which forms a stable limit cycle with free phases as discussed in the previous section. The thermal equilibrium spectra of  $^{31}\text{P}$  and  $^{19}\text{F}$  spins are shown in Fig. 5.1 (c,d) respectively.

To realize synchronization, we applied a weak drive of amplitude  $\Omega \approx 0.1$  Hz (optimization of drive amplitude is explained in Sec. 5.4.3) selectively on the  $|2\rangle \leftrightarrow |4\rangle$  transition as indicated in Fig. 5.1 (b). The total Hamiltonian in the doubly rotating frame is given by

$$H_{\text{tot}} = H_0 + V \text{ where,} \\ H_0 = -2\pi\nu_P I_z^P + 2\pi\mathcal{J} I_z^P I_z^F \text{ and } V = 2\pi\Omega I_y^P. \quad (5.15)$$

The first term with  $\nu_P = -\mathcal{J}/2$  makes the drive on-resonant with the  $|2\rangle \leftrightarrow |4\rangle$  transition of the  $^{31}\text{P}$  qubit that prepares  $\rho_{42}$  coherence (see Fig. 5.1(e)), while the dissipation mechanism redistributes the populations of the system.

## 5.4.2 Steady state dynamics

In this section, we describe a simple model to estimate the instantaneous state of the two-qubit system under different drive conditions. The time evolution of a quantum system is given by the master equation [244]

$$\frac{d\rho}{dt} = -i[H_0 + V, \rho] + \mathcal{D}[\hat{O}_+] \rho + \mathcal{D}[\hat{O}_-] \rho \quad (5.16)$$

where  $H_0$  is the internal Hamiltonian of the system and  $V$  represents the external drive. The thermal bath at a temperature  $T$  is modeled by the Lindblad superoperators  $\mathcal{D}[\hat{O}_+] \rho + \mathcal{D}[\hat{O}_-] \rho$ . The single quantum upward transitions (indicated by yellow curves in Fig. 5.1(b)) are described by the jump operator  $\mathcal{D}[\hat{O}_+] \rho$  accompanied by their corresponding transition probabilities and rates. The equivalent downward transitions are described by the Hermitian conjugate  $\mathcal{D}[\hat{O}_-] \rho$ . The single-quantum transition of the first qubit implies that the system in a state  $|i\rangle|j\rangle$  goes to the state  $|k\rangle|l\rangle$ , where  $k = i \pm 1$ , and  $l = j$ . The same can be extended to the single-quantum transition of the second qubit. The Lindblad superoperator for upward transitions of the combined two-qubit system is hence given by  $\mathcal{D}[\hat{O}_+] \rho = \sum_{(k=i\pm 1, l=j)} D[\mathcal{O}_{ij}^{kl}] \rho + \sum_{(k=i, l=j\pm 1)} D[\mathcal{O}_{ij}^{kl}] \rho$  where  $D[\hat{O}] \rho = \hat{O} \rho \hat{O}^\dagger - \{\hat{O}^\dagger \hat{O}, \rho\}/2$  and jump operator  $\mathcal{O}_{ij}^{kl}$  is defined as  $\mathcal{O}_{ij}^{kl} = \sqrt{g_{ij}^{kl} p_{ij}^{kl}} |k\rangle|l\rangle\langle i|\langle j|$ . Similarly, we can write  $\mathcal{D}[\hat{O}_-] \rho = \sum_{(k=i\pm 1, l=j)} D[\mathcal{O}_{kl}^{ij}] \rho + \sum_{(k=i, l=j\pm 1)} D[\mathcal{O}_{kl}^{ij}] \rho$ , where  $\mathcal{O}_{kl}^{ij} = (\mathcal{O}_{ij}^{kl})^\dagger$ . The coefficients of the jump operators corresponding to each qubit determine the transition rate given by  $g_{ij}^{kl}$ , and the transition probability given by  $p_{ij}^{kl}$ . The transition rate of each spin is related to the bath temperature  $T$  via its spin-lattice relaxation time  $T_1^i$  as  $g_i = 2\pi/T_1^i$  (see Fig. 5.1(a) for  $T_1$  values). The transition probabilities  $p_{ij}^{kl}$  can be identified with upward or downward transitions of a particular spin. We estimate these probabilities via the Fermionic bath model [245]. Relabelling the upward & downward transitions of  $n$ th spin as  $p_{n\pm}$ , we may write

$$p_{n+} = \frac{1}{e^{4\epsilon_n} + 1} \quad \text{and} \quad p_{n-} = 1 - p_{n+}, \quad (5.17)$$

which help maintain detailed balance.

The master equation in Eq. (5.16) is linear in  $\rho$  and can be written as follows

$$|\dot{\rho}\rangle\rangle = \mathcal{L}|\rho\rangle\rangle = (\mathcal{L}_0 + \mathcal{L}_V)|\rho\rangle\rangle \quad (5.18)$$

where  $\mathcal{L}$  represents the Liouvillian superoperator describing the open system dynamics and  $|\rho\rangle\rangle$  is the vectorised form of density matrix in Liouville space. The mathematical form of  $\mathcal{L}$  can be obtained by applying the transformation  $B\rho C \rightarrow C^* \otimes B|\rho\rangle\rangle$  to the master equation where  $|\rho\rangle\rangle$  is obtained by vertically stacking the columns of density matrix [218, 246–248].

The Liouvillian superoperator  $\mathcal{L}$  can be decomposed into two parts as shown in Eq. (5.18). The first part  $\mathcal{L}_0$  defines the dynamics of system in absence of external drive ( $V=0$ ) and is given by

$$\begin{aligned} \mathcal{L}_0 &= -i(I \otimes H_0 - H_0^* \otimes I) + \sum_{j=+,-} O_j^T \otimes O_j \\ &\quad - \frac{1}{2}(I \otimes O_j^\dagger O_j + O_j^T O_j^* \otimes I). \end{aligned} \quad (5.19)$$

The second term  $\mathcal{L}_V$  represents the superoperator corresponding to an external perturbation  $V$  which is given by

$$\mathcal{L}_V = -i(I \otimes V - V^* \otimes I). \quad (5.20)$$

The instantaneous state  $\rho(t)$  after solving Eq. (5.18) is given by

$$\rho(t) = e^{\mathcal{L}t} \rho_0, \quad (5.21)$$

where  $\rho_0$  represents the initial state of the system. The steady state is given by converging solution of Eq. (5.18), defined as  $\rho_{ss} = \lim_{t \rightarrow \infty} e^{\mathcal{L}t} \rho_0$ . Therefore the steady state corresponds to the eigenstate of Liouvillian superoperator having zero eigenvalue [249]. In the absence of external

drive, one obtains a diagonal steady state,

$$\rho^{\text{ss}} = \begin{bmatrix} \rho_{44}^{\text{ss}} & 0 & 0 & 0 \\ 0 & \rho_{33}^{\text{ss}} & 0 & 0 \\ 0 & 0 & \rho_{22}^{\text{ss}} & 0 \\ 0 & 0 & 0 & \rho_{11}^{\text{ss}} \end{bmatrix}, \quad (5.22)$$

with elements following the thermal distribution. In the presence of an external drive  $V$ , the steady state corresponds to the eigenstate of  $\mathcal{L}$  having zero eigenvalue and is of the form

$$\rho^{\text{ss}} = \begin{bmatrix} \rho_{44}^{\text{ss}} & 0 & \rho_{42}^{\text{ss}} & 0 \\ 0 & \rho_{33}^{\text{ss}} & 0 & 0 \\ \rho_{24}^{\text{ss}} & 0 & \rho_{22}^{\text{ss}} & 0 \\ 0 & 0 & 0 & \rho_{11}^{\text{ss}} \end{bmatrix}. \quad (5.23)$$

Here, the basis states are ordered according to decreasing energy eigenvalues. Also note that since the external drive is very weak, the steady state attained is close to the limit cycle, *i.e.*,  $\rho_{ii}^{\text{ss}} \approx \rho_{ii}^{\text{eq}}$ .

We would like to emphasise that it is a highly non-trivial task to measure all the Lindblad dissipation operators for the NMR system [250]. The dynamics in the system is vastly more complex than the model considered here can capture. The set of operators comprising this model is very minimal and intended only to capture the effective dissipation effects. A full description of the NMR system would involve many more terms not considered in our minimal model.

### 5.4.3 Optimum drive amplitude

The strength of the drive is crucial to realising synchronization in any system. A very weak drive will barely perturb the system, while a very strong drive will induce forced behaviour and alter the limit cycle. It is hence vital to limit the drive strength within an appropriate regime to achieve synchronization. For our system, we estimate the optimum drive strength using the numerical model described in Sec. 5.4.2. We vary the drive strength and numerically obtain the

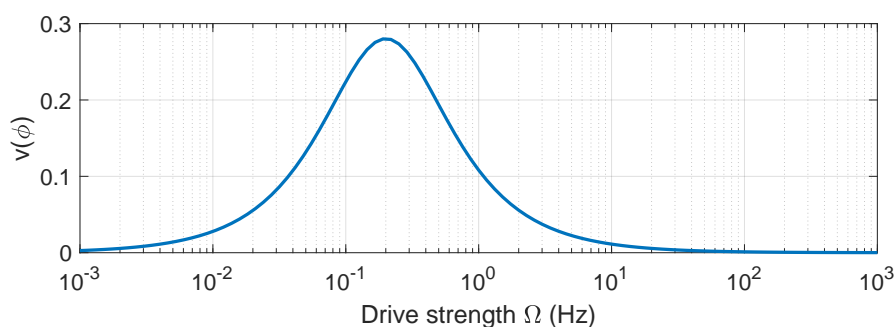


**Figure 5.2:** The dependence of visibility of phase-localization versus drive amplitude  $\Omega$ , showing an optimum strength at around 0.1 Hz.

corresponding steady-state, for which we estimate the visibility of the Husimi distribution

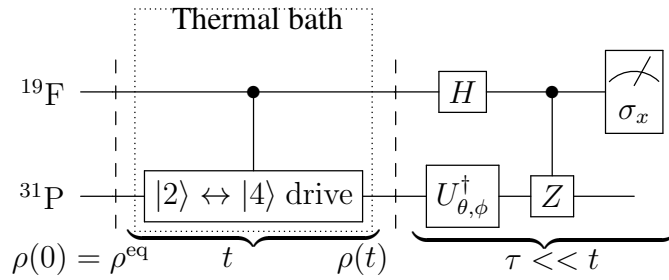
$$v(\phi) = \frac{\max(Q_\phi) - \min(Q_\phi)}{\max(Q_\phi) + \min(Q_\phi)}, \quad (5.24)$$

where  $Q_\phi = \sum_\theta Q(\theta, \phi)$ . Note that visibility quantifies the extent of phase-localization. The result is shown in Fig. 5.2. The drive amplitude was varied from  $10^{-3}$  Hz to  $10^3$  Hz. We can see that the visibility function is negligible for very low powers and then peaks at around  $10^{-1}$  Hz before dropping to zero at higher drive amplitudes. We thus chose a drive strength of 0.1 Hz for the experimental study of synchronization. The experimental method to calibrate such a low amplitude drive pulse is explained in the results section Sec. 5.5.1.

#### 5.4.4 Interferometric measurement of Husimi distribution

The Husimi function can theoretically be evaluated using Eq. (5.3) from the instantaneous state directly predicted by solving the master equation. Experimentally, the standard way to extract Husimi distribution is by using Eq. (5.3) after carrying out QST to estimate the steady state density matrix  $\rho$  [197]. However, tomographic measurements in quantum systems suffer from two main issues. Firstly, the experimental complexity of QST scales exponentially with system size [251, 252], where each component has to be measured repeatedly. This introduces deleterious noise sources when multiple experiments are needed to perform QST. For small quantum systems such as a four-level system, full state tomography is routinely performed. However, even in the small system size of four-levels considered here, the second issue was that QST of steady states turned out to be highly inefficient. This was because QST relies on determining each element of

(a)



(b)

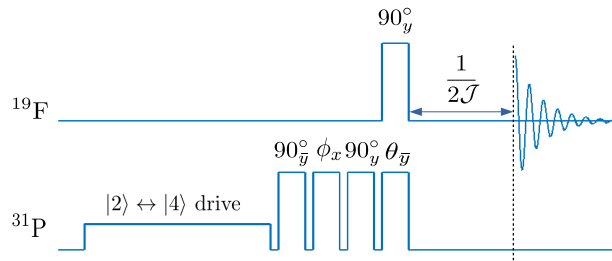


**Figure 5.3:** (a) IMHD circuit for direct measurement of Husimi distribution where the drive duration  $t$  is much longer than the measurement sequence time  $\tau$  and (b) the corresponding NMR pulse sequence.

the density matrix via a linear combination of expectation values of a set of observables. If the expectation values vary over large magnitudes, the estimation of very small magnitude elements by inverting the system of linear equations from multiple experimental measurements suffers from dynamic range problem. Furthermore, NMR signals are proportional to the population differences. Since the populations are in a pseudo-spin state, their effective difference dips below the noise threshold, rendering steady state population tomography difficult in such systems. The interferometric method described here avoids the dynamic range problem and directly extracts the Husimi function at each  $(\theta, \phi)$  value in a single experiment without requiring the elaborate QST protocols. This allowed us to efficiently observe and quantify synchronization even after a very long drive durations.

The circuit diagram describing the experiment to read the Husimi Q-function values is shown in Fig. 5.3(a). Here,  $^{19}\text{F}$  qubit acts as the ancillary system, which along with  $^{31}\text{P}$  qubit begin from a thermal equilibrium state  $\rho^{\text{eq}}$ . The long weak-drive responsible for synchronization is applied on the  $|2\rangle \leftrightarrow |4\rangle$  transition of  $^{31}\text{P}$  qubit. As part of the interferometer, we now apply a Hadamard operator on  $^{19}\text{F}$  qubit and prepare its superposition. Meanwhile, we apply the gate  $U_{\theta, \phi}^\dagger$  on  $^{31}\text{P}$

qubit. Subsequently, we apply a controlled phase-gate  $\mathbb{1}_P \otimes |0\rangle\langle 0|_F - \sigma_z^P \otimes |1\rangle\langle 1|_F$ .

Starting from the extremal state  $|0, 0\rangle = |\theta = 0, \phi = 0\rangle$ , we can generate the spin coherent state

$$|\theta, \phi\rangle = U_{\theta, \phi}|0, 0\rangle = [e^{-i\phi S_z} e^{-i\theta S_y} \otimes \mathbb{1}^F] |0, 0\rangle. \quad (5.25)$$

The corresponding interferometric measurement of Husimi distribution (IMHD) reading is

$$\begin{aligned} Q_{\text{IF}}(\theta, \phi) &= \langle \theta, \phi | \rho^{\text{ss}} | \theta, \phi \rangle = \text{Tr}(\rho^{\text{ss}} | \theta, \phi \rangle \langle \theta, \phi |) \\ &= \text{Tr}(\rho^{\text{ss}} U_{\theta, \phi} |0, 0\rangle \langle 0, 0| U_{\theta, \phi}^\dagger) \\ &= \text{Tr}(U_{\theta, \phi}^\dagger \rho^{\text{ss}} U_{\theta, \phi} |0, 0\rangle \langle 0, 0|) \\ &= \langle 0, 0 | \langle 0, 0 | \rho_{\theta, \phi} \end{aligned} \quad (5.26)$$

where  $\rho_{\theta, \phi} = U_{\theta, \phi}^\dagger \rho^{\text{ss}} U_{\theta, \phi}$ .

The NMR pulse sequence for IMHD is shown in Fig. 5.3(b). After the  $|2\rangle \leftrightarrow |4\rangle$  drive, we implement a pseudo-Hadamard operator using a  $90_y^\circ$  pulse on the  $^{19}\text{F}$  spin. While  $U_\theta^\dagger = e^{i\theta I_y}$  can be realized by a single  $\theta_y$  pulse,  $U_\phi^\dagger = e^{i\phi I_z} = e^{-i\frac{\pi}{2} I_y} e^{-i\phi I_x} e^{i\frac{\pi}{2} I_y}$  is realized by a sequence of three pulses. The measurement of  $|0, 0\rangle\langle 0, 0|$  projector can be realized via a controlled phase-gate, which can be implemented, up to a phase-factor, by a simple free evolution under the system Hamiltonian  $2\pi \mathcal{J} I_z^P I_z^F$  for a time duration of  $1/2\mathcal{J}$ . A subsequent measurement of transverse magnetization of the  $^{19}\text{F}$  spin yields the NMR signal

$$\begin{aligned} s = \text{Re}\langle \sigma_x^F \rangle &= \frac{1}{2} \{ C_{2\theta} [\rho_{11}^{\text{ss}} - \rho_{22}^{\text{ss}} - \rho_{33}^{\text{ss}} + \rho_{44}^{\text{ss}}] \\ &\quad + S_{2\theta} \text{Re}(e^{-i\phi} \rho_{24}^{\text{ss}} + e^{i\phi} \rho_{42}^{\text{ss}}) \}. \end{aligned} \quad (5.27)$$

One can verify from Eq. (5.10) and Eq. (5.27) that

$$\begin{aligned} Q_{\text{IF}}(\theta, \phi) &= \frac{24}{\pi^3} \left[ \frac{1+2s}{2} - (\rho_{11}^{\text{ss}} C_\theta^2 + \rho_{33}^{\text{ss}} S_\theta^2) \right] \\ &= Q(\theta, \phi). \end{aligned} \quad (5.28)$$

Here  $\rho_{11}^{ss} \simeq \rho_{11}^{eq}$  and  $\rho_{33}^{ss} \simeq \rho_{33}^{eq}$  are the populations of undriven levels and can be estimated from the thermal equilibrium population distribution. For the highly mixed NMR systems,  $\rho_{11} \simeq \rho_{33} \simeq 1/4$ , so that,

$$Q_{\text{IF}}(\theta, \phi) = \frac{24}{\pi^3} \left[ \frac{1 + 2s}{2} - \frac{1}{4} \right] = \frac{24}{\pi^3} \left[ s + \frac{1}{4} \right]. \quad (5.29)$$

Thus, the  $^{19}\text{F}$  signal after the IMHD circuit of Fig. 5.3 can directly measure the Husimi distribution values. One such spectrum for a particular drive duration and  $(\theta, \phi)$  values is shown in Fig. 5.1(f). One could use a third spin as an ancilla qubit for the interferometer circuit, but this will open up additional dissipation pathways. To minimise such decoherence channels, here we have used one of the system spins itself as an ancilla qubit.

## 5.5 Results and discussion

### 5.5.1 Low power RF calibration

We first explain the calibration of low power pulses in the NMR architecture. The experimental calibration of such very weak RF pulses is nontrivial, since the signal to noise ratio is negligibly small. For this purpose, we used a spin-system trimethylphosphite dissolved in dimethylsulphoxide solvent, which is different from the spin-system to study synchronization. We specifically chose this sample because of its star-topology with  $^{31}\text{P}$  at the centre coupled to nine identical  $^1\text{H}$  nuclei with a scalar  $\mathcal{J}$  coupling constant of 11 Hz, as shown in Fig. 5.4. Such geometry is highly preferable since the magnetization of the nine high  $\gamma$  proton nuclei can be easily transferred to the central  $^{31}\text{P}$  nucleus via a standard NMR technique INEPT and further algorithmic cooling, thus boosting its signal [253]. This gives better signal to noise ratio and hence more accurate calibration values. Note that the calibration of the RF coils is not dependent on the sample. The solvent dielectric constant does affect the pulse calibration in the sample, but it is a second order effect and can hence be ignored. The low power drive pulse was calibrated sequentially from a hard pulse such that it maintained the relation  $\alpha = \gamma_i B_{\text{RF}} \tau = P \tau$  where  $\alpha$  is the flip angle,  $B_{\text{RF}}$  is the amplitude of the RF-pulse,  $P$  is the corresponding power of the pulse and  $\tau$  is the pulse duration. The flip angle was kept constant  $\alpha = \pi/2$  and the power and time were varied step by

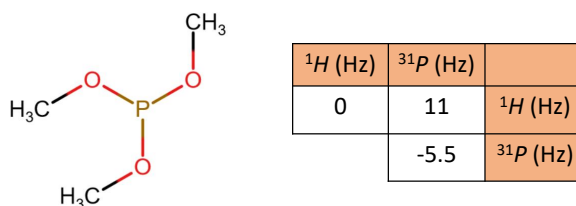


**Figure 5.4:** TMP molecule and Hamiltonian parameters.

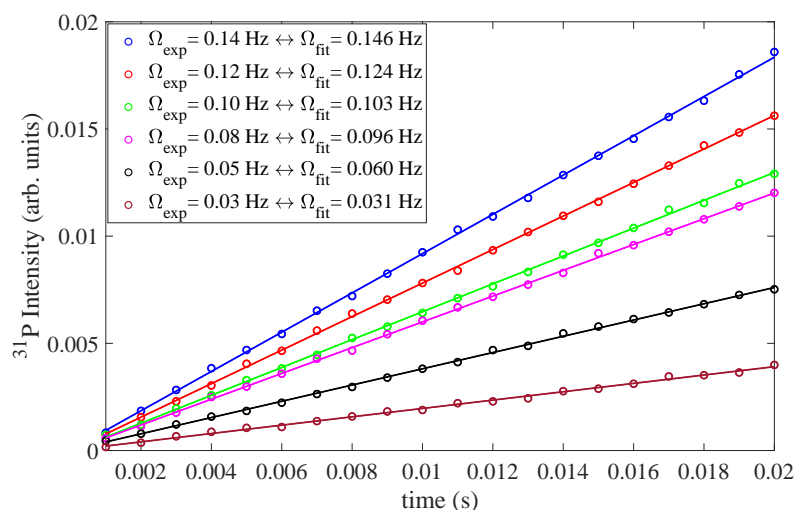


**Figure 5.5:** Low power calibration using trimethylphosphite. The intensity of <sup>31</sup>P spin after decoupling protons is shown as a function of time for various low amplitude pulses. We can see that the response is linear in this regime. The expected and exactly obtained values from back-calculation of the linear fit are shown in the legend.

step, due to the highly nonlinear response of the RF coils in the low power regime which makes direct estimation of calibration values in the low power regime error-prone. This procedure was repeated until the low power pulses of required values could be calibrated. The low power calibration was carried out for amplitudes from 0.14 Hz (which corresponded to a power of 41  $\mu\text{W}$ ) to 0.03 Hz (which corresponded to a power of 7  $\mu\text{W}$ ).

For very low amplitudes, the signal  $\propto \sin(\Omega t) \approx \Omega t$ , and therefore we expect a linear dependence. The calibration results are shown in Fig. 5.5. As we can see, the intensity of the <sup>31</sup>P spectrum after decoupling protons varies linearly with time for the low amplitude pulses. Thus by fitting a linear function to the resulting curve, we could back-calculate the exact amplitude of the pulse. The estimated and exact values from back calculation of the linear fit are shown in

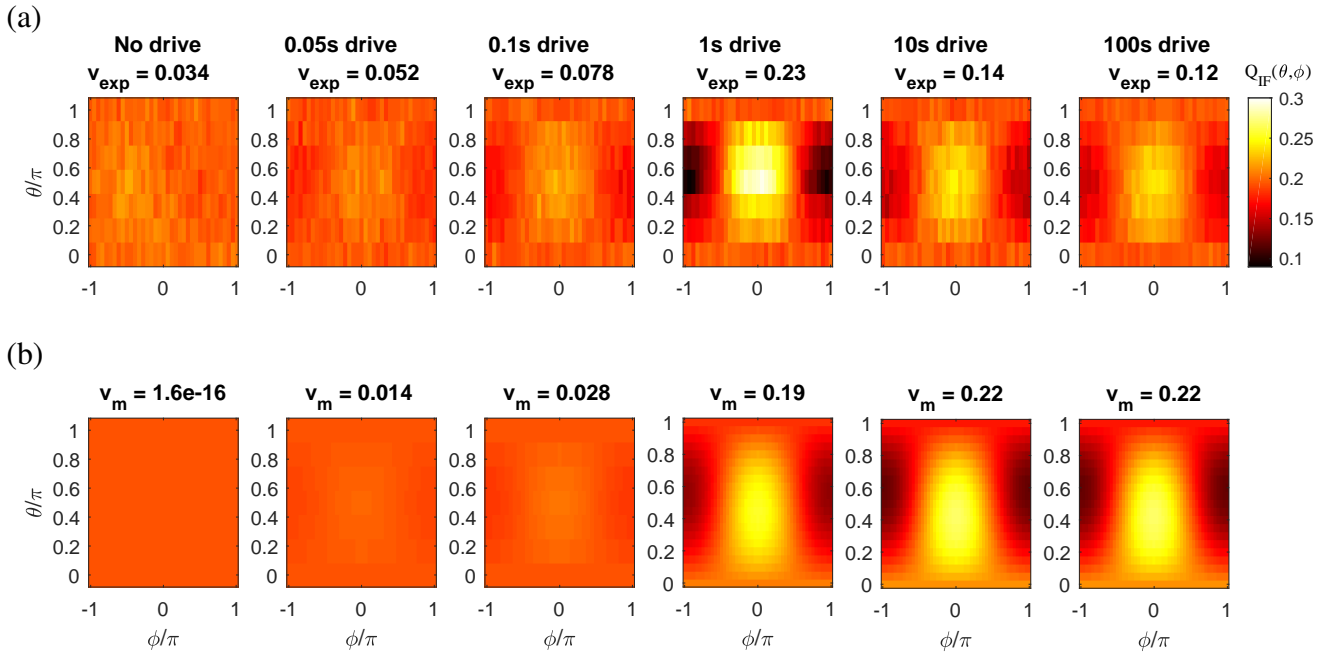


**Figure 5.6:** The full phase space Husimi distribution values for different drive durations to capture transient and steady state behaviour in the subspace of interest obtained (a) by experiments and (b) by the numerical model. The values mentioned in the titles indicate the visibility factors of the Husimi distributions. We can see that in the absence of drive, there is no localization in the phase space. Upon applying the drive, in the transient regime (upto 10 s), the phase begins to localize gradually, showing the strongest localization experimentally at a drive duration of 1 s and saturating after 10 s.

the legend. RF fields with amplitudes lesser than 0.03 Hz could not be calibrated as the power corresponding to such pulses were below the threshold of the hardware. These low power pulses were used in the Husimi distribution estimation and Arnold tongue experiments.

## 5.5.2 Synchronization experiments

The experimental IMHD results at thermal equilibrium as well as at various drive durations are shown in Fig. 5.6. The signal measured at the end of the IMHD circuit (Fig. 5.3) was directly used to estimate the Husimi distributions using Eq. (5.29). The title of each sub-figure indicates the value of the corresponding visibility factor of the Husimi distribution.

### *Limit cycle*

In the absence of drive, the system is in thermal equilibrium with the environment. Husimi distribution of the thermal equilibrium state  $\rho^{\text{eq}}$  is shown in Fig. 5.6 (a), which is uniform throughout the phase space with no phase localization, and accordingly vanishingly small visibility factor.

Therefore  $\rho^{\text{eq}}$  is a valid limit cycle with free phase, as is expected.

### *Onset of synchronization*

To study synchronization in the system, we applied a weak transition-selective drive of strength  $\Omega = 0.1$  Hz on-resonant with the  $|2\rangle \leftrightarrow |4\rangle$  transition as shown in Fig. 5.1(b). The equilibration time of the quantum system is approximately 10 s, which means that dynamics captured under 10 s can be considered transient whereas for timescales much larger than 10 s we observe steady states of the system. The drive is applied for different durations which enabled us to investigate the transient and steady state dynamics in the subspace of interest. The experimentally measured Husimi distributions for various drive durations are shown in Fig. 5.6 (a). The corresponding distributions for the instantaneous states predicted by the numerical model (described in section 5.4.2) are shown in Fig. 5.6 (b). We can see that the system gradually develops phase localization with the drive before reaching a steady state. For short drive durations, i.e., for 50 ms, 100 ms we observed a weak phase localization, which captures the transient dynamics. In this transient regime, the experimental phase distribution reached a peak localization strength at 1 s drive duration. The system then reached a steady state with the phase localization stabilizing for drive durations roughly above 10 s. It remains synchronized even up till 100 s, which is more than ten times the drive period as well as ten times the  $T_1$  relaxation time constants of the system spins.

The experimental phase localization pattern and visibility factors matched fairly well with those predicted by the numerical model. While an elaborate relaxation model, accounting for all the Lindblad dissipation operators and other experimental imperfections such as RF inhomogeneity might explain the observed deviations, the current minimal model nonetheless captured the essential signatures of synchronization.

### *Arnold tongue*

Arnold tongue is a quintessential test of synchronization that probes robustness of phase-localization against small changes in drive strengths and drive detuning [204]. As the drive strength is increased, the region of synchronization can be shown to be wider, leading to the familiar “tongue” shape. Here, we varied the drive strength of the 100 s weak drive, and its resonance-offset by 3 Hz about the resonance value. The Arnold tongue was quantified using the maximum of the synchronization measure,  $\max[S(\phi)]$ , and in this case it is only dependent on the  $\rho_{42}$  element of

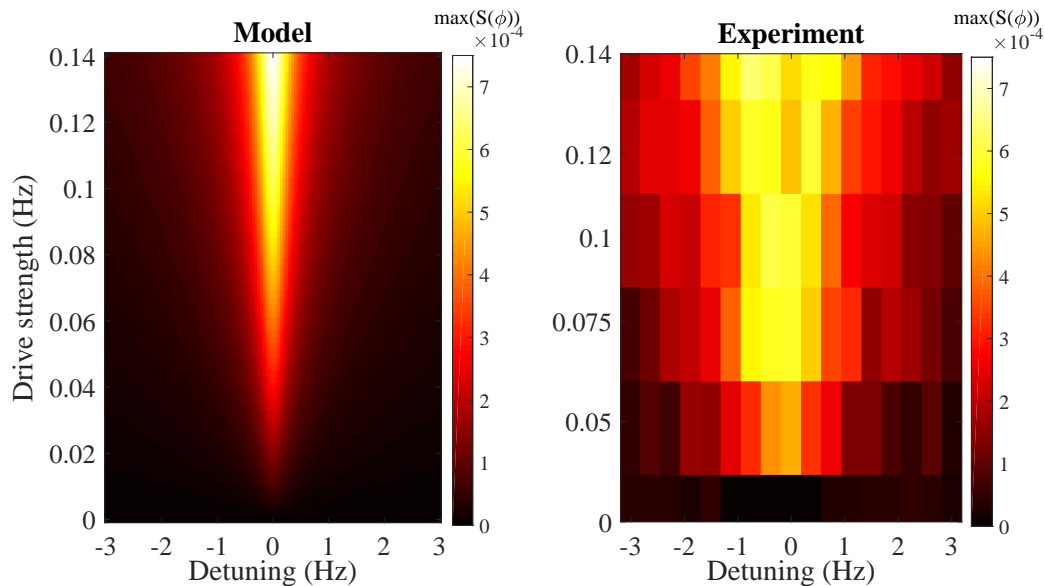


**Figure 5.7:** Arnold tongue behaviour of the system. The system shows strongest synchronization for on-resonant drive and strong drive strengths, while off-resonant drives are unable to synchronize with the transition of interest even for large driving strengths.

the density matrix, as evident from Eq. (5.12). Experimentally, this could be directly measured from the intensity of  $^{31}\text{P}$  NMR spectrum (see Fig. 5.1(e)). Fig. 5.7 compares the result of the Arnold tongue experiments with that of the numerical prediction (from the model described in section 5.4.2). For strong drive strength and near resonance conditions, the degree of synchronization was higher since the drive had more efficient perturbative effect on the system. On the other hand, for larger detuning and weaker drives, the extent of synchronization was weaker. The experimental data showed pixelation since the drive strength was varied in a discrete fashion. Moreover, in the limit of vanishing drive strength, we expect no synchronization, which could not be captured experimentally since the RF pulse calibration is reliable only till a certain lower threshold, as elaborated in Sec. 5.5.1. Despite an overall correspondence between the experimental and the predicted profiles, we could see a higher spread along the detuning axis in the experimental data, which can be attributed to the limitations of the minimal numerical model and experimental imperfections.

## 5.6 Summary and outlook

In this work, we experimentally explored the quantum equivalent of a classical omnipresent phenomenon of synchronization in nonlinear systems. We demonstrated the synchronization of a two-qubit system with a weak external drive. We used the Husimi distribution function as a witness for synchronization. A weak transition selective drive was applied on one of the spins and we observed the gradual onset of phase-localization via Husimi distribution. In the absence of any external drive, the system evolved under its internal Hamiltonian as well as inherent relaxation mechanisms, thereby settling to its thermal equilibrium state. The corresponding Husimi distribution pattern showed no phase-preference, and hence the thermal equilibrium state formed a valid limit cycle of the system.

To bypass the difficulties of performing quantum state tomography on steady states, here we used an interferometric technique to directly extract the Husimi distribution values by reading the signal of the undriven spin. This method is significantly more efficient compared to the standard tomography-based protocol.

To establish the robustness of synchronization, we investigated the response of the system to changes in drive strengths and drive detuning. The resulting phase-localization measure of the system exhibited the expected Arnold tongue behaviour. We compared the experimental results with a minimalistic  $T_1$  relaxation model of the two-qubit nuclear spin system, which could capture the general features of the experimental data.

This work demonstrated the suitability of NMR architecture for quantum synchronization studies and also opens up avenues for further exploration of the phenomenon in larger spin systems as well as under a variety of interactions and drive conditions, such as mutual synchronization in a network of spins. It would also be interesting to explore connections (if any) between quantum chaos and synchronization, since it has been established that some classically chaotic systems can synchronize [204], interplay between synchronization and quantum transport, etc.

## CHAPTER 6

---

### Simulation of interaction induced Rydberg phenomena in spin systems

---

#### Abstract

We experimentally emulate interaction induced blockade and local spin freezing in two and three qubit NMR architecture. These phenomena are identical to the Rydberg blockade and Rydberg biased freezing. In Rydberg blockade, the simultaneous excitation of two or more atoms is blocked due to the level shift induced by the strong van der Waal's interaction. In such a strong interaction regime, one can also observe Rydberg biased freezing, wherein the dynamics is confined to a subspace, with the help of multiple drives with unequal amplitudes. Here we drive NMR qubits with specific transition-selective radio waves, while intermittently characterizing the quantum states via quantum state tomography. This not only allows us to track the population dynamics, but also helps to probe quantum correlations, by means of quantum discord, evolving under blockade and freezing phenomena. Our work constitutes experimental simulations of these phenomena in the NMR platform. Moreover, these studies open up interesting quantum control perspectives in exploiting the above phenomena for entanglement generation as well as subspace manipulations.

#### Reported in

**V. R. Krithika**, Soham Pal, Rejish Nath, and T. S. Mahesh, *Observation of interaction induced blockade and local spin freezing in a NMR quantum simulator*, [Phys. Rev. Research](#) **3**, 033035 (2021).

## 6.1 Introduction

In this work, we explore some very different effects of interactions in giving rise to novel phenomena, such as blockade and freezing, in quantum systems. The blockade phenomenon is one in which strong interaction between systems shifts the energy of multi-excited states, and hence prohibit their simultaneous excitation of many particles by a drive field. It has been a subject of intense study using various quantum systems. For instance, blockade has been observed in electrons [254–256], photons [257–261], ions [262], and Rydberg atoms [263–265]. The blockade effect has been used for applications in controlled preparation of quantum states [266, 267], in particular the entangled or nonclassical states [268–270], thus becoming highly relevant for quantum information applications [271, 272] and quantum many-body physics [273]. It is well known that preparing entangled states in many-particle systems is no trivial task. The blockade phenomenon offers a convenient method to prepare such entangled states and can be scaled with the system size. In Rydberg systems, strong coupling between atoms arises as a consequence of strong van der Waals interaction between the atoms [272]. In the Rydberg blockade regime, a new feature has been predicted recently by Vineesha et al. [274], called the Rydberg biased freezing. In this phenomenon, the dynamics of atoms driven with small Rabi coupling freeze. The phenomenon of biased freezing can provide local control on selected qubits in a multi-qubit system, which is of vital importance in many quantum computing and information processing tasks [275].

Quantum simulations are a cornerstone of quantum computing and information processing tasks. Since their conception in the early 1980s, quantum simulators have steadily expanded to encompass several architectures and capabilities [10, 276, 277]. These simulators help us harness the powerful resources of quantum systems, such as superpositions and entanglement, which are beyond the reach of current day classical simulators. Among the many platforms that are today available, spin-based architectures such as NMR and vacancy centres in diamond are some of the most versatile, owing to the precise control, long coherence times, wide variety of spin-qubit topologies, and well developed methodologies. They have been routinely used to simulate various quantum phenomena from atomic to condensed matter physics [278–282]. Hence, given the importance of spin-based quantum information and computing platforms, it is of timely interest

to emulate blockade and Rydberg biased freezing in spin systems. Here, we use NMR as the experimental demonstration platform.

## 6.2 Objective

In this chapter, we experimentally demonstrate interaction induced blockade and local spin freezing, identical to the Rydberg blockade and Rydberg biased freezing phenomena respectively using two- and three-qubit spin systems in NMR architecture. We first establish the mapping of Rydberg blockade and freezing dynamics to NMR spin Hamiltonian to emulate the required dynamics. Subsequently, we study the following

- (i) Rabi oscillation dynamics of the spin systems under a radio-frequency (RF) field in the absence of interactions.
- (ii) Next, we introduce spin-spin couplings in the system and study the modified dynamics, i.e., blockade and local spin freezing, in the systems as compared to the non-interacting case. We also realize various configurations of Rydberg-biased freezing in the multi-qubit systems.
- (iii) We carry out full quantum state tomography at different instants to monitor the state and to extract quantum correlations in the system via quantum discord, as they evolve.
- (iv) We show that local freezing is not a adhoc occurrence at some RF drive amplitudes, but can be realized by the gradual tuning of parameters from blockade conditions.

Operational maps between atoms and spins, such as the ones used here are of interest since they might open up new possibilities in experimental quantum simulations using NMR architecture. Such maps not only provide clues towards new phenomena not foreseen by either of the quantum architectures, but also help conceive hybrid architectures.

## 6.3 Rydberg blockade and Rydberg biased freezing

In this section, we briefly review the phenomena of the Rydberg blockade and Rydberg biased freezing for two atoms ( $N = 2$ ). Each atom comprises of two levels with the ground state  $\{|g\rangle\}$  coupled to the Rydberg state  $\{|e\rangle\}$  by a laser field of Rabi frequency  $\Omega_i$  and detuning  $\Delta_i$ . In the

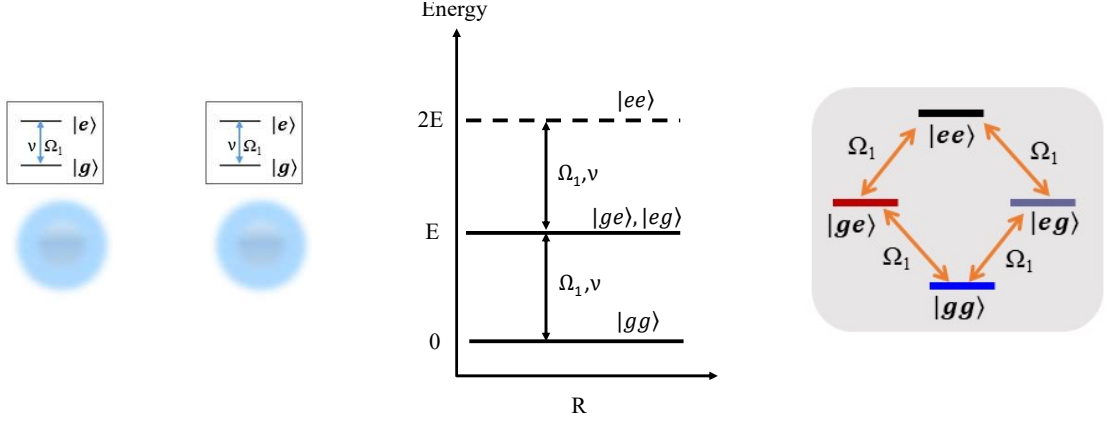


**Figure 6.1:** A system of two uncoupled Rydberg atoms and their corresponding energy level diagram with  $\nu$  denoting frequency of the energy gap. The ground state of each atom is coupled to the excited state by laser fields with Rabi frequencies  $\Omega_1$  and  $\Omega_2 = \Omega_1$  respectively. The energy levels of the system are equally separated in energy. Hence populations periodically oscillate between the ground state  $\{|gg\rangle\}$  and the doubly excited state  $\{|ee\rangle\}$  via the intermediate singly excited states  $\{|ge\rangle, |eg\rangle\}$ .

frozen-gas limit, the system is described by the Hamiltonian

$$\hat{H} = - \sum_{i=1}^2 \Delta_i \hat{\sigma}_{ee}^i + \sum_{i=1}^2 \Omega_i \hat{\sigma}_x^i + V_0 \hat{\sigma}_{ee}^1 \hat{\sigma}_{ee}^2, \quad (6.1)$$

where  $\hat{\sigma}_{ab} = |a\rangle\langle b|$  with  $a, b \in \{g, e\}$ ,  $\hat{\sigma}_x^i = \hat{\sigma}_{eg}^i + \hat{\sigma}_{ge}^i$ . Here, the value of  $\hbar$  has been set to 1. The interaction potential between two Rydberg excitations separated by a distance  $R$  is given by the van der Waals interaction  $V_0 = C_6/R^6$  where  $C_6$  is the van der Waals coefficient [272]. Henceforth, we take  $\Delta_i = 0$ , and work in the basis  $\{|gg\rangle, |ge\rangle, |eg\rangle, |ee\rangle\}$ .

In the case of uncoupled Rydberg atoms, i.e.,  $V_0 = 0$ , the ground state ( $|gg\rangle$ ), first excited state ( $|ge\rangle, |eg\rangle$ ) and doubly excited states ( $|ee\rangle$ ) are equally separated in energy as shown in Fig. 6.1. When an oscillatory excitation field of Rabi frequency  $\Omega_1$  is applied to such a system, the atoms get excited from the ground state to the doubly excited state via the intermediate singly-excited state, which manifests as Rabi oscillations of the populations within these levels.

### 6.3.1 Rydberg blockade

To observe Rydberg blockade, we move to the regime  $V_0 \gg \{\Omega_1, \Omega_2\}$ , and assume that  $\Omega_1 = \Omega_2$ . Under such conditions, the doubly excited state experiences a large energy shift due to  $V_0$  [see Fig. 6.2(a)], and gets detuned from the excitation field. In this case, if the two atoms are ini-

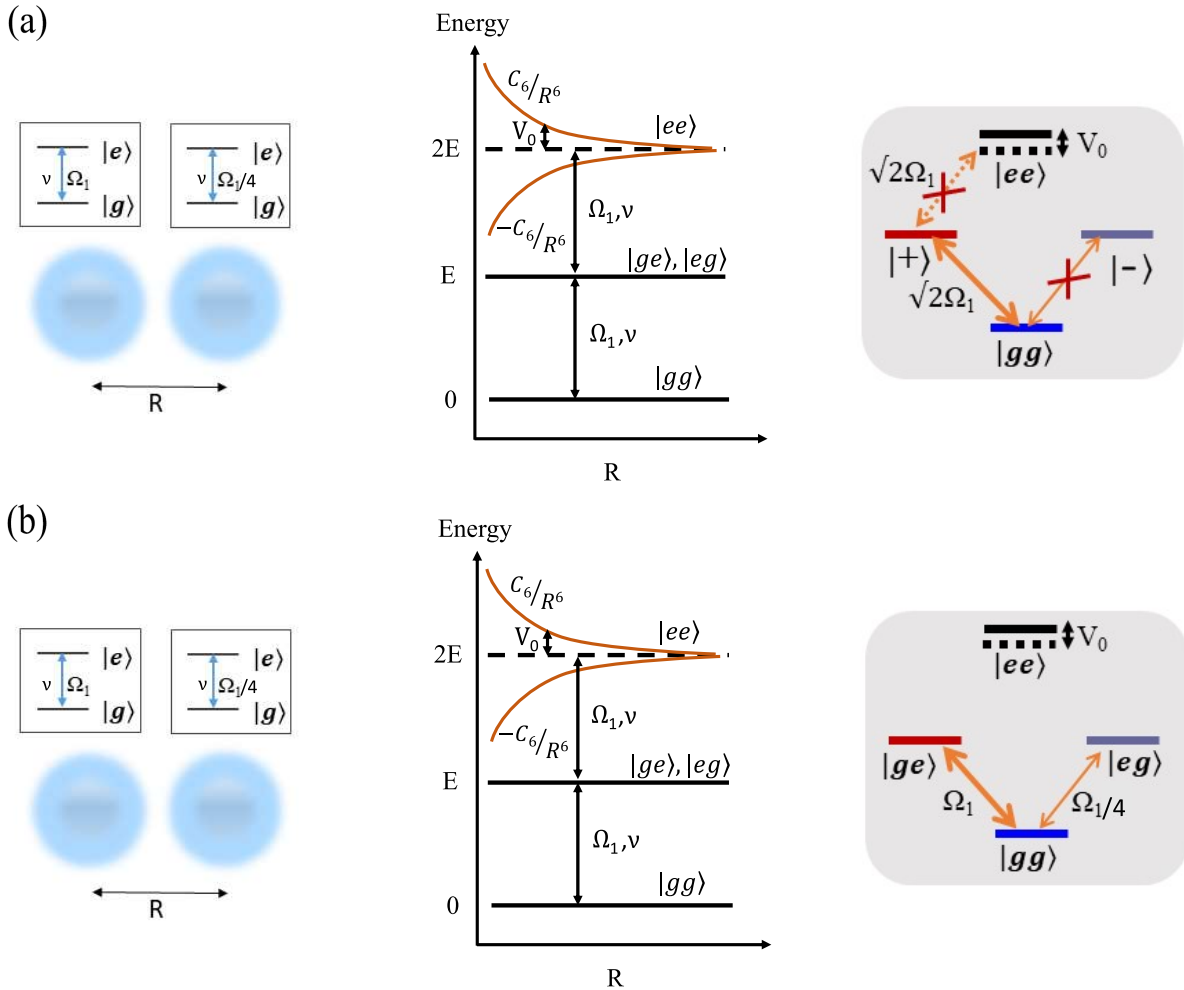


**Figure 6.2:** The energy level diagram and allowed transitions under (a) blockade and (b) Rydberg biased freezing of two interacting Rydberg atoms. Here,  $\nu$  denotes the frequency of the energy gap. The ground state of each atom is coupled to the excited state by laser fields with Rabi frequencies  $\Omega_1$  and  $\Omega_2$  respectively. Under strong interaction, the doubly excited state shifts out of resonance. In the regime  $\Omega_1 = \Omega_2$  (a), the system exhibits dynamics between the ground state  $|gg\rangle$  and the entangled state  $|+\rangle = (|eg\rangle + |ge\rangle)/\sqrt{2}$  with enhanced frequency  $\sqrt{2}\Omega_1$ . The entangled state  $|-\rangle = (|eg\rangle - |ge\rangle)/\sqrt{2}$  is also cut-off from the system's dynamics. In the regime where second atom is driven by a much weaker drive than the first atom  $\Omega_2 = \Omega_1/4$  (b), the dynamics of the second atom is suppressed and that of the first atom is unhindered, resulting in freezing of the second atom.

tialised in  $|gg\rangle$ , they exhibit coherent Rabi oscillations between  $|gg\rangle$  and  $|+\rangle = (|ge\rangle + |eg\rangle)/\sqrt{2}$  with an enhanced Rabi-frequency of  $\sqrt{2}\Omega_1$ , cutting off  $|ee\rangle$  entirely from the population dynamics. Effectively, strong interactions hinder the presence of two excitations simultaneously, over a separation of  $R_b$ , the blockade radius. This phenomenon is called Rydberg blockade [263–265].

### 6.3.2 Rydberg biased freezing

Next, keeping  $V_0 \gg \{\Omega_1, \Omega_2\}$  such that we remain in the blockade regime, if we increase  $\Omega_2$ , it eventually freezes the dynamics of the first atom [see Fig. 6.2(b)]. This phenomenon was first shown by Vineesha et.al [274] and is termed as Rydberg biased freezing. Note that the Rydberg biased freezing emerges as a combined effect of *both strong interactions and the strong driving on one atom* [274]. Since the system is still in blockade regime,  $|ee\rangle$  is cut off from the dynamics. Further, due to the strong bias on the second atom, the system exhibits predominant coherent Rabi oscillations between  $|gg\rangle$  and  $|ge\rangle$ , freezing the first atom.

It is straightforward to extend both blockade and freezing phenomena for more than two atoms. For  $N$  atoms and  $\Delta_i = 0$ , the Hamiltonian in Eq. (6.1) can be extended as,

$$\hat{H} = \sum_{i=1}^N \Omega_i \hat{\sigma}_x^i + \sum_{i<j}^N V_{ij} \hat{\sigma}_{ee}^i \hat{\sigma}_{ee}^j, \quad (6.2)$$

where  $V_{ij} = C_6/r_{ij}^6$  and  $r_{ij}$  is the separation between  $i$ th and  $j$ th atoms. A fully blockaded sample of  $N$  two level atoms exhibit coherent Rabi oscillations between the many-body ground state  $|G\rangle = \otimes_{i=1}^N |g^{(i)}\rangle$  and a collective single excited state,  $|+N\rangle = \sum_i |gg\dots e^{(i)}\dots gg\rangle/\sqrt{N}$  [283]. Freezing one or more atoms in an  $N$ -atom system can also be realized by appropriately tuning the Rabi frequencies on selected atoms. In this case, the system exhibits coherent Rabi oscillations between  $|G\rangle$  and the corresponding product states.

### 6.3.3 Mapping Rydberg atom Hamiltonian to spins

In this section, we describe the spin-model corresponding to the Rydberg atom Hamiltonian used to describe blockade and Rydberg biased freezing. We introduce the spin-1/2 operators,  $\hat{I}_\alpha^i$  ( $\alpha \in \{x, y, z\}$ ) by mapping  $|g\rangle$  and  $|e\rangle$  with up ( $|\uparrow\rangle$ ) and down ( $|\downarrow\rangle$ ) spin states along the  $z$ -axis, respectively. Then, we have  $\hat{\sigma}_x^i = 2\hat{I}_x^i$ , and  $\hat{\sigma}_{ee}^i = (\mathbb{1} - 2\hat{I}_z^i)/2$ , where  $\mathbb{1}$  is the identity operator,

and the Hamiltonian in Eq. (6.2) reads as (apart from an identity term),

$$\begin{aligned}
\hat{H} &= 2 \sum_{i=1}^N \Omega_i \hat{I}_x^i + \frac{1}{4} \sum_{i<j}^N V_{ij} (\mathbb{1} - 2\hat{I}_z^i) (\mathbb{1} - 2\hat{I}_z^j) \\
&= 2 \sum_{i=1}^N \Omega_i \hat{I}_x^i - \frac{1}{2} \sum_{i<j}^N V_{ij} (\hat{I}_z^i + \hat{I}_z^j) + \sum_{i<j}^N V_{ij} \hat{I}_z^i \hat{I}_z^j.
\end{aligned} \tag{6.3}$$

Since  $V_{ii} = 0$  and  $V_{ij} = V_{ji}$ , the second term in the above equation can be further simplified as follows

$$\begin{aligned}
-\frac{1}{2} \sum_{i<j}^N V_{ij} (\hat{I}_z^i + \hat{I}_z^j) &= -\frac{1}{2} \sum_{i=1}^N \sum_{j=1}^N \frac{V_{ij}}{2} \hat{I}_z^i + \frac{V_{ji}}{2} \hat{I}_z^j \\
&= -\frac{1}{2} \sum_{i=1}^N \bar{V}_i \hat{I}_z^i - \frac{1}{2} \sum_{j=1}^N \bar{V}_j \hat{I}_z^j = -\sum_{i=1}^N \bar{V}_i \hat{I}_z^i,
\end{aligned} \tag{6.4}$$

where  $\bar{V}_i = \sum_{j=1}^N V_{ij}/2$ . Thus, the overall Hamiltonian can be cast in terms of spin operators as

$$H = 2 \sum_{i=1}^N \Omega_i \hat{I}_x^i - \sum_{i=1}^N \bar{V}_i \hat{I}_z^i + \sum_{i<j}^N V_{ij} \hat{I}_z^i \hat{I}_z^j. \tag{6.5}$$

In spin models, the first term in Eq. (6.5) plays the role of a transverse field, second term acts as a longitudinal field and the third term provides the Ising interactions. In the next section, we describe the experimental realization of the above Hamiltonian using nuclear spins. For our convenience, we continue to use the states  $|g\rangle$  and  $|e\rangle$  as the two spin states of the NMR qubit.

## 6.4 Experimental setup and results

We experimentally emulated Rydberg atom dynamics on two different systems: (i) a two-qubit system involving  $^{19}\text{F}$  and  $^{31}\text{P}$  nuclear spins of sodium fluorophosphate dissolved in  $\text{D}_2\text{O}$  (Fig. 6.3(a)), and (ii) a three-qubit system involving  $^1\text{H}$ ,  $^{13}\text{C}$  and  $^{19}\text{F}$  nuclear spins of dibromofluoromethane, (Fig. 6.3(d)) dissolved in deuterated acetone. All experiments were performed on a 500 MHz high-resolution Bruker NMR spectrometer at ambient temperatures.

Each NMR sample contains about  $10^{15}$  molecules (nuclear spin-systems) placed in an external

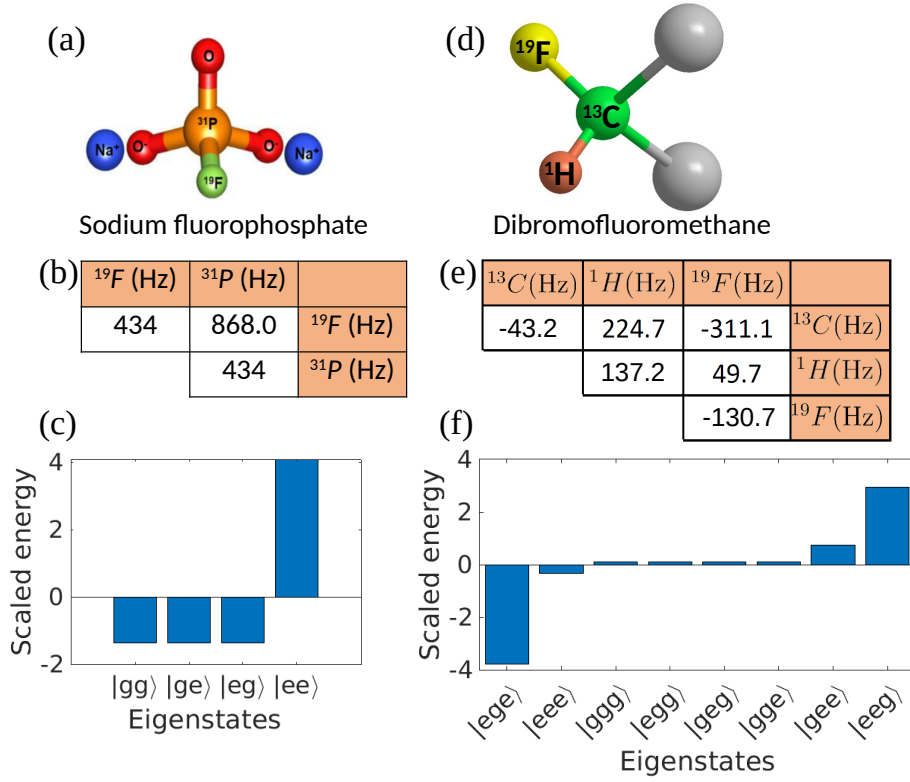


**Figure 6.3:** Sodium fluorophosphate molecule (a), the parameters of the rotating-frame Hamiltonian  $H_0$  (Eq. 6.6) (b) forming the two-qubit register, and the corresponding energy eigenstates and eigenvalues (c). Dibromofluoromethane molecule (d), the parameters of rotating-frame Hamiltonian (e) forming the three-qubit register, and the corresponding energy eigenstates and eigenvalues (f). In tables (b, e) the diagonal elements represent tunable off-set frequencies  $\nu_i$  set according to Eq. 6.7, and off-diagonal elements show scalar coupling constants  $\mathcal{J}_{ij}$  between the respective qubits.

magnetic field  $\mathbf{B} = B_0 \hat{z}$ , where  $B_0 = 11.75$  T. The Zeeman interaction lifts the degeneracy between the spin states  $m = \pm 1/2$  with an energy gap  $\hbar \gamma_i B_0$  where  $\gamma_i$  is the gyromagnetic ratio of the nuclear isotope and  $\gamma_i B_0$  constitutes its Larmor frequency. The time-averaged local field at the site of nuclear spins in a rapidly reorienting liquid molecule differs from the external magnetic field. The resulting individual Larmor frequencies  $\gamma_i B_0 (1 + \delta_i)$  are strongly dependent on the chemical environment.

Each of the nuclear isotopes forming our spin systems were irradiated with a linearly polarized radio-frequency (RF) wave, whose resonant component is of the form  $B_i^{\text{RF}} \exp(i2\pi\eta_i t)$  characterized by controllable amplitudes  $2\pi\nu_i^{\text{RF}} = \gamma_i B_i^{\text{RF}}$  and controllable carrier frequencies  $\eta_i$ . The resonance offsets with respect to the carrier frequencies are given by  $2\pi\nu_i = \gamma_i B_0 (1 + \delta_i) - 2\pi\eta_i$ . The spins also interact with one another via a constant scalar coupling  $\mathcal{J}_{ij}$  mediated through covalent bonds. While  $\mathcal{J}_{ij}$  itself is not a controllable parameter, the effective evolution time of the

scalar interaction, can however be manipulated, if required. For both the spin systems described above, the resonance offsets and coupling strengths are tabulated in Fig. 6.3(b,e).

Thus the NMR Hamiltonian in a frame co-rotating with individual RF carriers for a heteronuclear system under secular approximation is

$$\begin{aligned}
 H_{\text{NMR}} &= 2\pi \sum_{i=1}^N \nu_i^{\text{RF}} \hat{I}_x^i + H_0, \quad \text{where,} \\
 H_0 &= -2\pi \sum_{i=1}^N \nu_i \hat{I}_z^i + 2\pi \sum_{i,j>i}^N \mathcal{J}_{ij} \hat{I}_z^i \hat{I}_z^j.
 \end{aligned} \tag{6.6}$$

We can now map the NMR parameters in Eq. 6.6 with the Rydberg system in Eq. 6.5 by setting

$$2\pi\nu_i^{\text{RF}} = 2\Omega_i, \quad 2\pi\nu_i = \bar{V}_i, \quad \text{and} \quad 2\pi\mathcal{J}_{ij} = V_{ij}. \tag{6.7}$$

The energy eigenstates and corresponding eigenvalues of the two and three-qubit systems for the rotating-frame Hamiltonian  $H_0$  in Eq. 6.6 are shown in Fig. 6.3(c, f) respectively. Thus, NMR systems along with RF pulses provide a natural test bed for emulating similar physics that can be studied using a Rydberg quantum simulator.

### 6.4.1 Capturing single spin-1/2 dynamics in a multi-qubit system

Here, we explain how we realized the dynamics of non interacting spins (equivalent to  $V_0 = 0$ ) in the two and three-qubit cases. The Rabi oscillation of a non interacting spin-1/2 nucleus can be realized in different ways. For instance, one can use heteronuclear spin-decoupling to average-out all the spin-spin interactions [49]. However, here we used a simpler method that uses low-bandwidth transition-selective RF fields whose carrier frequencies are set on one of the transitions of each spin and ignore all other off-resonant transitions. In the weak coupling approximation, the Rabi dynamics on individual on-resonant transitions is equivalent to a non interacting two-level system. To realize a single spin dynamics of spin A in a coupled spin pair AB, we first let spin B

remain in the thermal state  $\rho_B = \frac{1}{2}|\uparrow\rangle\langle\uparrow| - \frac{1}{2}|\downarrow\rangle\langle\downarrow|$ , so that the spins are in a separable initial state

$$\begin{aligned}\rho_{AB} &= \rho_A \otimes \rho_B \\ &= \frac{1}{2}\rho_A \otimes |\uparrow\rangle\langle\uparrow| - \frac{1}{2}\rho_A \otimes |\downarrow\rangle\langle\downarrow|.\end{aligned}\quad (6.8)$$

As illustrated in Fig. 6.4, the four-dimensional space can now be decomposed into two single-spin subspaces labeled  $B_\uparrow$  and  $B_\downarrow$  based on the state of spin-B. The subspaces remain independent as long as spin B is undisturbed.

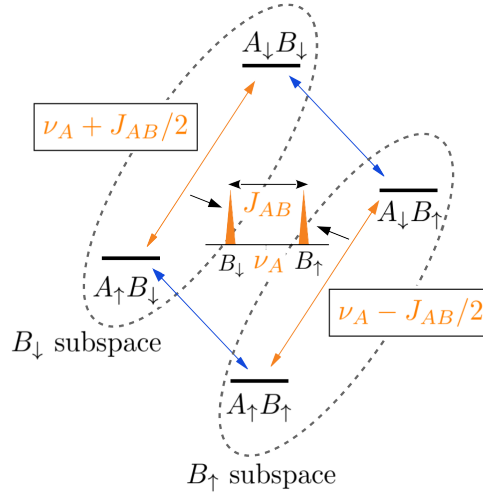


**Figure 6.4:** Energy levels of a coupled two-qubit system AB. The dashed ellipses show the  $B_\uparrow$  and  $B_\downarrow$  subspaces. The two transitions of qubit A are displayed at the center with the corresponding spin orientation of qubit B labeled under each peak.

Now consider a propagator  $U_A = U_\uparrow \otimes |\uparrow\rangle\langle\uparrow| + U_\downarrow \otimes |\downarrow\rangle\langle\downarrow|$ , which is essentially acting on spin-A subspaces

$$\rho_{AB} \xrightarrow{U_A} \rho'_{AB} = (U_\uparrow \rho_A U_\uparrow^\dagger) \otimes |\uparrow\rangle\langle\uparrow| + (U_\downarrow \rho_A U_\downarrow^\dagger) \otimes |\downarrow\rangle\langle\downarrow|.\quad (6.9)$$

The two resolved spectral lines of spin-A allow individual measurements of the two subspaces, i.e., the expectation values in the two subspaces are identical to that of a pair of uncoupled

single spins:

$$\begin{aligned} s_{\uparrow} &= \text{Tr}[(\sigma_x \otimes |\uparrow\rangle\langle\uparrow|)\rho'_{AB}] = \text{Tr}[\sigma_x(U_{\uparrow}\rho_A U_{\uparrow}^{\dagger})] \quad \text{and,} \\ s_{\downarrow} &= \text{Tr}[(\sigma_x \otimes |\downarrow\rangle\langle\downarrow|)\rho'_{AB}] = \text{Tr}[\sigma_x(U_{\downarrow}\rho_A U_{\downarrow}^{\dagger})]. \end{aligned} \quad (6.10)$$

Note that the above expectations are as if  $U_{\uparrow}$  or  $U_{\downarrow}$  is applied on a single uncoupled spin. The above method can be easily generalized to multi-spin systems. In our experiment, we choose  $\uparrow$ -subspace in 2-spin case and  $\uparrow\uparrow$ -subspace in 3-spin case to study the single-spin Rabi dynamics of each nuclear spin. We take the data only from the transition of interest and ignore all other peaks in the spectrum, thereby capturing the uncoupled dynamics. We repeat this procedure for the individual spins in the system and then combine the results to get the overall dynamics of the non interacting spins. In the following sections, we explain the experimental setup for interacting spin architecture to emulate Rydberg blockade and freezing dynamics.

## 6.4.2 Initialization, Readout, and Modeling Experimental Imperfections

### Initialization

As explained in Sec. 1.2.1.4, at ambient temperatures, the thermal energy is much larger than the Zeeman energy gaps and accordingly an  $n$ -qubit NMR system is found in a highly mixed state of the form  $\rho_{\text{th}} = \mathbb{1}/2^n + \sum_i \epsilon_i \hat{I}_z^i$ , where  $\mathbb{1}$  accounts for the uniform background population and  $\epsilon_i = \hbar\gamma_i B_0 / (2^n k_B T) \sim 10^{-5}$  is the purity factor capturing the deviation population distribution. Therefore, one prepares a *pseudopure state* (PPS) [6] of the form  $\rho_{\text{pps}} = (1 - \epsilon)\mathbb{1}/2^n + \epsilon|\psi\rangle\langle\psi|$  using spatial averaging technique, which captures the essential dynamics of a pure state  $|\psi\rangle$ . The NMR pulse sequences for preparing two- and three-qubit PPS states are shown in Fig. 1.5.

### Readout

We performed full Quantum State Tomography (QST) to determine the instantaneous state during evolution, which allowed us not only to monitor populations in various energy levels, but also to quantify coherences and thereby extract quantum correlations. Since NMR signals arise from single-transition transverse-magnetization operators of the form  $I_x^i \pm iI_y^i$ , not all elements of the density matrix are directly measurable. Therefore, one performs a set of experiments to system-

atically convert unobservable elements to observable elements of the density matrix, followed by their measurements [251]. In our case, we performed six and twelve such detection experiments for two and three qubit registers respectively, to obtain pure phase absorptive signals [155], using which we reconstructed the full density matrix.

### Modeling experimental imperfections

The two main imperfections in the NMR experiments are (i) spatial RF inhomogeneity (RFI) causing different Rabi amplitudes at different points in the sample and (ii) z-repolarization process  $T_1$  (relaxation to thermal equilibrium) and dephasing process  $T_2$  (loss of quantum coherence) [49]. The rate constants  $T_1$  and  $T_2$  are measured by standard NMR methods. We modelled RFI by considering a probability distribution of RF values spread over  $\pm 10\%$  about the nominal value. This distribution was then optimized by minimizing the rms deviation of the experimental data points from the corresponding theoretical values. Decoherence effects were also incorporated into the same model. The theoretical points were obtained by solving the von Neumann equation in the rotating frame using Eq. (6.6) for the corresponding initial state density matrix in each case.

## 6.5 Results and Discussion

### 6.5.1 Non-interacting spins ( $\mathcal{J}_{ij} = 0$ )

We first studied the Rabi oscillations of non interacting ( $\mathcal{J}_{ij} = 0$ ) spins under a uniform drive, i.e.,  $\nu_i^{\text{RF}} = \nu^{\text{RF}}$  for all  $i$ . The Zeeman energy splitting provides the necessary levels for Rabi oscillations, as illustrated in the central columns of Fig. 6.5 and Fig. 6.6. As explained before in Sec. 6.4.1, after initializing each spin to its ground state, we applied RF fields to drive the on-resonant transitions with field amplitudes  $\nu^{\text{RF}} = 217$  Hz and  $\nu^{\text{RF}} = 10$  Hz respectively for the two and three-qubit registers. The relative populations of ground and excited states were then measured by a suitable detection pulse after dephasing (and hence destroying) the coherences with the help of a pulsed field gradient (PFG).

The dynamics for the non interacting spins in the two-qubit and three-qubit systems, are shown in Figs. 6.5(a) and 6.6(a), respectively. Since the drive was applied to all the spins simul-

taneously, it leads to coherent Rabi oscillations between the ground states  $|gg\rangle$  or  $|ggg\rangle$  with the excited states  $|ee\rangle$  or  $|eee\rangle$  respectively. The decay profiles indicated by the experimental data points relative to the theoretical expectations (dashed-lines) are due to environmental relaxations in NMR systems as well as RFI. These effects were captured fairly well by the model indicated by the solid lines. In two-qubit register, the population transfer from  $|gg\rangle$  to  $|ee\rangle$  takes place via single excited states  $|eg\rangle$  and  $|ge\rangle$  and for  $N = 3$  we have both singly and doubly excited states as intermediate ones as shown in Fig. 6.6(a).

### 6.5.2 Strongly interacting case: Interaction induced excitation blockade

Next, we considered the case of strongly interacting spins with  $\mathcal{J}_{ij} \gg \nu^{\text{RF}}$  and  $\nu_i \gg \nu^{\text{RF}}$ . For the two-qubit register, we have  $\mathcal{J}_{ij} = 868$  Hz, and  $\nu^{\text{RF}} = 217$  Hz.

We first prepared  $|G\rangle = |gg\rangle$  pseudopure state as explained in Sec. 6.4.2. Following the basis-freedom in the degenerate subspace, singly-excited states  $|ge\rangle$  and  $|eg\rangle$  can be linearly combined to form  $|\pm\rangle = (|ge\rangle \pm |eg\rangle)/\sqrt{2}$ . Under these conditions, we observed Rabi oscillations between  $|gg\rangle$  and  $|+\rangle = (|ge\rangle + |eg\rangle)/\sqrt{2}$ , with no population being found in  $|ee\rangle$ , indicating the excitation blockade. This effect is shown in Fig. 6.5(c). Note that, the anti-symmetric state  $|-\rangle = (|ge\rangle - |eg\rangle)/\sqrt{2}$  is completely decoupled from the excitation dynamics. Comparing this to the results for the non interacting qubits [Fig. 6.5(a)], the oscillation frequency of the population in  $|gg\rangle$  was amplified by a factor of  $\sqrt{2}$  due to the blockade. Experimentally, we observed an oscillation frequency of  $(\sqrt{2} \pm 0.002)\nu^{\text{RF}}$ , showing an excellent agreement with the expected theoretical prediction.

In the three-qubit case [see Fig. 6.6(c)], we have  $\nu^{\text{RF}} = 10$  Hz, and the interaction strengths are given in Fig. 6.3(d). We then prepared  $|G\rangle = |ggg\rangle$  pseudopure state as described in Sec. 6.4.2. Again following the basis-freedom in the degenerate subspace, singly-excited states  $|egg\rangle$ ,  $|geg\rangle$ , and  $|gge\rangle$ , are linearly combined to form  $|W_1\rangle \equiv |+_3\rangle = (|001\rangle + |010\rangle + |100\rangle)/\sqrt{3}$  and its orthogonal counterparts  $|W_2\rangle$  and  $|W_3\rangle$ , which can be determined by Gram-Schmidt orthogonalization. The basis is not uniquely fixed, but a possible combination is  $|W_2\rangle = (2|001\rangle - |010\rangle - |100\rangle)/\sqrt{6}$  and  $|W_3\rangle = (|010\rangle - |100\rangle)/\sqrt{2}$ . The spin-spin interactions are such that the states with more than one excitation are energetically well separated from  $|G\rangle$  and singly excited states. The experimental and theoretical results of the population dynamics shown in Fig. 6.6(c)

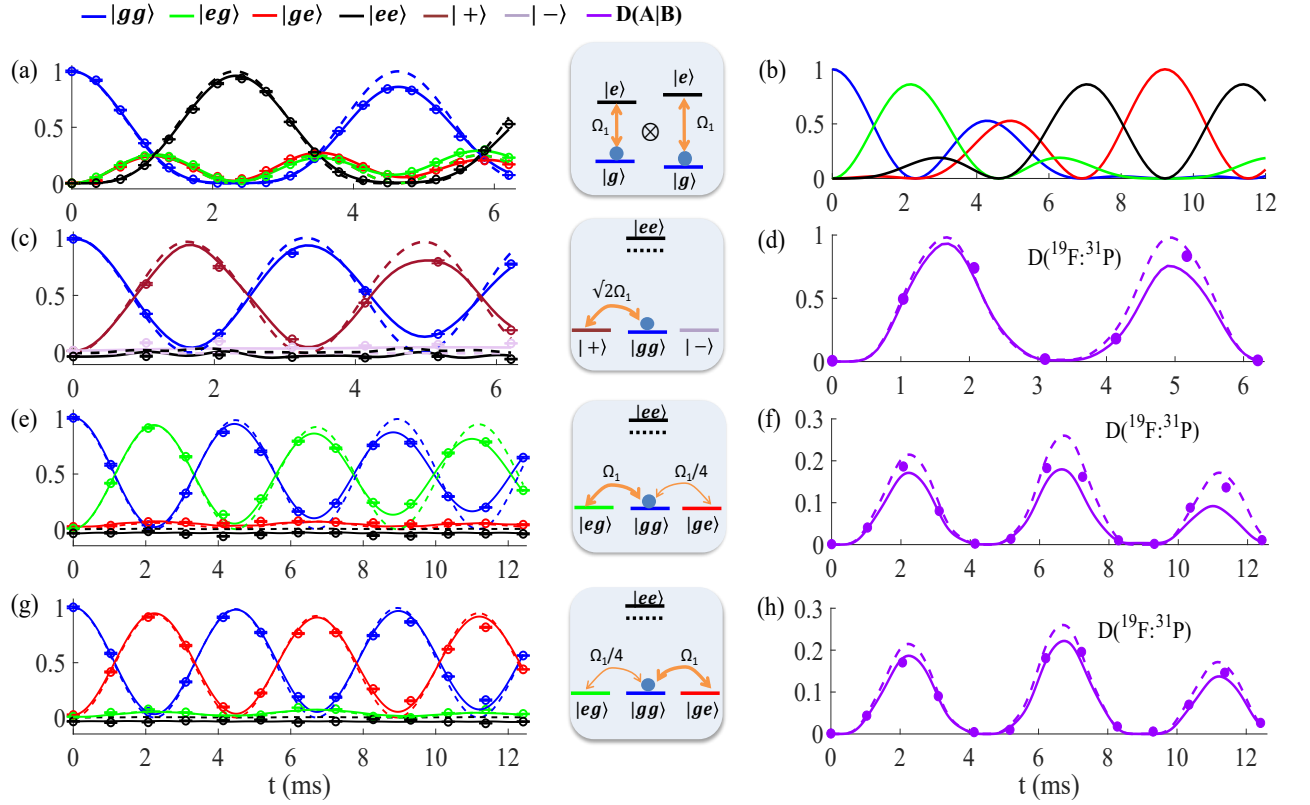


**Figure 6.5:** Population dynamics (left column) and discord (right column) versus driving time for the two-qubit register under Rabi drive (a), interaction induced blockade (c,d), freezing of the second qubit (e,f) and of the first qubit (g,h). Plot (b) shows the population dynamics of a pair of non interacting spins with the same driving parameters as in freezing on second qubit case (g), illustrating the importance of spin-spin interaction to realize freezing. Experimental data points are shown by dots with error bars (indicating random errors), theoretically expected dynamics are shown by dashed lines, and realistic numerical models are shown by solid lines. In each case, the corresponding energy level diagram is also shown (central column) with the same color coding as the legend shown at the top of the figure. The energy level diagram of (a) corresponds to uncoupled spins, while those of (c)-(g) show eigenstates of the rotating frame Hamiltonian ( $H_0$ ) in a relevant basis (upto the freedom in degenerate subspace) along with prominent transitions. The discord values  $D(A|B)$  are expressed in units of  $\ln 2/\epsilon^2$  [46], where  $\epsilon$  is the purity factor as described in section 6.4.2.

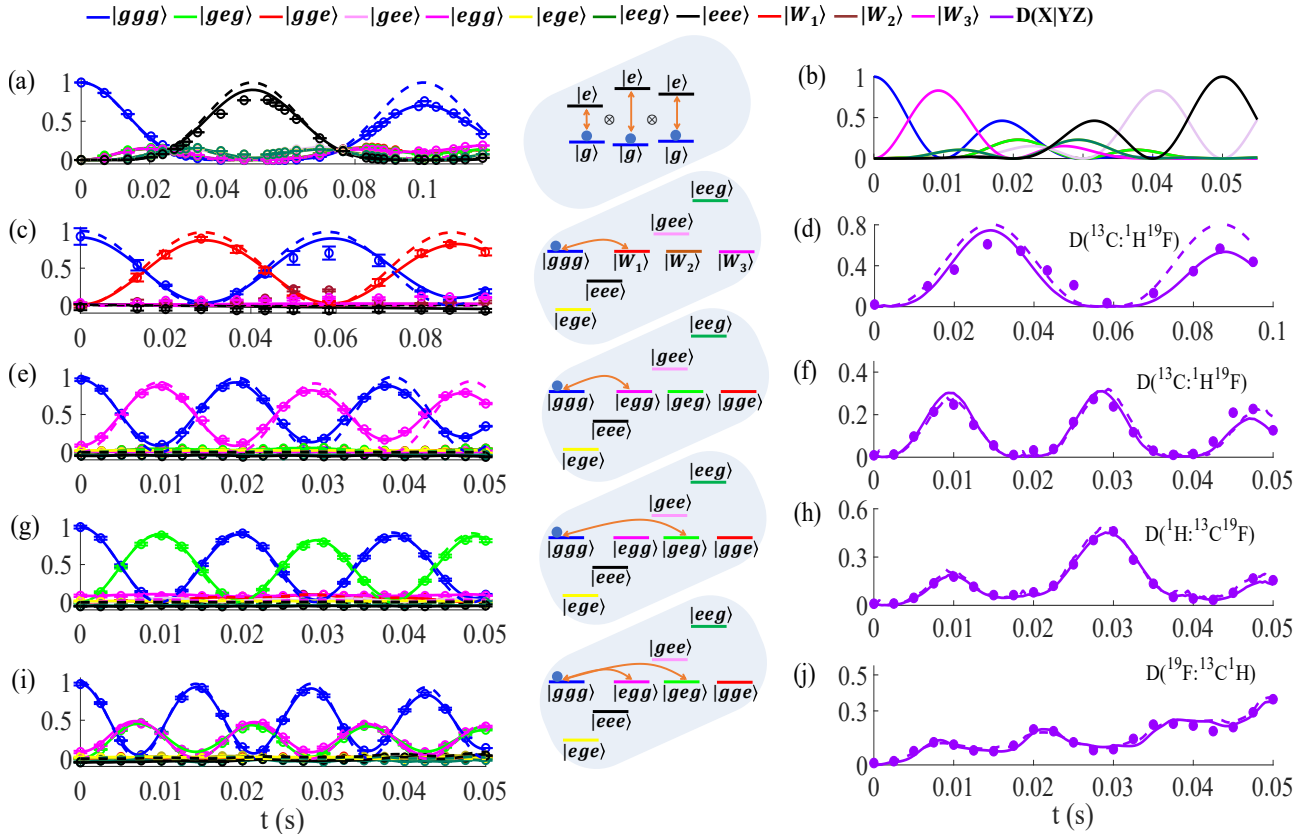


**Figure 6.6:** Population dynamics (left column) and discord (right column) versus driving time for the three-qubit register under Rabi drive (a), interaction induced blockade (c,d), freezing of the second and third qubits (e,f) and of the first and third qubits (g,h) and of only the last qubit (i,j). Plot (b) shows the population dynamics for three non interacting spins with the same driving parameters as freezing on second and third qubits (e,f), illustrating the importance of spin-spin interactions to realize freezing. Experimental data points are shown by dots with error bars (indicating random errors), theoretically expected dynamics are shown by dashed lines, and realistic numerical models are shown by solid lines. In each case, the corresponding energy level diagram is also shown (central column) with the same color coding as the legend shown at the top of the figure. The energy level diagram of (a) corresponds to uncoupled spins, while those of (c)-(g) show eigenstates of the rotating frame Hamiltonian ( $H_0$ ) in a relevant basis (upto the freedom in degenerate subspace) along with prominent transitions. The discord values  $D(X|YZ)$  are expressed in units of  $\ln 2/2\epsilon^2$  [46], where  $\epsilon$  is the purity factor as described in section 6.4.2

for the initial state  $|G\rangle$  indicated that the population exchange occurs only between  $|G\rangle$  and  $|W_1\rangle$ , while all other states are blocked. Here again the collective Rabi oscillation has a frequency of  $(\sqrt{3} \pm 0.03)\nu^{RF}$ , which also showed excellent agreement with the expected value  $\sqrt{3}\nu^{RF}$ .

Figs. 6.5(d) and 6.6(d) show the quantum discord between A:B and X:YZ at different steps of evolution under blockade conditions for two and three-qubit cases respectively. Initially, the system was prepared in a product state  $|G\rangle$ , and hence the quantum discord is zero. However, during the course of time evolution, correlations developed between the qubits, resulting in non-zero values of discord. We could see that the discord was maximized each time when the system attained the entangled state  $|+\rangle$  in the case of two-qubits and  $|W_1\rangle$  in the case of three-qubits. After incorporating the imperfections, the numerical model (solid lines) and experimental (circles) results were in excellent agreement. Brief details of discord calculations in the systems used here are given in the Appendix A.4.

### 6.5.3 Strongly interacting case: Local spin freezing

In the blockade regime, by locally amplifying the Rabi coupling (or equivalently the local transverse field in the spin model in Eq. (6.6)) of selected spins, we can freeze the dynamics of other spins, which in a Rydberg lattice is called the Rydberg biased freezing [274]. This was achieved in the two qubit NMR register by a drive on the first qubit ( $^{19}F$ ) with  $\nu_1^{RF} = 217$  Hz and on the second qubit ( $^{31}P$ ) with a weaker field, i.e.,  $\nu_2^{RF} = \nu_1^{RF}/4$ . The corresponding dynamics is shown in Fig. 6.5(e). For these values of field and interaction strengths, we expect freezing of the second qubit and it remains in its ground state  $|g\rangle$ , and the two-qubit system exhibits Rabi oscillations between  $|G\rangle$  and  $|eg\rangle$  as shown by dashed lines in Fig. 6.5(e). Due to the imperfections discussed in Sec. 6.4.2, we experimentally observed a small fraction of population in  $|ge\rangle$  (circles in Fig. 6.5(e)). After incorporating the imperfections, numerical model results (solid lines) showed excellent agreement with the experimental values. To appreciate the biased spin freezing due to the strong spin-spin interactions and the inhomogeneous Rabi coupling, we showed the same dynamics as that of the non interacting qubits, but with  $\nu_2^{RF} = \nu_1^{RF}/4$ . In the latter case, we could see that both qubits are involved in the excitation dynamics [see Fig. 6.5(b)]. If we switch the weaker drive to the first qubit and the stronger one to the second qubit, we observed prominent dynamics of the second qubit while the first qubit freezes in the presence of strong spin-spin

interactions, as shown in Fig. 6.5(g). This effect was persistent for 12 ms, which is about 0.65 times the time period of the weaker drive. These results also showed that this behaviour is not transient, but holds over extended times of evolution.

In addition to this, we also studied the regime in between Rydberg blockade and Rydberg biased freezing by gradually reducing the driving amplitude of the second qubit with respect to the first qubit and observed the populations in each of the singly excited states  $|ge\rangle$  and  $|eg\rangle$ . In Fig. 6.7(a), we show the value of population in states  $|eg\rangle$  and  $|ge\rangle$  at half the effective Rabi period, i.e., at the first crest that appeared in the Rabi dynamics. We could see that the populations start out equally in  $|ge\rangle$  and  $|eg\rangle$  states in blockade regime, with driving amplitude 217 Hz on both qubits and gradually deviated from each other as the driving fields on both qubits became different. Here, the driving amplitude of the second qubit was reduced, and hence the population in  $|ge\rangle$  gradually decreased while the population in  $|eg\rangle$  increased. The corresponding quantum discord values for each of these points is shown in Fig. 6.7(b). We could see that as the driving amplitude of the second qubit is increased, the discord also increases, signalling the shift from freezing to blockade regime. This was expected, since with increasing drive amplitude, the system dynamics is no longer restricted to the subspace of the first qubit. The second qubit dynamics also become prominent, finally resulting in the maximally entangled  $|+\rangle$  state under blockade condition. This showed that local spin freezing was not a chance occurring at some values of RF drive amplitudes, but a general phenomenon that can be realized by choosing appropriate drive parameters.

In the three-qubit register, we can studied selective freezing of either a single qubit or two qubits. To demonstrate two-qubit freezing we applied a drive on the first qubit with  $\nu_1^{\text{RF}} = 50$  Hz and the last two qubits by  $\nu_3^{\text{RF}} = \nu_2^{\text{RF}} = 10$  Hz. As seen in Fig. 6.6(e), only the first qubit took part in the excitation dynamics, resulting in Rabi oscillations between  $|G\rangle$  and  $|egg\rangle$ . Instead of the first qubit, if we drive the second qubit strongly, and weakly drive the first and the third ones, we observed Rabi oscillations between  $|G\rangle$  and  $|geg\rangle$  [see Fig. 6.6(g)]. To demonstrate single qubit freezing in the three qubit register, we applied a weak drive on the third qubit in comparison to the first two qubits, i.e.,  $\nu_1^{\text{RF}} = \nu_2^{\text{RF}} = 50$  Hz,  $\nu_3^{\text{RF}} = 10$  Hz. As shown in Fig. 6.6(i), the population dynamics in this case was between  $|G\rangle$  and the single excitation states of the first two qubits,  $|egg\rangle$  and  $|geg\rangle$  respectively, while the third qubit dynamics was suppressed. Similar to the

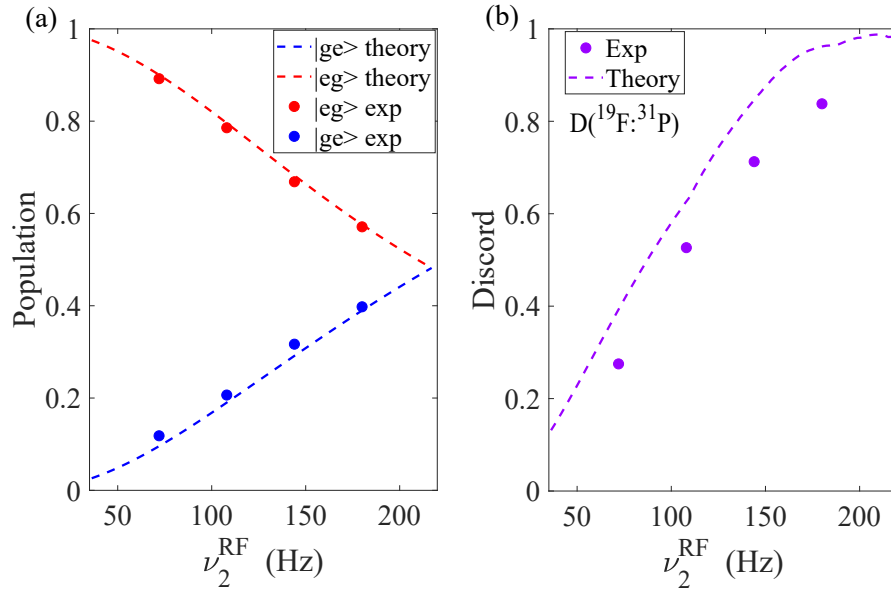


**Figure 6.7:** (a) Population in  $|ge\rangle$  and  $|eg\rangle$  as the driving amplitude of the second qubit ( $\nu_2^{RF}$ ) is gradually reduced from Rydberg blockade condition ( $\nu_1^{RF} = 217$  Hz) to Rydberg biased freezing condition (54.2 Hz) (b) the corresponding discord values  $D(A|B)$  in units of  $\ln 2/\epsilon^2$ . Experimental data are recorded at half the effective Rabi period (for each value of  $\nu_2^{RF}$ ) and shown by filled circles, which are overlaid on theoretical simulations shown by dashed lines.

two-qubit case, in the absence of spin-spin couplings between the qubits and under non-uniform drive  $\nu_2^{RF} = \nu_3^{RF} = \nu_1^{RF}/5$ , all qubits were excited simultaneously, as shown in Fig. 6.6(b). This reinforced the fact that strong spin-spin interactions cause local spin freezing and that this phenomenon sustains over extended periods of evolution under such conditions.

Figs. 6.5(f,h) and 6.6(f,h,j) show discord between A:B and X:YZ for Rydberg biased freezing scenarios in two and three qubit cases respectively. In the three-qubit case, discord was calculated for different partitions as indicated in the figure 6.6(f,h,j). We could see that less entanglement was generated under conditions of Rydberg biased freezing as compared to Rydberg blockade. This was due to considerable suppression of the dynamics of frozen qubits during the evolution. Accordingly, the dynamics was largely confined to exchanges between separable states, with less quantum correlation being created as revealed by discord values. We could also see in Fig. 6.6(j) that discord of the frozen qubit with the rest of the system was steadily increasing. Further weakening of the drive amplitude on the frozen qubit would lead to its stronger isolation and further suppression of quantum correlations.

## 6.6 Summary and outlook

In this work, we experimentally examined interaction induced blockade and local spin freezing, analogous to Rydberg blockade and Rydberg biased freezing respectively, in two- and three-qubit NMR registers. While Rydberg blockade has previously been demonstrated experimentally, we believe this is the first experimental demonstration of local spin freezing which also simulates Rydberg biased freezing. In addition, we also characterized the dynamics of quantum discord in these systems during the course of evolution under blockade and spin freezing conditions.

This experimental demonstration opens up many avenues for further investigations. The ability of interaction induced blockade, realized by a simple off-resonant drive, to create multi-qubit entanglement may have interesting applications in experimental quantum information studies. The robustness of such approaches compared to the traditional methods involving a combination of local and nonlocal gates is hitherto unexplored. Moreover, the biased local spin freezing can be utilized to selectively control and drive qubits in a multi-qubit system. This may find applications for local quantum control, such as exchanging information among a subset of qubits and controlled generation of quantum dynamics in a system of interacting qubits.

It is fascinating to note that, though the concepts of NMR spin systems are altogether different from that of Rydberg atoms, it does not hinder access to quantum phenomena featured by the latter, thus justifying the role of NMR registers as versatile quantum simulators. This work also reinforces the far reaching effects of (nonlinear) interactions in giving rise to diverse and rich physical phenomena in quantum systems.

# Thesis Summary

---

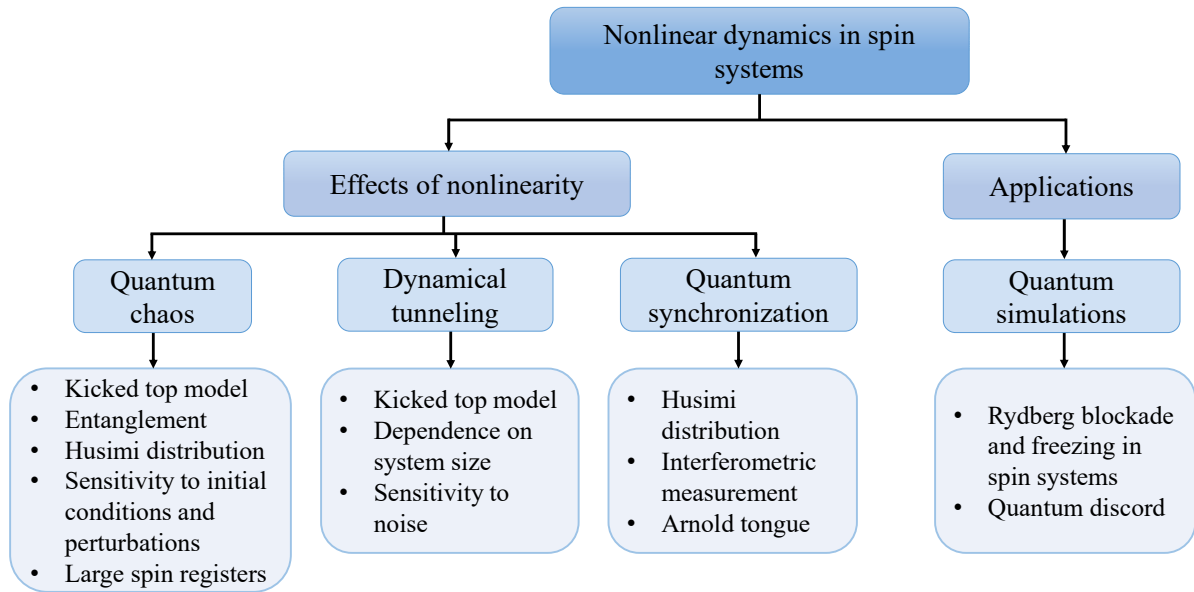


**Figure T1:** Summary of the thesis, and concepts covered in the chapters therein.

In this thesis, we have experimentally explored some nonlinear phenomena in spin systems using NMR architecture. The nonlinear effects studied include quantum chaos using the quantum kicked top (QKT) model, dynamical tunneling in two- and three-qubit systems using QKT, quantum synchronization of a four-level spin system with a weak external drive, and simulating interaction-induced Rydberg blockade and freezing in two- and three-qubit spin registers. These effects were investigated using quantum information processing tools such as von Neumann entropy and quantum discord for quantifying quantum correlations, Husimi quasi-probability distribution for phase space analysis, interferometric technique and quantum state tomography for readout, as summarized in Fig. T1. This thesis highlights the scope and implications of these phenomena for fundamental studies and application in quantum computing and information processing, and the versatility of NMR platform for performing quantum simulations.

The work explored here can be extended to study many phenomena in NMR spin systems which are of interest from fundamental perspectives and applications in quantum information. For

instance, multiple facets of quantum chaos can be investigated - including its complete characterization in star systems, OTOCs (as demonstrated in [201]), effects of quantum chaos in quantum control, nonlinear dynamics using quadrupolar spins ( $I > 1$ ), interplay between quantum chaos and time-crystalline behaviour, quantum many-body effects [284–287], dynamics of quantum coherences and correlations under chaos, quantum chaotic effects in quantum algorithms [85], etc. It would also be of interest to probe other models of quantum chaos and their effects, such as the ratchet effect [288], in spin systems. Although the studies here have been performed on small spin systems, these approaches can be extended to larger systems such as solid-state NMR systems with dipolar interactions [286, 289]. There is no doubt that nonlinear effects and interactions give rise to diverse phenomena in quantum systems, and studying these can help further our understanding of physics and also develop useful quantum technology applications.

# Appendix

---

## A.1 Pulsed Field Gradient

The pulsed field gradient is a spatially varying magnetic field which is introduced to add additional space-dependent phase, as required. In this thesis, all the gradients used were spatially varying along the  $z$  axis, and can be described by the Hamiltonian [49]

$$B_{\text{PFG}}(z) = G_z z \hat{z}.$$

In the presence of such a gradient, spins at different positions along the length of the sample ( $\hat{z}$ ) experience different local magnetic fields. Since the Larmor frequency of the spins is directly proportional to the magnetic field, the transverse components of the magnetization vector precess at different Larmor frequencies along the length of the sample. Hence, over the duration of application of the gradient, any phase coherence between the transverse components of the magnetization along the sample length gets destroyed, and this effectively eliminates the net transverse magnetization over the bulk sample volume. This effect is pictorially shown in Fig. T1 starting from a state with uniform transverse magnetization. It is important to note that the effects of gradient are under precise control, and reversible (for time scales  $\ll T_2$ ). By applying a negative gradient (reversing direction), the spatial dephasing can be reversed and phase coherence can be restored.

## A.2 Quantum State Tomography Pulse Sequences

### A.2.1 Single qubit tomography example

In NMR architecture, the detection operator is given by  $D = \sigma_x + i\sigma_y$ , and the signal is described by  $M = \text{Tr}(\rho D)$ . These signals can be absorptive or dispersive (due to the complex phase factor). To avoid errors from integration of dispersive signals, we measure only absorptive signals, i.e.,

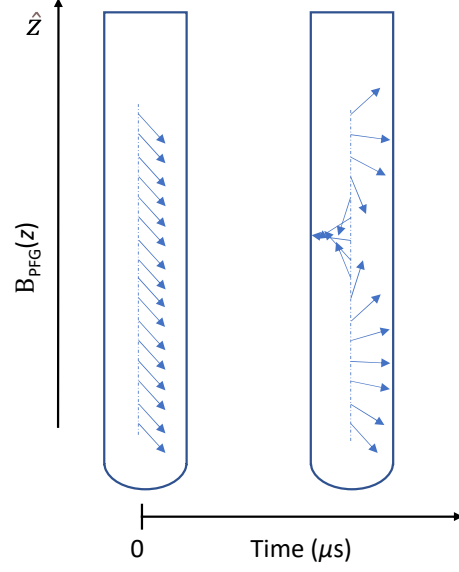


**Figure T1:** Effect of  $\hat{z}$  gradient.

along  $D_{ab} = \sigma_x$  such that  $M = \text{Tr}(\rho D_{ab}) = \text{Tr}(\rho \sigma_x)$ , which will pick out the real part of the density matrix's off-diagonal element.

Consider a general single qubit traceless density matrix given by  $\rho = \begin{bmatrix} p_0 & a + ib \\ a - ib & -p_0 \end{bmatrix}$ .

(i) Extracting populations - the population  $p_0$  is a diagonal element and not directly detectable.

Hence we transform it to the off-diagonal element and then detect by the following protocol.

$$\rho \xrightarrow{PFG} \begin{bmatrix} p_0 & 0 \\ 0 & -p_0 \end{bmatrix} \xrightarrow{(\pi/2)_y} \begin{bmatrix} 0 & p_0 \\ p_0 & 0 \end{bmatrix} = p_0 \sigma_x; M_1 = \text{Tr}(\rho \sigma_x) = \text{Tr}((p_0 \sigma_x) \sigma_x) = p_0. \quad (6.11)$$

(ii) Extracting real component of off-diagonal element

$$\rho \xrightarrow{(\pi/2)_y} \begin{bmatrix} a & ib - p_0 \\ -ib - p_0 & -a \end{bmatrix} \xrightarrow{PFG} \begin{bmatrix} a & 0 \\ 0 & -a \end{bmatrix} \xrightarrow{(\pi/2)_y} \begin{bmatrix} 0 & a \\ a & 0 \end{bmatrix} = a \sigma_x$$

$$M_2 = \text{Tr}(\rho \sigma_x) = \text{Tr}((a \sigma_x) \sigma_x) = a. \quad (6.12)$$

Note that direct detection will also give the real component of the off-diagonal element directly.

(iii) Extracting imaginary component of off-diagonal element

$$\rho \xrightarrow{(\pi/2)_x} \begin{bmatrix} b & a - ip_0 \\ a + ip_0 & -b \end{bmatrix} \xrightarrow{PFG} \begin{bmatrix} b & 0 \\ 0 & -b \end{bmatrix} \xrightarrow{(\pi/2)_y} \begin{bmatrix} 0 & b \\ b & 0 \end{bmatrix} = b\sigma_x$$

$$M_3 = \text{Tr}(\rho\sigma_x) = \text{Tr}((b\sigma_x)\sigma_x) = b. \quad (6.13)$$

Hence from the area under the peaks (signals) measured in each experiment, we can reconstruct the original density matrix as  $\rho = \begin{bmatrix} M_1 & M_2 + iM_3 \\ M_2 - iM_3 & -M_1 \end{bmatrix} = \begin{bmatrix} p_0 & a + ib \\ a - ib & -p_0 \end{bmatrix}$ .

The NMR pulse sequences for absorptive full-state quantum state tomography (QST) [155] of the two- and three-qubit systems used in this thesis are given below. QST for different systems comprise of multiple experiments. Each experiment ( $U_i$ ) has some pulses and free evolution under the internal Hamiltonian  $H_{\text{int}} = \sum_{i,j>i} 2\pi\mathcal{J}_{ij}I_{zi}I_{zj}$  whose operations can be summarized as  $U_i\rho U_i^\dagger$ . In each experiment, the unitary operators are followed by a gradient and detection pulse ( $U_{di}$ ) of appropriate angle about the  $y$ -axis.

## A.2.2 Two-qubit system

The optimized QST protocol for determining the two-qubit state  $\rho$  of sodium fluorophosphate ( $^{19}\text{F}$  and  $^{31}\text{P}$ ) system comprised of six experiments. The sequence of experiments (with operators time ordered from right to left) are -

1.  $U_1 = \mathbb{1}; U_{d1} = \left(\frac{\pi}{4}\right)_y^{F,P}$
2.  $U_2 = \left(\frac{\pi}{3}\right)_x^{F,P}; U_{d2} = \left(\frac{\pi}{4}\right)_y^{F,P}$
3.  $U_3 = \left(\frac{\pi}{3}\right)_y^{F,P}; U_{d3} = \left(\frac{\pi}{6}\right)_y^{F,P}$
4.  $U_4 = \left(\frac{\pi}{3}\right)_x^{F,P} \exp(-iH_{\text{int}}\tau_1)$ , with  $\tau_1 = 0.0018$  s;  $U_{d4} = \left(\frac{\pi}{4}\right)_y^{F,P}$
5.  $U_5 = \left(\frac{\pi}{3}\right)_y^{F,P} \exp(-iH_{\text{int}}\tau_2)$ , with  $\tau_2 = 0.0005$  s;  $U_{d5} = \left(\frac{\pi}{6}\right)_y^{F,P}$
6.  $U_6 = \left(\frac{\pi}{3}\right)_x^{F,P} \exp(-iH_{\text{int}}\tau_3) \left(\frac{\pi}{3}\right)_x^{F,P}$ , with  $\tau_3 = 0.0005$  s;  $U_{d6} = \left(\frac{\pi}{3}\right)_y^{F,P}$

### A.2.3 Three-qubit system

The QST protocol for the three-qubit dibromofluoromethane system ( $^{13}\text{C}$ ,  $^1\text{H}$  and  $^{19}\text{F}$ ) comprised of twelve experiments as described below.

1.  $U_1 = \mathbb{1}; U_{d1} = \left(\frac{\pi}{12}\right)_{-y}^{C,H,F}$
2.  $U_2 = \left(\frac{\pi}{3}\right)_{-x}^{C,H,F}; U_{d2} = \left(\frac{\pi}{6}\right)_{-y}^{C,H,F}$
3.  $U_3 = \left(\frac{\pi}{3}\right)_y^{C,H,F}; U_{d3} = \left(\frac{\pi}{5.1426}\right)_{-y}^{C,H,F}$
4.  $U_4 = \left(\frac{\pi}{3}\right)_{-x}^{C,H,F} \exp(-iH_{\text{int}}\tau_1)$ , with  $\tau_1 = 0.0019$  s;  $U_{d4} = \left(\frac{\pi}{6}\right)_y^{C,H,F}$
5.  $U_5 = \left(\frac{\pi}{3}\right)_y^{C,H,F} \exp(-iH_{\text{int}}\tau_2)$ , with  $\tau_2 = 0.0019$  s;  $U_{d5} = \left(\frac{\pi}{5.1426}\right)_{-y}^{C,H,F}$
6.  $U_6 = \exp(-iH_{\text{int}}\tau_4) \left(\frac{\pi}{3}\right)_{-x}^{C,H,F} \exp(-iH_{\text{int}}\tau_3)$ , with  $\tau_3 = 0.0072$  s,  $\tau_4 = 0.0101$  s;  $U_{d6} = \left(\frac{\pi}{3}\right)_y^{C,H,F}$
7.  $U_7 = \exp(-iH_{\text{int}}\tau_6) \left(\frac{\pi}{3}\right)_y^{C,H,F} \exp(-iH_{\text{int}}\tau_5)$ , with  $\tau_5 = 0.0101$  s,  $\tau_6 = 0.0101$  s;  $U_{d7} = \left(\frac{\pi}{5.1426}\right)_{-y}^{C,H,F}$
8.  $U_8 = \left(\frac{\pi}{3}\right)_{-x}^{C,H,F} \exp(-iH_{\text{int}}\tau_7) \left(\frac{\pi}{3.2728}\right)_{-x}^{C,H,F}$ , with  $\tau_7 = 0.0081$  s;  $U_{d8} = \left(\frac{\pi}{5.1426}\right)_{-y}^{C,H,F}$
9.  $U_9 = \left(\frac{\pi}{3}\right)_{-x}^{C,H,F} \exp(-iH_{\text{int}}\tau_8) \left(\frac{\pi}{3}\right)_y^{C,H,F}$ , with  $\tau_8 = 0.0101$  s;  $U_{d9} = \left(\frac{\pi}{5.1426}\right)_y^{C,H,F}$
10.  $U_{10} = \left(\frac{\pi}{3}\right)_{-y}^{C,H,F} \exp(-iH_{\text{int}}\tau_9) \left(\frac{\pi}{4}\right)_x^{C,H,F}$ , with  $\tau_9 = 0.0018$  s;  $U_{d10} = \left(\frac{\pi}{5.1426}\right)_{-y}^{C,H,F}$
11.  $U_{11} = \left(\frac{\pi}{3.2728}\right)_{-y}^{C,H,F} \exp(-iH_{\text{int}}\tau_{10}) \left(\frac{\pi}{3}\right)_y^{C,H,F}$ , with  $\tau_{10} = 0.0101$  s;  $U_{d11} = \left(\frac{\pi}{5.1426}\right)_{-y}^{C,H,F}$
12.  $U_{12} = \exp(-iH_{\text{int}}\tau_{12}) \left(\frac{\pi}{3}\right)_{-y}^H \left(\frac{\pi}{3}\right)_{-x}^{C,F} \exp(-iH_{\text{int}}\tau_{11}) \left(\frac{\pi}{3.5999}\right)_{-x}^H \left(\frac{\pi}{3.5999}\right)_{-y}^{C,F}$ , with  $\tau_{11} = 0.0078$  s,  $\tau_{12} = 0.0051$  s;  $U_{d12} = \left(\frac{\pi}{6}\right)_y^{C,H,F}$

### A.3 Estimating scalar spin-spin coupling

The scalar spin-spin coupling present in liquid state NMR samples can be directly obtained from the spectrum of either of the coupled nuclei as explained below. The Hamiltonian of two coupled heteronuclear spins ( $AB$ ) is given by  $H = \Omega_A I_{zA} + \Omega_B I_{zB} + 2\pi J_{AB} I_{zA} I_{zB}$ , where  $\Omega_i = -2\pi\nu_i$

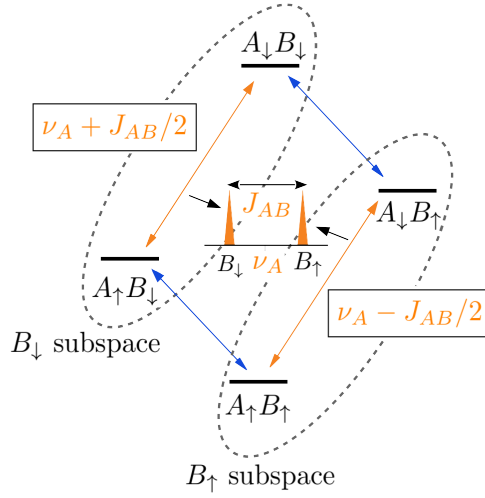


**Figure T1:** Energy level diagram of coupled two-qubit system of spins  $AB$ . The spectrum of spin  $A$  is shown in the center with two peaks at frequencies  $\nu_A - J_{AB}/2$  and  $\nu_A + J_{AB}/2$  respectively which correspond to  $B_\uparrow$  and  $B_\downarrow$  configurations.

are the chemical shifts of the spins, and  $J_{AB}$  is the scalar spin-spin coupling. The eigenstates and their corresponding energies (in Hz) for this two-qubit system shown in Fig. T1 are

$$\begin{aligned}
 A_\uparrow B_\uparrow & & -\nu_A/2 - \nu_B/2 + J_{AB}/4 \\
 A_\uparrow B_\downarrow & & -\nu_A/2 + \nu_B/2 - J_{AB}/4 \\
 A_\downarrow B_\uparrow & & +\nu_A/2 - \nu_B/2 - J_{AB}/4 \\
 A_\downarrow B_\downarrow & & +\nu_A/2 + \nu_B/2 + J_{AB}/4.
 \end{aligned}$$

(6.14)

Consider the transitions of spin  $A$ . There are two transitions allowed by magnetic dipole interaction rules, which are  $A_\uparrow B_\uparrow \rightarrow A_\downarrow B_\uparrow$  in which spin  $B$  remains in the  $\uparrow$  state and  $A_\uparrow B_\downarrow \rightarrow A_\downarrow B_\downarrow$  in which spin  $B$  remains in the  $\downarrow$  state. These are shown by yellow arrows in Fig. T1. The energies of these two transitions can be calculated to be  $\nu_A - J_{AB}/2$  and  $\nu_A + J_{AB}/2$  respectively. These are the two frequencies that are obtained in the spectrum of spin  $A$ , shown in the center of Fig. T1. The difference in frequencies between the two transitions in the spectrum of spin  $A$  directly gives the value of  $J_{AB}$ . Identical information will be obtained from the spectrum of spin  $B$ .

## A.4 Estimating quantum discord

For discord calculations, we use bipartition of two-qubit system as A:B and for three-qubit system as A:BC, and measurement is performed on the first qubit. Optimization over multiple measurement bases was performed considering the generalized orthonormal single-qubit basis vectors [46],  $|\psi_1\rangle = \cos(\theta/2)|0\rangle + \exp(i\phi)\sin(\theta/2)|1\rangle$  and  $|\psi_2\rangle = \sin(\theta/2)|0\rangle - \exp(i\phi)\cos(\theta/2)|1\rangle$ . By varying  $\{\theta, \phi\}$ , we can cover multiple measurement bases required for calculating discord. For a two-qubit system, we used the protocol given in Ref. [290] where they developed a set of optimized bases that bypasses the need for scanning over basis vectors  $|\psi_1\rangle, |\psi_2\rangle$ .

For three-qubit systems, we used optimization over  $\{|\psi_1\rangle, |\psi_2\rangle\}$  basis vectors, and the distribution of  $\{\theta, \phi\}$  for this procedure was generated using the triangulation function `spheretri` [291]. The density matrix was permuted to generate different ordering of qubits  $ABC, BAC, CAB$  to facilitate efficient partial trace and measurement operations.

For a general system described by  $\rho$ , for any value of  $\{\theta, \phi\}$ , the measurement operators on a qubit  $A$  can be obtained as  $M_{1A} = |\psi_1\rangle\langle\psi_1| \otimes \mathbb{1}$  and  $M_{2A} = |\psi_2\rangle\langle\psi_2| \otimes \mathbb{1}$ . The post-measurement states of the system are  $\rho_1 = M_{1A}\rho M_{1A}'$ , and  $\rho_2 = M_{2A}\rho M_{2A}'$ , each weighted with their corresponding probabilities. This helps evaluate the conditional entropy  $S(A|B) = p_1S(\rho_1) + p_2S(\rho_2)$  for a pair of  $\{\theta, \phi\}$ , and the procedure is repeated for all values of  $\{\theta, \phi\}$  to obtain the optimum. Following this, the value of discord can be obtained using Eqs. 1.25 and 1.26.





---

## Bibliography

---

- [1] Richard P Feynman. Simulating physics with computers. *International Journal of Theoretical Physics*, 21(6/7), 1982.
- [2] Charles H. Bennett and Gilles Brassard. Quantum cryptography: Public key distribution and coin tossing. *Theoretical Computer Science*, 560:7–11, 2014. Theoretical Aspects of Quantum Cryptography – celebrating 30 years of BB84.
- [3] David Deutsch and Richard Jozsa. Rapid solution of problems by quantum computation. *Proceedings of the Royal Society of London. Series A: Mathematical and Physical Sciences*, 439(1907):553–558, 1992.
- [4] P.W. Shor. Algorithms for quantum computation: discrete logarithms and factoring. In *Proceedings 35th Annual Symposium on Foundations of Computer Science*, pages 124–134, 1994.
- [5] Lov K. Grover. A fast quantum mechanical algorithm for database search. In *Proceedings of the Twenty-Eighth Annual ACM Symposium on Theory of Computing*, STOC '96, page 212–219, New York, NY, USA, 1996. Association for Computing Machinery.
- [6] David G. Cory, Amr F. Fahmy, and Timothy F. Havel. Ensemble quantum computing by nmr spectroscopy. *Proceedings of the National Academy of Sciences*, 94(5):1634–1639, 1997.
- [7] Neil A. Gershenfeld and Isaac L. Chuang. Bulk spin-resonance quantum computation. *Science*, 275(5298):350–356, 1997.
- [8] John Preskill. Quantum computing 40 years later, 2021.
- [9] Andreas Trabesinger. Quantum simulation. *Nature Physics*, 8(4):263–263, 2012.

- [10] I. M. Georgescu, S. Ashhab, and Franco Nori. Quantum simulation. *Rev. Mod. Phys.*, 86:153–185, Mar 2014.
- [11] Yasunobu Nakamura, Yu A Pashkin, and JS Tsai. Coherent control of macroscopic quantum states in a single-cooper-pair box. *nature*, 398(6730):786–788, 1999.
- [12] G Wendin. Quantum information processing with superconducting circuits: a review. *Reports on Progress in Physics*, 80(10):106001, sep 2017.
- [13] J. I. Cirac and P. Zoller. Quantum computations with cold trapped ions. *Phys. Rev. Lett.*, 74:4091–4094, May 1995.
- [14] Colin D Bruzewicz, John Chiaverini, Robert McConnell, and Jeremy M Sage. Trapped-ion quantum computing: Progress and challenges. *Applied Physics Reviews*, 6(2):021314, 2019.
- [15] D. Jaksch and P. Zoller. The cold atom hubbard toolbox. *Annals of Physics*, 315(1):52–79, 2005. Special Issue.
- [16] Maciej Lewenstein, Anna Sanpera, Veronica Ahufinger, Bogdan Damski, Aditi Sen(De), and Ujjwal Sen. Ultracold atomic gases in optical lattices: mimicking condensed matter physics and beyond. *Advances in Physics*, 56(2):243–379, 2007.
- [17] Immanuel Bloch, Jean Dalibard, and Sylvain Nascimbene. Quantum simulations with ultracold quantum gases. *Nature Physics*, 8(4):267–276, 2012.
- [18] Daniel Loss and David P. DiVincenzo. Quantum computation with quantum dots. *Phys. Rev. A*, 57:120–126, Jan 1998.
- [19] Guido Burkard, Hans-Andreas Engel, and Daniel Loss. Spintronics and quantum dots for quantum computing and quantum communication. *Fortschritte der Physik*, 48(9-11):965–986.
- [20] Christoph Kloeffel and Daniel Loss. Prospects for spin-based quantum computing in quantum dots. *Annual Review of Condensed Matter Physics*, 4(1):51–81, 2013.

- [21] Emanuel Knill, Raymond Laflamme, and Gerald J Milburn. A scheme for efficient quantum computation with linear optics. *nature*, 409(6816):46–52, 2001.
- [22] Jeremy L. O’Brien. Optical quantum computing. *Science*, 318(5856):1567–1570, 2007.
- [23] Pieter Kok, W. J. Munro, Kae Nemoto, T. C. Ralph, Jonathan P. Dowling, and G. J. Milburn. Linear optical quantum computing with photonic qubits. *Rev. Mod. Phys.*, 79:135–174, Jan 2007.
- [24] Stefanie Barz. Quantum computing with photons: introduction to the circuit model, the one-way quantum computer, and the fundamental principles of photonic experiments. 48(8):083001, mar 2015.
- [25] Ibm, the quantum experience.
- [26] Frank Arute, Kunal Arya, Ryan Babbush, Dave Bacon, Joseph C Bardin, Rami Barends, Rupak Biswas, Sergio Boixo, Fernando GSL Brandao, David A Buell, et al. Quantum supremacy using a programmable superconducting processor. *Nature*, 574(7779):505–510, 2019.
- [27] D-wave systems.
- [28] Ionq, trapped ion quantum computing.
- [29] Rigetti computing: Quantum computing.
- [30] Psiquantum: fault tolerant quantum computing.
- [31] Michael A. Nielsen and Isaac L. Chuang. *Quantum Computation and Quantum Information: 10th Anniversary Edition*. Cambridge University Press, 2010.
- [32] Ryszard Horodecki, Paweł Horodecki, Michał Horodecki, and Karol Horodecki. Quantum entanglement. *Rev. Mod. Phys.*, 81:865–942, Jun 2009.
- [33] Gerardo Adesso, Thomas R Bromley, and Marco Cianciaruso. Measures and applications of quantum correlations. *Journal of Physics A: Mathematical and Theoretical*, 49(47):473001, 2016.

- [34] Yuchen Wang, Zixuan Hu, Barry C. Sanders, and Sabre Kais. Qudits and high-dimensional quantum computing. *Frontiers in Physics*, 8, 2020.
- [35] Yulin Chi, Jieshan Huang, Zhanchuan Zhang, Jun Mao, Zinan Zhou, Xiaojiong Chen, Chonghao Zhai, Jueming Bao, Tianxiang Dai, Huihong Yuan, et al. A programmable qudit-based quantum processor. *Nature communications*, 13(1):1–10, 2022.
- [36] Oleg Kupervasser. Chapter 3 - principal paradoxes of quantum mechanics. In Oleg Kupervasser, editor, *Application of New Cybernetics in Physics*, pages 73 – 120. Elsevier, Amsterdam, 2017.
- [37] Martin B. Plenio and S. Virmani. An introduction to entanglement measures. 2005.
- [38] Asher Peres. Separability criterion for density matrices. *Phys. Rev. Lett.*, 77:1413–1415, Aug 1996.
- [39] Charles H. Bennett, David P. DiVincenzo, Christopher A. Fuchs, Tal Mor, Eric Rains, Peter W. Shor, John A. Smolin, and William K. Wootters. Quantum nonlocality without entanglement. *Phys. Rev. A*, 59:1070–1091, Feb 1999.
- [40] J. Niset and N. J. Cerf. Multipartite nonlocality without entanglement in many dimensions. *Phys. Rev. A*, 74:052103, Nov 2006.
- [41] B. P. Lanyon, M. Barbieri, M. P. Almeida, and A. G. White. Experimental quantum computing without entanglement. *Phys. Rev. Lett.*, 101:200501, Nov 2008.
- [42] Kavan Modi, Aharon Brodutch, Hugo Cable, Tomasz Paterek, and Vlatko Vedral. The classical-quantum boundary for correlations: Discord and related measures. *Rev. Mod. Phys.*, 84:1655–1707, Nov 2012.
- [43] T. S. Mahesh, C. S. Sudheer Kumar, and Udaysinh T. Bhosale. *Quantum Correlations in NMR Systems*, pages 499–516. Springer International Publishing, Cham, 2017.
- [44] Harold Ollivier and Wojciech H Zurek. Quantum discord: a measure of the quantumness of correlations. *Physical review letters*, 88(1):017901, 2001.

- [45] L Henderson and V Vedral. Classical, quantum and total correlations. *Journal of Physics A: Mathematical and General*, 34(35):6899–6905, aug 2001.
- [46] Hemant Katiyar, Soumya Singha Roy, T. S Mahesh, and Apoorva Patel. Evolution of quantum discord and its stability in two-qubit nmr systems. *Physical Review A*, 86(1):012309, 2012.
- [47] Anatole Abragam. *The principles of nuclear magnetism*. Number 32. Oxford university press, 1961.
- [48] J. Cavanagh, W. J. Fairbrother, A. G. Palmer III, and N. J. Skelton. *Protein NMR spectroscopy: principles and practice*. Elsevier, 1995.
- [49] M. H. Levitt. *Spin dynamics: basics of nuclear magnetic resonance*. John Wiley and Sons, 2001.
- [50] Charles P Slichter. *Principles of magnetic resonance*, volume 1. Springer Science & Business Media, 2013.
- [51] E. Knill and R. Laflamme. Power of one bit of quantum information. *Phys. Rev. Lett.*, 81:5672–5675, Dec 1998.
- [52] Ivan Oliveira, Roberto Sarthour Jr, Tito Bonagamba, Eduardo Azevedo, and Jair CC Freitas. *NMR quantum information processing*. Elsevier, 2011.
- [53] D.G. Cory, R. Laflamme, E. Knill, L. Viola, T.F. Havel, N. Boulant, G. Boutis, E. Fortunato, S. Lloyd, R. Martinez, C. Negrevergne, M. Pravia, Y. Sharf, G. Teklemariam, Y.S. Weinstein, and W.H. Zurek. Nmr based quantum information processing: Achievements and prospects. *Fortschritte der Physik*, 48(9-11):875–907, 2000.
- [54] Abhishek Shukla, Manvendra Sharma, and T.S. Mahesh. Noon states in star-topology spin-systems: Applications in diffusion studies and rf inhomogeneity mapping. *Chemical Physics Letters*, 592:227–231, 2014.
- [55] Deepak Khurana, V. R. Krithika, and T. S. Mahesh. Unambiguous measurement of information scrambling in a hierarchical star-topology system, 2019.

- [56] T S Mahesh, Deepak Khurana, V R Krithika, G J Sreejith, and C S Sudheer Kumar. Star-topology registers: Nmr and quantum information perspectives. *Journal of Physics: Condensed Matter*, 33(38):383002, jul 2021.
- [57] James Keeler. *Understanding NMR spectroscopy*. John Wiley & Sons, 2010.
- [58] V. R. Krithika, Soham Pal, Rejish Nath, and T. S. Mahesh. Observation of interaction induced blockade and local spin freezing in a nmr quantum simulator. *Phys. Rev. Research*, 3:033035, Jul 2021.
- [59] David P. DiVincenzo. The physical implementation of quantum computation. *Fortschritte der Physik*, 48(9-11):771–783, 2000.
- [60] E. Knill, I. Chuang, and R. Laflamme. Effective pure states for bulk quantum computation. *Phys. Rev. A*, 57:3348–3363, May 1998.
- [61] Soumya Singha Roy and T.S. Mahesh. Density matrix tomography of singlet states. *Journal of Magnetic Resonance*, 206(1):127–133, 2010.
- [62] Abhishek Shukla, K. Rama Koteswara Rao, and T. S. Mahesh. Ancilla-assisted quantum state tomography in multiqubit registers. *Phys. Rev. A*, 87:062317, Jun 2013.
- [63] Steven H Strogatz. *Nonlinear dynamics and chaos: with applications to physics, biology, chemistry, and engineering*. CRC press, 2018.
- [64] Irving R Epstein and Kenneth Showalter. Nonlinear chemical dynamics: oscillations, patterns, and chaos. *The Journal of Physical Chemistry*, 100(31):13132–13147, 1996.
- [65] Tomasz Kapitaniak. *Chaos for engineers: theory, applications, and control*, volume 3. Springer Science & Business Media, 2000.
- [66] Edward Ott. *Chaos in dynamical systems*. Cambridge university press, 2002.
- [67] Roderick V Jensen. Quantum chaos. *Nature*, 355(6358):311–318, 1992.
- [68] Martin C. Gutzwiller. Quantum chaos. *Scientific American*, 266(1):78–85, 1992.

- [69] D. Wintgen and H. Friedrich. Regularity and irregularity in spectra of the magnetized hydrogen atom. *Phys. Rev. Lett.*, 57:571–574, Aug 1986.
- [70] Hans-Jürgen Stöckmann. *Quantum chaos: an introduction*. American Association of Physics Teachers, 2000.
- [71] Martin C Gutzwiller. *Chaos in classical and quantum mechanics*, volume 1. Springer Science & Business Media, 2013.
- [72] Fritz Haake. *Quantum Signatures of Chaos*. Springer Berlin, Heidelberg, 2010.
- [73] Steven Tomsovic and Denis Ullmo. Chaos-assisted tunneling. *Phys. Rev. E*, 50:145–162, Jul 1994.
- [74] Giulio Casati. Quantum chaos. *Chaos: An Interdisciplinary Journal of Nonlinear Science*, 6(3):391–398, 1996.
- [75] Winfried K Hensinger, Hartmut Häffner, Antoine Browaeys, Norman R Heckenberg, Kris Helmerson, Callum McKenzie, Gerard J Milburn, William D Phillips, Steve L Rolston, Halina Rubinsztein-Dunlop, et al. Dynamical tunnelling of ultracold atoms. *Nature*, 412(6842):52–55, 2001.
- [76] Daniel A. Steck, Windell H. Oskay, and Mark G. Raizen. Observation of chaos-assisted tunneling between islands of stability. *Science*, 293(5528):274–278, 2001.
- [77] Tobias Graß, Bruno Juliá-Díaz, Marek Kuś, and Maciej Lewenstein. Quantum chaos in  $su(3)$  models with trapped ions. *Phys. Rev. Lett.*, 111:090404, Aug 2013.
- [78] S Chaudhury, A Smith, BE Anderson, S Ghose, and Poul S Jessen. Quantum signatures of chaos in a kicked top. *Nature*, 461(7265):768–771, 2009.
- [79] Gabriela B Lemos, Rafael M Gomes, Stephen P Walborn, Paulo H Souto Ribeiro, and Fabricio Toscano. Experimental observation of quantum chaos in a beam of light. *Nature communications*, 3(1):1–7, 2012.
- [80] Jonas Larson, Brandon M. Anderson, and Alexander Altland. Chaos-driven dynamics in spin-orbit-coupled atomic gases. *Phys. Rev. A*, 87:013624, Jan 2013.

- [81] Charles Neill, P Roushan, M Fang, Y Chen, M Kolodrubetz, Z Chen, A Megrant, R Barends, B Campbell, B Chiaro, et al. Ergodic dynamics and thermalization in an isolated quantum system. *Nature Physics*, 12(11):1037–1041, 2016.
- [82] M. Bitter and V. Milner. Experimental demonstration of coherent control in quantum chaotic systems. *Phys. Rev. Lett.*, 118:034101, Jan 2017.
- [83] Elmer V. H. Doggen, Bertrand Georgeot, and Gabriel Lemarié. Chaos-assisted tunneling in the presence of anderson localization. *Phys. Rev. E*, 96:040201, Oct 2017.
- [84] A. G. Araujo-Ferreira, R. Aucaise, R. S. Sarthour, I. S. Oliveira, T. J. Bonagamba, and I. Roditi. Classical bifurcation in a quadrupolar nmr system. *Phys. Rev. A*, 87:053605, May 2013.
- [85] Daniel Braun. Quantum chaos and quantum algorithms. *Phys. Rev. A*, 65:042317, Apr 2002.
- [86] Lukas M Sieberer, Tobias Olsacher, Andreas Elben, Markus Heyl, Philipp Hauke, Fritz Haake, and Peter Zoller. Digital quantum simulation, trotter errors, and quantum chaos of the kicked top. *npj Quantum Information*, 5(1):1–11, 2019.
- [87] Tobias Olsacher, Lorenzo Pastori, Christian Kokail, Lukas M Sieberer, and Peter Zoller. Digital quantum simulation, learning of the floquet hamiltonian, and quantum chaos of the kicked top. *Journal of Physics A: Mathematical and Theoretical*, 55(33):334003, aug 2022.
- [88] B. Georgeot and D. L. Shepelyansky. Emergence of quantum chaos in the quantum computer core and how to manage it. *Phys. Rev. E*, 62:6366–6375, Nov 2000.
- [89] D. L. Shepelyansky. Quantum chaos and quantum computers. *Physica Scripta*, T90(1):112, 2001.
- [90] Christoph Berke, Evangelos Varvelis, Simon Trebst, Alexander Altland, and David P DiVincenzo. Transmon platform for quantum computing challenged by chaotic fluctuations. *Nature communications*, 13(1):1–10, 2022.

- [91] Xiaoguang Wang, Shohini Ghose, Barry C. Sanders, and Bambi Hu. Entanglement as a signature of quantum chaos. *Phys. Rev. E*, 70:016217, Jul 2004.
- [92] M. Lombardi and A. Matzkin. Entanglement and chaos in the kicked top. *Phys. Rev. E*, 83:016207, Jan 2011.
- [93] Joshua B. Ruebeck, Jie Lin, and Arjendu K. Pattanayak. Entanglement and its relationship to classical dynamics. *Phys. Rev. E*, 95:062222, Jun 2017.
- [94] Jayendra N. Bandyopadhyay and Arul Lakshminarayan. Entanglement production in coupled chaotic systems: Case of the kicked tops. *Phys. Rev. E*, 69:016201, Jan 2004.
- [95] Jayendra N. Bandyopadhyay and Arul Lakshminarayan. Testing statistical bounds on entanglement using quantum chaos. *Phys. Rev. Lett.*, 89:060402, Jul 2002.
- [96] Fritz Haake, Harald Wiedemann, and Karol Życzkowski. Lyapunov exponents from quantum dynamics. *Annalen der Physik*, 504(7):531–539, 1992.
- [97] Vaibhav Madhok, Vibhu Gupta, Denis-Alexandre Trottier, and Shohini Ghose. Signatures of chaos in the dynamics of quantum discord. *Phys. Rev. E*, 91:032906, Mar 2015.
- [98] O. Bohigas, M. J. Giannoni, and C. Schmit. Characterization of chaotic quantum spectra and universality of level fluctuation laws. *Phys. Rev. Lett.*, 52:1–4, Jan 1984.
- [99] Tanmoy Bhattacharya, Salman Habib, and Kurt Jacobs. Continuous quantum measurement and the emergence of classical chaos. *Phys. Rev. Lett.*, 85:4852–4855, Dec 2000.
- [100] Wojciech Hubert Zurek and Juan Pablo Paz. Quantum chaos: a decoherent definition. *Physica D: Nonlinear Phenomena*, 83(1):300–308, 1995. Quantum Complexity in Mesoscopic Systems.
- [101] Salman Habib, Kosuke Shizume, and Wojciech Hubert Zurek. Decoherence, chaos, and the correspondence principle. *Phys. Rev. Lett.*, 80:4361–4365, May 1998.
- [102] Arjendu K. Pattanayak. Lyapunov exponents, entropy production, and decoherence. *Phys. Rev. Lett.*, 83:4526–4529, Nov 1999.

- [103] Diana Monteoliva and Juan Pablo Paz. Decoherence and the rate of entropy production in chaotic quantum systems. *Phys. Rev. Lett.*, 85:3373–3376, Oct 2000.
- [104] Diana Monteoliva and Juan Pablo Paz. Decoherence in a classically chaotic quantum system: Entropy production and quantum-classical correspondence. *Phys. Rev. E*, 64:056238, Oct 2001.
- [105] Pablo Bianucci, Juan Pablo Paz, and Marcos Saraceno. Decoherence for classically chaotic quantum maps. *Phys. Rev. E*, 65:046226, Apr 2002.
- [106] Xi-Wen Hou and Bambi Hu. Decoherence, entanglement, and chaos in the dicke model. *Phys. Rev. A*, 69:042110, Apr 2004.
- [107] Wojciech Hubert Zurek. *Decoherence and the Transition from Quantum to Classical — Revisited*, pages 1–31. Birkhäuser Basel, Basel, 2007.
- [108] Shohini Ghose, Rene Stock, Poul Jessen, Roshan Lal, and Andrew Silberfarb. Chaos, entanglement, and decoherence in the quantum kicked top. *Phys. Rev. A*, 78:042318, Oct 2008.
- [109] Jayendra N. Bandyopadhyay. Quantum chaotic system as a model of decohering environment. *EPL (Europhysics Letters)*, 85(5):50006, mar 2009.
- [110] Mihai Horoi, Vladimir Zelevinsky, and B. Alex Brown. Chaos vs thermalization in the nuclear shell model. *Phys. Rev. Lett.*, 74:5194–5197, Jun 1995.
- [111] Marcos Rigol and Lea F. Santos. Quantum chaos and thermalization in gapped systems. *Phys. Rev. A*, 82:011604, Jul 2010.
- [112] Alexander Altland and Fritz Haake. Quantum chaos and effective thermalization. *Phys. Rev. Lett.*, 108:073601, Feb 2012.
- [113] F. Borgonovi, F.M. Izrailev, L.F. Santos, and V.G. Zelevinsky. Quantum chaos and thermalization in isolated systems of interacting particles. *Physics Reports*, 626:1–58, 2016. Quantum chaos and thermalization in isolated systems of interacting particles.

- [114] Luca D’Alessio, Yariv Kafri, Anatoli Polkovnikov, and Marcos Rigol. From quantum chaos and eigenstate thermalization to statistical mechanics and thermodynamics. *Advances in Physics*, 65(3):239–362, 2016.
- [115] Joshua M Deutsch. Eigenstate thermalization hypothesis. *Reports on Progress in Physics*, 81(8):082001, jul 2018.
- [116] Anatoly Dymarsky, Nima Lashkari, and Hong Liu. Subsystem eigenstate thermalization hypothesis. *Phys. Rev. E*, 97:012140, Jan 2018.
- [117] David Jansen, Jan Stolpp, Lev Vidmar, and Fabian Heidrich-Meisner. Eigenstate thermalization and quantum chaos in the holstein polaron model. *Phys. Rev. B*, 99:155130, Apr 2019.
- [118] Lata Kh Joshi, Andreas Elben, Amit Vikram, Benoît Vermersch, Victor Galitski, and Peter Zoller. Probing many-body quantum chaos with quantum simulators. *Phys. Rev. X*, 12:011018, Jan 2022.
- [119] Stephen H Shenker and Douglas Stanford. Black holes and the butterfly effect. *Journal of High Energy Physics*, 2014(3):1–25, 2014.
- [120] Daniel A. Roberts and Douglas Stanford. Diagnosing chaos using four-point functions in two-dimensional conformal field theory. *Phys. Rev. Lett.*, 115:131603, Sep 2015.
- [121] Juan Maldacena, Stephen H Shenker, and Douglas Stanford. A bound on chaos. *Journal of High Energy Physics*, 2016(8):1–17, 2016.
- [122] Pavan Hosur, Xiao-Liang Qi, Daniel A Roberts, and Beni Yoshida. Chaos in quantum channels. *Journal of High Energy Physics*, 2016(2):1–49, 2016.
- [123] Brian Swingle, Gregory Bentsen, Monika Schleier-Smith, and Patrick Hayden. Measuring the scrambling of quantum information. *Phys. Rev. A*, 94:040302, Oct 2016.
- [124] Efim B. Rozenbaum, Sriram Ganeshan, and Victor Galitski. Lyapunov exponent and out-of-time-ordered correlator’s growth rate in a chaotic system. *Phys. Rev. Lett.*, 118:086801, Feb 2017.

- [125] Ignacio García-Mata, Marcos Saraceno, Rodolfo A. Jalabert, Augusto J. Roncaglia, and Diego A. Wisniacki. Chaos signatures in the short and long time behavior of the out-of-time ordered correlator. *Phys. Rev. Lett.*, 121:210601, Nov 2018.
- [126] Jorge Chávez-Carlos, B. López-del Carpio, Miguel A. Bastarrachea-Magnani, Pavel Stránský, Sergio Lerma-Hernández, Lea F. Santos, and Jorge G. Hirsch. Quantum and classical lyapunov exponents in atom-field interaction systems. *Phys. Rev. Lett.*, 122:024101, Jan 2019.
- [127] Hua Yan, Jiao-Zi Wang, and Wen-Ge Wang. Similar early growth of out-of-time-ordered correlators in quantum chaotic and integrable ising chains. *Communications in Theoretical Physics*, 71(11):1359, nov 2019.
- [128] Efim B. Rozenbaum, Sriram Ganeshan, and Victor Galitski. Universal level statistics of the out-of-time-ordered operator. *Phys. Rev. B*, 100:035112, Jul 2019.
- [129] Jorge Chávez-Carlos, B. López-del Carpio, Miguel A. Bastarrachea-Magnani, Pavel Stránský, Sergio Lerma-Hernández, Lea F. Santos, and Jorge G. Hirsch. Quantum and classical lyapunov exponents in atom-field interaction systems. *Phys. Rev. Lett.*, 122:024101, Jan 2019.
- [130] Emiliano M. Fortes, Ignacio García-Mata, Rodolfo A. Jalabert, and Diego A. Wisniacki. Gauging classical and quantum integrability through out-of-time-ordered correlators. *Phys. Rev. E*, 100:042201, Oct 2019.
- [131] Arul Lakshminarayan. Out-of-time-ordered correlator in the quantum baker's map and truncated unitary matrices. *Phys. Rev. E*, 99:012201, Jan 2019.
- [132] Jiaozi Wang, Giuliano Benenti, Giulio Casati, and Wen-ge Wang. Quantum chaos and the correspondence principle. *Phys. Rev. E*, 103:L030201, Mar 2021.
- [133] H.-J. Stöckmann and J. Stein. “quantum” chaos in billiards studied by microwave absorption. *Phys. Rev. Lett.*, 64:2215–2218, May 1990.
- [134] M. Sieber and F. Steiner. Quantum chaos in the hyperbola billiard. *Physics Letters A*, 148(8):415–420, 1990.

- [135] E. Cuevas, E. Louis, and J. A. Vergés. Model of quantum chaotic billiards: Spectral statistics and wave functions in two dimensions. *Phys. Rev. Lett.*, 77:1970–1973, Sep 1996.
- [136] Suhan Ree and L. E. Reichl. Classical and quantum chaos in a circular billiard with a straight cut. *Phys. Rev. E*, 60:1607–1615, Aug 1999.
- [137] Wenjun Li, L. E. Reichl, and Biao Wu. Quantum chaos in a ripple billiard. *Phys. Rev. E*, 65:056220, May 2002.
- [138] Ārt Lozej, Giulio Casati, and Toma Ź Prosen. Quantum chaos in triangular billiards. *Phys. Rev. Research*, 4:013138, Feb 2022.
- [139] M.S. Santhanam, Sanku Paul, and J. Bharathi Kannan. Quantum kicked rotor and its variants: Chaos, localization and beyond. *Physics Reports*, 956:1–87, 2022. Quantum kicked rotor and its variants: Chaos, localization and beyond.
- [140] Roberto Artuso, Giulio Casati, and Dima Shepelyansky. Fractal spectrum and anomalous diffusion in the kicked harper model. *Phys. Rev. Lett.*, 68:3826–3829, Jun 1992.
- [141] R. Artuso, F. Borgonovi, I. Guarneri, L. Rebuzzini, and G. Casati. Phase diagram in the kicked harper model. *Phys. Rev. Lett.*, 69:3302–3305, Dec 1992.
- [142] R. Artuso, G. Casati, F. Borgonovi, L. Rebuzzini, and I. Guarneri. Fractal and dynamical properties of the kicked harper model. *International Journal of Modern Physics B*, 08(03):207–235, 1994.
- [143] Paul A. Miller and Sarben Sarkar. Signatures of chaos in the entanglement of two coupled quantum kicked tops. *Phys. Rev. E*, 60:1542–1550, Aug 1999.
- [144] Hiroshi Fujisaki, Takayuki Miyadera, and Atushi Tanaka. Dynamical aspects of quantum entanglement for weakly coupled kicked tops. *Phys. Rev. E*, 67:066201, Jun 2003.
- [145] Rafał Demkowicz-Dobrzański and Marek Kuś. Global entangling properties of the coupled kicked tops. *Phys. Rev. E*, 70:066216, Dec 2004.

- [146] Udaysinh T. Bhosale and M. S. Santhanam. Signatures of bifurcation on quantum correlations: Case of the quantum kicked top. *Phys. Rev. E*, 95:012216, Jan 2017.
- [147] Meenu Kumari and Shohini Ghose. Quantum-classical correspondence in the vicinity of periodic orbits. *Phys. Rev. E*, 97:052209, May 2018.
- [148] Shruti Dogra, Vaibhav Madhok, and Arul Lakshminarayan. Quantum signatures of chaos, thermalization, and tunneling in the exactly solvable few-body kicked top. *Phys. Rev. E*, 99:062217, Jun 2019.
- [149] Meenu Kumari and Shohini Ghose. Untangling entanglement and chaos. *Phys. Rev. A*, 99:042311, Apr 2019.
- [150] Udaysinh T. Bhosale and M. S. Santhanam. Periodicity of quantum correlations in the quantum kicked top. *Phys. Rev. E*, 98:052228, Nov 2018.
- [151] Fritz Haake, M Kuś, and Rainer Scharf. Classical and quantum chaos for a kicked top. *Zeitschrift für Physik B Condensed Matter*, 65(3):381–395, 1987.
- [152] J M Radcliffe. Some properties of coherent spin states. *Journal of Physics A: General Physics*, 4(3):313–323, may 1971.
- [153] J. R. Klauder and B. Skagerstam. *Coherent States: Applications in Physics and Mathematical Physics*. World Scientific, 1985.
- [154] Navin Khaneja, Timo Reiss, Cindie Kehlet, Thomas Schulte-Herbrüggen, and Steffen J. Glaser. Optimal control of coupled spin dynamics: design of nmr pulse sequences by gradient ascent algorithms. *Journal of Magnetic Resonance*, 172(2):296–305, 2005.
- [155] V. S. Anjusha and T. S. Mahesh. Optimized dynamical protection of nonclassical correlation in a quantum algorithm, 2018.
- [156] Evan M. Fortunato, Marco A. Pravia, Nicolas Boulant, Grum Teklemariam, Timothy F. Havel, and David G. Cory. Design of strongly modulating pulses to implement precise effective hamiltonians for quantum information processing. *The Journal of Chemical Physics*, 116(17):7599–7606, 2002.

- [157] Kôdi Husimi. Some formal properties of the density matrix. *Proceedings of the Physico-Mathematical Society of Japan. 3rd Series*, 22(4):264–314, 1940.
- [158] Yutaka Kano. A new phase-space distribution function in the statistical theory of the electromagnetic field. *Journal of Mathematical Physics*, 6(12):1913–1915, 1965.
- [159] Jonathan A. Jones, Steven D. Karlen, Joseph Fitzsimons, Arzhang Ardavan, Simon C. Benjamin, G. Andrew D. Briggs, and John J. L. Morton. Magnetic field sensing beyond the standard quantum limit using 10-spin noon states. *Science*, 324(5931):1166–1168, 2009.
- [160] Vittorio Giovannetti, Seth Lloyd, and Lorenzo Maccone. Advances in quantum metrology. *Nature photonics*, 5(4):222–229, 2011.
- [161] Itai Afek, Oron Ambar, and Yaron Silberberg. High-noon states by mixing quantum and classical light. *Science*, 328(5980):879–881, 2010.
- [162] Takafumi Ono, Ryo Okamoto, and Shigeki Takeuchi. An entanglement-enhanced microscope. *Nature communications*, 4(1):1–7, 2013.
- [163] Varad R. Pande, Gaurav Bhole, Deepak Khurana, and T. S. Mahesh. Strong algorithmic cooling in large star-topology quantum registers. *Phys. Rev. A*, 96:012330, Jul 2017.
- [164] CS Sudheer Kumar and TS Mahesh. Ancilla-induced amplification of quantum fisher information. *The European Physical Journal Plus*, 133(11):460, 2018.
- [165] Soham Pal, Naveen Nishad, T. S. Mahesh, and G. J. Sreejith. Temporal order in periodically driven spins in star-shaped clusters. *Phys. Rev. Lett.*, 120:180602, May 2018.
- [166] Jitendra Joshi and T. S. Mahesh. Experimental investigation of a quantum battery using star-topology nmr spin systems. *Phys. Rev. A*, 106:042601, Oct 2022.
- [167] Ran Liu, Yanjun Hou, Ze Wu, Hui Zhou, Jiahui Chen, Xi Chen, Zhaokai Li, and Xinhua Peng. Optimal and robust experiment design for quantum state tomography of star-topology register, 2022.

- [168] Mohamad Niknam, Lea F. Santos, and David G. Cory. Experimental detection of the correlation rényi entropy in the central spin model. *Phys. Rev. Lett.*, 127:080401, Aug 2021.
- [169] David J Griffiths and Darrell F Schroeter. *Introduction to quantum mechanics*. Cambridge university press, 2018.
- [170] B.D. Josephson. Possible new effects in superconductive tunnelling. *Physics Letters*, 1(7):251–253, 1962.
- [171] Sidney Shapiro. Josephson currents in superconducting tunneling: The effect of microwaves and other observations. *Phys. Rev. Lett.*, 11:80–82, Jul 1963.
- [172] Michael Tinkham. *Introduction to superconductivity*. Courier Corporation, 2004.
- [173] P Bedrossian, DM Chen, K Mortensen, and JA Golovchenko. Demonstration of the tunnel-diode effect on an atomic scale. *Nature*, 342(6247):258–260, 1989.
- [174] Eric Mevel, Pierre Breger, Rusty Trainham, Guillaume Petite, Pierre Agostini, Arnold Migus, Jean-Paul Chambaret, and Andre Antonetti. Atoms in strong optical fields: Evolution from multiphoton to tunnel ionization. *Phys. Rev. Lett.*, 70:406–409, Jan 1993.
- [175] Joachim Ankerhold. *Quantum tunneling in complex systems: the semiclassical approach*, volume 224. Springer Berlin, Heidelberg, 2007.
- [176] Julian Chen. *Introduction to Scanning Tunneling Microscopy Third Edition*, volume 69. Oxford University Press, USA, 2021.
- [177] Srihari Keshavamurthy and Peter Schlagheck. *Dynamical tunneling: theory and experiment*. CRC Press, 2011.
- [178] Michael J Davis and Eric J Heller. Quantum dynamical tunneling in bound states. *The Journal of Chemical Physics*, 75(1):246–254, 1981.
- [179] Eric J Heller and Michael J Davis. Quantum dynamical tunneling in large molecules. a plausible conjecture. *The Journal of Physical Chemistry*, 85(4):307–309, 1981.

- [180] Asher Peres. Dynamical quasidegeneracies and quantum tunneling. *Phys. Rev. Lett.*, 67:158–158, Jul 1991.
- [181] Steven Tomsovic. Tunneling and chaos. *Physica Scripta*, 2001(T90):162, 2001.
- [182] Olivier Brodier, Peter Schlagheck, and Denis Ullmo. Resonance-assisted tunneling in near-integrable systems. *Phys. Rev. Lett.*, 87:064101, Jul 2001.
- [183] A. Bäcker, R. Ketzmerick, S. Löck, M. Robnik, G. Vidmar, R. Höhmann, U. Kuhl, and H.-J. Stöckmann. Dynamical tunneling in mushroom billiards. *Phys. Rev. Lett.*, 100:174103, May 2008.
- [184] Olivier Brodier, Peter Schlagheck, and Denis Ullmo. Resonance-assisted tunneling. *Annals of Physics*, 300(1):88–136, 2002.
- [185] Steffen Löck, Arnd Bäcker, Roland Ketzmerick, and Peter Schlagheck. Regular-to-chaotic tunneling rates: From the quantum to the semiclassical regime. *Phys. Rev. Lett.*, 104:114101, Mar 2010.
- [186] Christopher Eltschka and Peter Schlagheck. Resonance- and chaos-assisted tunneling in mixed regular-chaotic systems. *Phys. Rev. Lett.*, 94:014101, Jan 2005.
- [187] Stefan Gehler, Steffen Löck, Susumu Shinohara, Arnd Bäcker, Roland Ketzmerick, Ulrich Kuhl, and Hans-Jürgen Stöckmann. Experimental observation of resonance-assisted tunneling. *Phys. Rev. Lett.*, 115:104101, Sep 2015.
- [188] Felix Fritsch, Roland Ketzmerick, and Arnd Bäcker. Resonance-assisted tunneling in deformed optical microdisks with a mixed phase space. *Phys. Rev. E*, 100:042219, Oct 2019.
- [189] C. Dembowski, H.-D. Gräf, A. Heine, R. Hofferbert, H. Rehfeld, and A. Richter. First experimental evidence for chaos-assisted tunneling in a microwave annular billiard. *Phys. Rev. Lett.*, 84:867–870, Jan 2000.
- [190] Daniel A. Steck, Windell H. Oskay, and Mark G. Raizen. Fluctuations and decoherence in chaos-assisted tunneling. *Phys. Rev. Lett.*, 88:120406, Mar 2002.

- [191] A. Mouchet, C. Miniatura, R. Kaiser, B. Grémaud, and D. Delande. Chaos-assisted tunneling with cold atoms. *Phys. Rev. E*, 64:016221, Jun 2001.
- [192] R. Hofferbert, H. Alt, C. Dembowski, H.-D. Gräf, H. L. Harney, A. Heine, H. Rehfeld, and A. Richter. Experimental investigations of chaos-assisted tunneling in a microwave annular billiard. *Phys. Rev. E*, 71:046201, Apr 2005.
- [193] G. Vanhaele and P. Schlagheck. Noon states with ultracold bosonic atoms via resonance- and chaos-assisted tunneling. *Phys. Rev. A*, 103:013315, Jan 2021.
- [194] G. Vanhaele, A. Bäcker, R. Ketzmerick, and P. Schlagheck. Creating triple-noon states with ultracold atoms via chaos-assisted tunneling. *Phys. Rev. A*, 106:L011301, Jul 2022.
- [195] Urbashi Satpathi, Sayak Ray, and Amichay Vardi. Chaos-assisted many-body tunnelling. *Phys. Rev. E*, 106:L042204, Oct 2022.
- [196] BC Sanders and GJ Milburn. The effect of measurement on the quantum features of a chaotic system. *Zeitschrift für Physik B Condensed Matter*, 77(3):497–510, 1989.
- [197] V. R. Krithika, V. S. Anjusha, Udaysinh T Bhosale, and T. S. Mahesh. Nmr studies of quantum chaos in a two-qubit kicked top. *Physical Review E*, 99(3):032219, 2019.
- [198] Chong Chen, Jun-Hong An, Hong-Gang Luo, C. P. Sun, and C. H. Oh. Floquet control of quantum dissipation in spin chains. *Phys. Rev. A*, 91:052122, May 2015.
- [199] Pieter W. Claeys, Mohit Pandey, Dries Sels, and Anatoli Polkovnikov. Floquet-engineering counterdiabatic protocols in quantum many-body systems. *Phys. Rev. Lett.*, 123:090602, Aug 2019.
- [200] Bin Yan, Lukasz Cincio, and Wojciech H Zurek. Information scrambling and loschmidt echo. *Physical review letters*, 124(16):160603, 2020.
- [201] Jun Li, Ruihua Fan, Hengyan Wang, Bingtian Ye, Bei Zeng, Hui Zhai, Xinhua Peng, and Jiangfeng Du. Measuring out-of-time-order correlators on a nuclear magnetic resonance quantum simulator. *Phys. Rev. X*, 7:031011, Jul 2017.

- [202] Christopher J Turner, Alexios A Michailidis, Dmitry A Abanin, Maksym Serbyn, and Zlatko Papić. Weak ergodicity breaking from quantum many-body scars. *Nature Physics*, 14(7):745–749, 2018.
- [203] Maksym Serbyn, Dmitry A Abanin, and Zlatko Papić. Quantum many-body scars and weak breaking of ergodicity. *Nature Physics*, 17(6):675–685, 2021.
- [204] Arkady Pikovsky, Jurgen Kurths, Michael Rosenblum, and Jürgen Kurths. *Synchronization: a universal concept in nonlinear sciences*. Number 12. Cambridge university press, 2003.
- [205] Tony E Lee and H. R. Sadeghpour. Quantum synchronization of quantum van der pol oscillators with trapped ions. *Physical review letters*, 111(23):234101, 2013.
- [206] Michael R Hush, Weibin Li, Sam Genway, Igor Lesanovsky, and Andrew D Armour. Spin correlations as a probe of quantum synchronization in trapped-ion phonon lasers. *Physical Review A*, 91:061401, 2015.
- [207] Simon E Nigg. Observing quantum synchronization blockade in circuit quantum electrodynamics. *Physical Review A*, 97(1):013811, 2018.
- [208] Minghui Xu, David A Tieri, E. C. Fine, James K Thompson, and Murray J Holland. Synchronization of two ensembles of atoms. *Physical review letters*, 113(15):154101, 2014.
- [209] Max Ludwig and Florian Marquardt. Quantum many-body dynamics in optomechanical arrays. *Phys. Rev. Lett.*, 111:073603, Aug 2013.
- [210] Stefan Walter, Andreas Nunnenkamp, and Christoph Bruder. Quantum synchronization of a driven self-sustained oscillator. *Physical review letters*, 112(9):094102, 2014.
- [211] Stefan Walter, Andreas Nunnenkamp, and Christoph Bruder. Quantum synchronization of two van der pol oscillators. *Annalen der Physik*, 527(1-2):131–138, 2015.
- [212] Wenlin Li, Chong Li, and Heshan Song. Quantum synchronization in an optomechanical system based on lyapunov control. *Physical Review E*, 93(6):062221, 2016.

- [213] Mian Zhang, Gustavo S Wiederhecker, Sasikanth Manipatruni, Arthur Barnard, Paul McEuen, and Michal Lipson. Synchronization of micromechanical oscillators using light. *Physical review letters*, 109(23):233906, 2012.
- [214] Catherine A Holmes, Charles P Meaney, and Gerard J Milburn. Synchronization of many nanomechanical resonators coupled via a common cavity field. *Physical Review E*, 85(6):066203, 2012.
- [215] Dirk Witthaut, Sandro Wimberger, Raffaella Burioni, and Marc Timme. Classical synchronization indicates persistent entanglement in isolated quantum systems. *Nature communications*, 8(1):1–7, 2017.
- [216] Alexandre Roulet and Christoph Bruder. Quantum synchronization and entanglement generation. *Physical review letters*, 121(6):063601, 2018.
- [217] Noufal Jaseem, Michal Hajdušek, Vlatko Vedral, Rosario Fazio, Leong-Chuan Kwek, and Sai Vinjanampathy. Quantum synchronization in nanoscale heat engines. *Physical Review E*, 101(2):020201, 2020.
- [218] Parvinder Solanki, Noufal Jaseem, Michal Hajdušek, and Sai Vinjanampathy. Role of coherence and degeneracies in quantum synchronization. *Phys. Rev. A*, 105:L020401, Feb 2022.
- [219] Wenlin Li, Chong Li, and Heshan Song. Quantum synchronization and quantum state sharing in an irregular complex network. *Physical Review E*, 95(2):022204, 2017.
- [220] Michal Hajdušek, Parvinder Solanki, Rosario Fazio, and Sai Vinjanampathy. Seeding crystallization in time. *Phys. Rev. Lett.*, 128:080603, Feb 2022.
- [221] Alexandre Roulet and Christoph Bruder. Synchronizing the smallest possible system. *Phys. Rev. Lett.*, 121:053601, Jul 2018.
- [222] Noufal Jaseem, Michal Hajdušek, Parvinder Solanki, Leong-Chuan Kwek, Rosario Fazio, and Sai Vinjanampathy. Generalized measure of quantum synchronization. *Physical Review Research*, 2(4):043287, 2020.

- [223] Wolfgang P Schleich. *Quantum optics in phase space*. John Wiley & Sons, 2011.
- [224] Fernando Galve, Gian Luca Giorgi, and Roberta Zambrini. *Quantum Correlations and Synchronization Measures*, pages 393–420. Springer International Publishing, Cham, 2017.
- [225] Wenlin Li, Wenzhao Zhang, Chong Li, and Heshan Song. Properties and relative measure for quantifying quantum synchronization. *Physical Review E*, 96(1):012211, 2017.
- [226] Martin Koppenhöfer and Alexandre Roulet. Optimal synchronization deep in the quantum regime: Resource and fundamental limit. *Physical Review A*, 99(4):043804, 2019.
- [227] A. Mari, A. Farace, N. Didier, V. Giovannetti, and R. Fazio. Measures of quantum synchronization in continuous variable systems. *Phys. Rev. Lett.*, 111:103605, Sep 2013.
- [228] Gonzalo Manzano, Fernando Galve, Gian Luca Giorgi, Emilio Hernández-García, and Roberta Zambrini. Synchronization, quantum correlations and entanglement in oscillator networks. *Scientific Reports*, 3(1):1–6, 2013.
- [229] V Ameri, M Eghbali-Arani, A Mari, A Farace, F Kheirandish, V Giovannetti, and R Fazio. Mutual information as an order parameter for quantum synchronization. *Physical Review A*, 91(1):012301, 2015.
- [230] Sameer Sonar, Michal Hajdušek, Manas Mukherjee, Rosario Fazio, Vlatko Vedral, Sai Vinjanampathy, and Leong-Chuan Kwek. Squeezing enhances quantum synchronization. *Phys. Rev. Lett.*, 120:163601, Apr 2018.
- [231] Berislav Buca, Cameron Booker, and Dieter Jaksch. Algebraic Theory of Quantum Synchronization and Limit Cycles under Dissipation. *SciPost Phys.*, 12:97, 2022.
- [232] Göktuğ Karpat, İskender Yalçınkaya, Barış Çakmak, Gian Luca Giorgi, and Roberta Zambrini. Synchronization and non-markovianity in open quantum systems. *Phys. Rev. A*, 103:062217, Jun 2021.
- [233] G. Karpat, İ. Yalçınkaya, and B. Çakmak. Quantum synchronization of few-body systems under collective dissipation. *Phys. Rev. A*, 101:042121, Apr 2020.

- [234] G. Karpat, İ. Yalçınkaya, and B. Çakmak. Quantum synchronization in a collision model. *Phys. Rev. A*, 100:012133, Jul 2019.
- [235] Gian Luca Giorgi, Fernando Galve, and Roberta Zambrini. Probing the spectral density of a dissipative qubit via quantum synchronization. *Phys. Rev. A*, 94:052121, Nov 2016.
- [236] G. L. Giorgi, F. Plastina, G. Francica, and R. Zambrini. Spontaneous synchronization and quantum correlation dynamics of open spin systems. *Phys. Rev. A*, 88:042115, Oct 2013.
- [237] Martin Koppenhöfer, Christoph Bruder, and Alexandre Roulet. Quantum synchronization on the ibm q system. *Physical Review Research*, 2(2):023026, 2020.
- [238] Arif Warsi Laskar, Pratik Adhikary, Suprodip Mondal, Parag Katiyar, Sai Vinjanampathy, and Saikat Ghosh. Observation of quantum phase synchronization in spin-1 atoms. *Physical Review Letters*, 125(1):013601, 2020.
- [239] Ingemar Bengtsson and Karol Zyczkowski. *Geometry of Quantum States: An Introduction to Quantum Entanglement*. Cambridge University Press, 2006.
- [240] Yen Lee Loh and Monica Kim. Visualizing spin states using the spin coherent state representation. *American Journal of Physics*, 83(1):30–35, 2015.
- [241] Kae Nemoto. Generalized coherent states for  $su(n)$  systems. *Journal of Physics A: Mathematical and General*, 33(17):3493, 2000.
- [242] Askold Perelomov. *Generalized Coherent States and Their Applications*. Springer, Berlin, Heidelberg, 1986.
- [243] Manu Mathur and HS Mani.  $Su(n)$  coherent states. *Journal of Mathematical Physics*, 43(11):5351–5364, 2002.
- [244] Heinz-Peter Breuer, Francesco Petruccione, et al. *The theory of open quantum systems*. Oxford University Press on Demand, 2002.
- [245] Arnab Ghosh, Sudarson Sekhar Sinha, and Deb Shankar Ray. Fermionic oscillator in a fermionic bath. *Physical Review E*, 86(1):011138, 2012.

- [246] Nishchay Suri, Felix C Binder, Bhaskaran Muralidharan, and Sai Vinjanampathy. Speeding up thermalisation via open quantum system variational optimisation. *The European Physical Journal Special Topics*, 227(3):203–216, 2018.
- [247] Daniel Manzano. A short introduction to the lindblad master equation. *AIP Advances*, 10(2):025106, 2020.
- [248] Jerryman A Gyamfi. Fundamentals of quantum mechanics in liouville space. *European Journal of Physics*, 41(6):063002, 2020.
- [249] Carlos Navarrete-Benlloch. Open systems dynamics: Simulating master equations in the computer. *arXiv preprint arXiv:1504.05266*, 2015.
- [250] N Boulant, T. F. Havel, M. A Pravia, and D. G Cory. Robust method for estimating the lindblad operators of a dissipative quantum process from measurements of the density operator at multiple time points. *Physical Review A*, 67(4):042322, 2003.
- [251] Isaac L Chuang, Neil Gershenfeld, Mark G Kubinec, and Debbie W Leung. Bulk quantum computation with nuclear magnetic resonance: theory and experiment. *Proceedings of the Royal Society of London. Series A: Mathematical, Physical and Engineering Sciences*, 454(1969):447–467, 1998.
- [252] Abhishek Shukla, K Rama Koteswara Rao, and T. S Mahesh. Ancilla-assisted quantum state tomography in multiqubit registers. *Physical Review A*, 87(6):062317, 2013.
- [253] Varad R. Pande, Gaurav Bhole, Deepak Khurana, and T. S. Mahesh. Strong algorithmic cooling in large star-topology quantum registers. *Phys. Rev. A*, 96:012330, Jul 2017.
- [254] DV Averin and KK Likharev. Coulomb blockade of single-electron tunneling, and coherent oscillations in small tunnel junctions. *Journal of low temperature physics*, 62(3):345–373, 1986.
- [255] T. A. Fulton and G. J. Dolan. Observation of single-electron charging effects in small tunnel junctions. *Phys. Rev. Lett.*, 59:109–112, Jul 1987.

- [256] K. Ono, D. G. Austing, Y. Tokura, and S. Tarucha. Current rectification by pauli exclusion in a weakly coupled double quantum dot system. *Science*, 297(5585):1313–1317, 2002.
- [257] Kevin M Birnbaum, Andreea Boca, Russell Miller, Allen D Boozer, Tracy E Northup, and H Jeff Kimble. Photon blockade in an optical cavity with one trapped atom. *Nature*, 436(7047):87–90, 2005.
- [258] C. Lang, D. Bozyigit, C. Eichler, L. Steffen, J. M. Fink, A. A. Abdumalikov, M. Baur, S. Filipp, M. P. da Silva, A. Blais, and A. Wallraff. Observation of resonant photon blockade at microwave frequencies using correlation function measurements. *Phys. Rev. Lett.*, 106:243601, Jun 2011.
- [259] A. J. Hoffman, S. J. Srinivasan, S. Schmidt, L. Spietz, J. Aumentado, H. E. Türeci, and A. A. Houck. Dispersive photon blockade in a superconducting circuit. *Phys. Rev. Lett.*, 107:053602, Jul 2011.
- [260] Cyril Vaneph, Alexis Morvan, Gianluca Aiello, Mathieu Féchant, Marco Aprili, Julien Gabelli, and Jérôme Estève. Observation of the unconventional photon blockade in the microwave domain. *Phys. Rev. Lett.*, 121:043602, Jul 2018.
- [261] H. J. Snijders, J. A. Frey, J. Norman, H. Flayac, V. Savona, A. C. Gossard, J. E. Bowers, M. P. van Exter, D. Bouwmeester, and W. Löffler. Observation of the unconventional photon blockade. *Phys. Rev. Lett.*, 121:043601, Jul 2018.
- [262] Jiandong Feng, Ke Liu, Michael Graf, Dumitru Dumcenco, Andras Kis, Massimiliano Di Ventra, and Aleksandra Radenovic. Observation of ionic coulomb blockade in nanopores. *Nature materials*, 15(8):850–855, 2016.
- [263] Alpha Gaëtan, Yevhen Miroshnychenko, Tatjana Wilk, Amodsen Chotia, Matthieu Viteau, Daniel Comparat, Pierre Pillet, Antoine Browaeys, and Philippe Grangier. Observation of collective excitation of two individual atoms in the rydberg blockade regime. *Nature Physics*, 5(2):115–118, 2009.
- [264] E. Urban, T. A. Johnson, T. Henage, L. Isenhower, D. D. Yavuz, T. G. Walker, and

- M. Saffman. Observation of rydberg blockade between two atoms. *Nature Physics*, 5(2):110–114, 2009.
- [265] D. Barredo, S. Ravets, H. Labuhn, L. Béguin, A. Vernier, F. Nogrette, T. Lahaye, and A. Browaeys. Demonstration of a strong rydberg blockade in three-atom systems with anisotropic interactions. *Phys. Rev. Lett.*, 112:183002, May 2014.
- [266] J. R. Petta, A. C. Johnson, J. M. Taylor, E. A. Laird, A. Yacoby, M. D. Lukin, C. M. Marcus, M. P. Hanson, and A. C. Gossard. Coherent manipulation of coupled electron spins in semiconductor quantum dots. *Science*, 309(5744):2180–2184, 2005.
- [267] K. C. Nowack, F. H. L. Koppens, Yu. V. Nazarov, and L. M. K. Vandersypen. Coherent control of a single electron spin with electric fields. *Science*, 318(5855):1430–1433, 2007.
- [268] Andrei Faraon, Ilya Fushman, Dirk Englund, Nick Stoltz, Pierre Petroff, and Jelena Vučković. Coherent generation of non-classical light on a chip via photon-induced tunnelling and blockade. *Nat. Phys.*, 4(11):859–863, 2008.
- [269] Thibault Peyronel, Ofer Firstenberg, Qi-Yu Liang, Sebastian Hofferberth, Alexey V. Gorshkov, Thomas Pohl, Mikhail D. Lukin, and Vladan Vuletić. Quantum nonlinear optics with single photons enabled by strongly interacting atoms. *Nature*, 488(7409):57–60, 2012.
- [270] Kai Müller, Armand Rundquist, Kevin A. Fischer, Tomas Sarmiento, Konstantinos G. Lagoudakis, Yousif A. Kelaita, Carlos Sánchez Muñoz, Elena del Valle, Fabrice P. Laussy, and Jelena Vučković. Coherent generation of nonclassical light on chip via detuned photon blockade. *Phys. Rev. Lett.*, 114:233601, Jun 2015.
- [271] M. D. Lukin, M. Fleischhauer, R. Cote, L. M. Duan, D. Jaksch, J. I. Cirac, and P. Zoller. Dipole blockade and quantum information processing in mesoscopic atomic ensembles. *Phys. Rev. Lett.*, 87:037901, Jun 2001.
- [272] M. Saffman, T. G. Walker, and K. Mølmer. Quantum information with rydberg atoms. *Rev. Mod. Phys.*, 82:2313–2363, Aug 2010.

- [273] Antoine Browaeys and Thierry Lahaye. Many-body physics with individually controlled rydberg atoms. *Nature Physics*, 16(2):132–142, 2020.
- [274] Vineesha Srivastava, Ankita Niranjana, and Rejish Nath. Dynamics and quantum correlations in two independently driven rydberg atoms with distinct laser fields. *Journal of Physics B: Atomic, Molecular and Optical Physics*, 52(18):184001, 2019.
- [275] Daniel Burgarth, Koji Maruyama, Michael Murphy, Simone Montangero, Tommaso Calarco, Franco Nori, and Martin B. Plenio. Scalable quantum computation via local control of only two qubits. *Phys. Rev. A*, 81:040303, Apr 2010.
- [276] Iulia Buluta and Franco Nori. Quantum simulators. *Science*, 326(5949):108–111, 2009.
- [277] J Ignacio Cirac and Peter Zoller. Goals and opportunities in quantum simulation. *Nature physics*, 8(4):264–266, 2012.
- [278] Jiangfeng Du, Nanyang Xu, Xinhua Peng, Pengfei Wang, Sanfeng Wu, and Dawei Lu. Nmr implementation of a molecular hydrogen quantum simulation with adiabatic state preparation. *Phys. Rev. Lett.*, 104:030502, Jan 2010.
- [279] Chenyong Ju, Chao Lei, Xiangkun Xu, Dimitrie Culcer, Zhenyu Zhang, and Jiangfeng Du. Nv-center-based digital quantum simulation of a quantum phase transition in topological insulators. *Phys. Rev. B*, 89:045432, Jan 2014.
- [280] Anjusha V.S., Swathi S. Hegde, and T.S. Mahesh. Nmr investigation of the quantum pi-geonhole effect. *Physics Letters A*, 380(4):577–580, 2016.
- [281] FangZhou Jin, HongWei Chen, Xing Rong, Hui Zhou, MingJun Shi, Qi Zhang, ChenYong Ju, YiFu Cai, ShunLong Luo, XinHua Peng, et al. Experimental simulation of the unruh effect on an nmr quantum simulator. *SCIENCE CHINA Physics, Mechanics & Astronomy*, 59(3):1–8, 2016.
- [282] Wentao Ji, Lin Zhang, Mengqi Wang, Long Zhang, Yuhang Guo, Zihua Chai, Xing Rong, Fazhan Shi, Xiong-Jun Liu, Ya Wang, and Jiangfeng Du. Quantum simulation for three-dimensional chiral topological insulator. *Phys. Rev. Lett.*, 125:020504, Jul 2020.

- [283] Rolf Heidemann, Ulrich Raitzsch, Vera Bendkowsky, Björn Butscher, Robert Löw, Luis Santos, and Tilman Pfau. Evidence for coherent collective rydberg excitation in the strong blockade regime. *Phys. Rev. Lett.*, 99:163601, Oct 2007.
- [284] Jingfu Zhang, Gui Lu Long, Wei Zhang, Zhiwei Deng, Wenzhang Liu, and Zhiheng Lu. Simulation of heisenberg  $xy$  interactions and realization of a perfect state transfer in spin chains using liquid nuclear magnetic resonance. *Phys. Rev. A*, 72:012331, Jul 2005.
- [285] Xinhua Peng, Jiangfeng Du, and Dieter Suter. Quantum phase transition of ground-state entanglement in a heisenberg spin chain simulated in an nmr quantum computer. *Phys. Rev. A*, 71:012307, Jan 2005.
- [286] Wenxian Zhang, Paola Cappellaro, Natania Antler, Brian Pepper, David G. Cory, Viatcheslav V. Dobrovitski, Chandrasekhar Ramanathan, and Lorenza Viola. Nmr multiple quantum coherences in quasi-one-dimensional spin systems: Comparison with ideal spin-chain dynamics. *Phys. Rev. A*, 80:052323, Nov 2009.
- [287] Ken Xuan Wei, Chandrasekhar Ramanathan, and Paola Cappellaro. Exploring localization in nuclear spin chains. *Physical review letters*, 120(7):070501, 2018.
- [288] Clément Hainaut, Adam Rançon, Jean-François Clément, Jean Claude Garreau, Pascal Szriftgiser, Radu Chicireanu, and Dominique Delande. Ratchet effect in the quantum kicked rotor and its destruction by dynamical localization. *Physical Review A*, 97(6):061601, 2018.
- [289] Hans Georg Krojanski and Dieter Suter. Scaling of decoherence in wide nmr quantum registers. *Phys. Rev. Lett.*, 93:090501, Aug 2004.
- [290] Xiao-Ming Lu, Jian Ma, Zhengjun Xi, and Xiaoguang Wang. Optimal measurements to access classical correlations of two-qubit states. *Physical Review A*, 83(1):012327, 2011.
- [291] P.V. Gagarinov. Spheretri. <https://github.com/pgagarinov/spheretri>, 2017.